Observation of Enhanced Raman Scattering as a Result of Coupling between Localized Plasmons and Surface Polariton Waves Associated with Metal-Semiconductor Nanocomposites

By

Natacha Souto Melgar

A dissertation submitted in partial fulfillment of the requirements for the degree of

DOCTOR OF PHILOSOPHY

In

CHEMICAL ENGINEERING

UNIVERSITY OF PUERTO RICO
MAYAGÜEZ CAMPUS

MAY 2011

Approved by:

_____	_____
Julio G. Briano, PhD *President, Graduate Committee*	Date
_____	_____
Carlos Rinaldi, PhD *Member, Graduate Committee*	Date
_____	_____
Arturo Hernández-Maldonado, PhD *Member, Graduate Committee*	Date
_____	_____
Nelson Cardona-Martínez, PhD *Member, Graduate Committee*	Date
_____	_____
Samuel Hernández-Rivera, PhD *Member, Graduate Committee*	Date
_____	_____
Alberto Santana-Vargas, PhD *Representative Graduate School*	Date
_____	_____
David Suleiman-Rosado, PhD *Chairperson of the Department*	Date

ABSTRACT

We report the observation of enhanced Raman scattering as a result of the coupling between the localized surface plasmon (LSP) of metal nanoparticles (NP) and the surface plasmon polariton (SPP) associated with a thin metal surface. In the present study, we apply AuNPs composites for the SERS detection of the trinitrotoluene (TNT) explosive, as well as to other related nitroaromatic derivatives. The analysis of TNT attracts current interest due to homeland security issues. We describe the successful detection of 4-NBT, 4-ABT, and TNT by an AuNPs – TiO_2 matrix associated with an Au coated p-Si/SiO_2 surface. The AuNPs matrix has been prepared by self-assembly of AuNPs – TiO_2 composites and characterized by AFM and Raman measurements. AuNPs were prepared by capping highly monodisperse colloidal n-TiO_2 particles with Au islands. Au capping was done by band-gap irradiation of colloidal TiO_2 and $HAuCl_4$ acid mixtures. The colloidal TiO_2 nanoparticles were prepared by controlled hydrolysis of titanium tetra-isopropoxide with aqueous $HClO_4$ solution (pH 1.5). The Au surfaces used in this research were microscopically smooth Au films deposited on semiconductor wafers cut from p-Si/SiO_2 single crystals. The Au films were prepared by physical vapor deposition using standard techniques. The final composite hybrid wafers were characterized for thickness and composition by standard SEM (thickness: p-Si, 222 μm; SiO_2, 171 μm; Au 8.4 μm). The smoothness of the Au surface was confirmed by optical microscopy (magnification 100 x), SEM, and AFM. Chemical etching of the smooth Au surface with full-strength *aqua regia* under well defined conditions also produced a matrix of AuNPs islands on the p-Si/SiO_2 wafers. The etched surface galleries allowed the observation of enhanced Raman scattering with TNT and the other nitroaromatic derivatives.

RESUMEN

Informamos la observación de dispersión realzada de Raman como resultado directo del acoplamiento entre el plasmón localizado (LSP) en nanopartículas (NP) metálicas y el polaritón o plasmón deslocalizado (SPP) asociado con una superficie metálica delgada. En este estudio aplicamos AuNPs compuestas de metal y semiconductor a la detección SERS del explosivo trinitrotolueno (TNT) así como a otros derivados nitroaromáticos. El análisis de TNT atrae interés actual debido a situaciones que afectan la seguridad nacional. Describimos la detección exitosa de 4-NBT, 4-ABT y TNT con una matriz de AuNPs – TiO_2 asociada a una superficie de p-Si/SiO_2 recubierta con una película de Au. La matriz de AuNPs se ha preparado por auto-ensamblaje de las AuNPs – TiO_2 y se ha caracterizado por medidas de AFM y dispersión Raman. Las AuNPs se prepararon cubriendo partículas de TiO_2 altamente mono dispersas con isletas de Au. El recubrimiento con Au se hizo mediante irradiación en el ancho de la banda de TiO_2 coloidal en presencia de ácido $HAuCl_4$. Las nanopartículas coloidales de TiO_2 se prepararon por hidrólisis controlada de tetraisopropóxido de titanio con una disolución de $HClO_4$ (pH 1.5). Las superficies de Au utilizadas eran películas de Au lisas a nivel microscópico depositadas sobre galletas semiconductoras cortadas de un solo cristal de p-Si/SiO_2. Las películas de Au se prepararon por deposición física mediante técnicas estándar. El espesor y la composición de las galletas así preparadas se caracterizaron mediante SEM estándar (espesor: p-Si, 222 μm; SiO_2, 171 μm; Au 8.4 μm). La rugosidad microscópica de la superficie de Au se confirmó por microscopía óptica (ampliación 100 x), SEM y AFM. Mediante la acción del *agua regia* sobre la superficie lisa de la película de Au bajo condiciones bien definidas se produjo también una matriz de isletas de AuNPs en las galletas de p-Si/SiO_2. Las galerías excavadas en la superficie permitieron la observación de dispersión Raman realzada con TNT y los otros derivados.

Dedication

To my parents Josefina and Fernando

ACKNOWLEDGEMENTS

I would like to show my gratitude to all those people that have contributed to the work described in this thesis. First of all I will like to thank my supervisor, Dr. Julio Briano, for his graduate course guidance, encouragement and financial support.

I wish to express a special thanks to Dr. Samuel Hernandez, for giving me the opportunity to do research in his laboratory facilities. It is an honor for me to be part of his research group. Thanks for the valuable suggestions and collaboration in the development of this research. There is no doubt that without him, this study would not have been completed.

I would like to extent my appreciation to all Dr. Samuel Hernandez group members especially Leonardo Pacheco and Oliva Primera. Thanks for their support, cooperation and insight in the project.

It is a pleasure to acknowledge the continuous support of Photochemistry Laboratory of the Natural Products Facility of the University of Puerto Rico in Mayagüez for ample access to their facilities, resources and materials. In particular I would like to express my gratitude to Prof. Lolita Rodríguez Rodríguez for letting me acces to her wet laboratory and small instrumentation laboratory. Her generous support with laboratory materials and SRQ stipends is also acknowledged.

I also acknowledge the exclusive support of Dr. Fernando A. Souto in helping me with set-up of the photochemistry experiments and the design of the colloidal TiO_2 hydrolysis experiments. I am also grateful for the suggestions to use the laminar flow hood facilities available at his laboratory to perform the self-assembly and evaporation experiments.

For additional financial support, I thank the Alfred P. Sloan Foundation's Graduate Scholarship Programs, the Department of Chemical Engineering and the Department of

Chemistry of the University of Puerto Rico at Mayaguez. I would also want to thank the Science on Wheels Educational Center (SONWEC) for giving me the opportunity to work with them. As a part of SONWEC I was able to stimulate the interest of teachers and K-12 students in science, and improve their education in chemistry, biology, physics and mathematics. I am also grateful for that.

I owe my deepest gratitude to Dr. Carlos Rinaldi. He has made available his support in a number of ways. This research would not have been possible without his financial assistance through all these years.

Thanks to Boris Rentería from the Materials Research Laboratory in the University of Puerto Rico, Mayaguez Campus for the AFM studies. Thanks for your patience and time. Also, thanks to Prof. Otaño from Physics Department of University of Puerto Rico in Cayey for obtaining the SEM images. TEM images were measured in the Department of Chemistry, Jackson State University by Dr. Oliva Primera, thanks for all your disposition and time.

Thanks to all the undergraduate students that help me through all these years: Gabriel Pérez, Rafael Soler and Wilfredo Cardona and Juan Lau.

It is difficult to overstate my appreciation to Dr. Fernando Souto. His deep insights, exceedingly enthusiasm and integral view on research have added tremendous value to the quality of the study. Not only a great mentor and father, he has also been a cornerstone in my professional development.

Lastly, and most importantly, I want to thank my mother, Josefina Melgar. She has always supported and encouraged me to do my best in all matters of life.

TABLE OF CONTENTS

LIST OF TABLES

LIST OF FIGURES

CHAPTER 1

1 INTRODUCTION

Over the last decades we have witnessed an overwhelming interest in nanotechnology. This is due to the scientific convergence of physics, chemistry, biology, materials science and engineering at the nanoscale level and the importance given to the control of matter of nanoscopic dimensions on almost all technologies.[1] Nanotechnology, a field of applied science and technology, is concerned with the development and utilization of structures and devices at the atomic, molecular and supramolecular levels, in the length scale of about 1 – 100 nm range. At the nanoscale, novel physical, chemical and biological properties occur as compared to individual atoms and molecules or bulk matter. For example, platinum, an inert material, becomes a catalyst; silicon, an insulator, becomes a conductor; and gold at room temperature becomes a liquid.[2] Also smaller particle size determines larger interfacial areas, an increased number of molecules on the particle interfaces, quantum electromagnetic interactions, increased surface tension, and size confinement effects.[1]

1.1 Nanoscale Research 1

A major issue in nanoscale research is how to convert the nanoscale material into a novel technological system. Nanoparticle fabrication may be classified into the following processes: (1) nanoparticle synthesis; (2) processing and conversion of nanoparticles into nanostructured materials, nanocomponents and nanodevices; (3) utilization of nanoparticles in order to produce or enhance a process or a phenomenon of mechanical, chemical, electrical, magnetic or biological nature. Nanoparticle synthesis methods include precipitation from solutions forming suspensions (colloids); gas condensation (aerosols); chemical, plasma and laser ablation; supercritical fluid expansion; polymerization; and mechanical attrition. Some nanoparticle

processing methods that have been employed consist of sintering, generation of nanostructures on surfaces, and molecular self assembly techniques. Nanostructure materials have been used in a broad class of applications such as agents of surface modification; filtration; bioseparation; pollution control in combustion; drug delivery and health diagnostics; catalysts and pigments in chemical plants; and sensors. Research challenges that have been major study objectives in the past few years include particle synthesis at high production rates, continuous particle synthesis, particle nucleation and growth mechanisms, and processing into functional nanostructures and devices.

1.2 Metal Nanoparticles (M-NPs)

Especially interesting nanoscale systems are metal nanoparticles (M-NPs) due to the simplicity in which they can be synthesized and modified chemically. Another advantage of metal nanoparticles over other systems is that their optical constants approximate those of the bulk metal even at these very small dimensions.[3] A unique property that M-NPs often show is a strong absorption band in the visible spectrum (plasmon) which is due to electron oscillations induced by incident light. Surface plasmons (SPs), plasmons confined to surfaces, interact strongly with light, resulting in a polariton (delocalized excitation). They occur at the interface between a material with a positive dielectric constant and another material with a negative dielectric constant, usually a metal or doped dielectric. Surface plasmons allow M-NPs to be employed in a broad range of applications, such as biological-labels, nanoscale biosensors, and nano-optical devices, among others.[4] Metal surface plasmons have been used to enhance the surface sensitivity of several spectroscopic measurements including fluorescence, Raman scattering, infrared absorption, and light transmission. [5]

1.3 Raman Scattering

Raman spectroscopy is a vibrational technique that provides information on chemical structures from the characteristic spectral patterns ("fingerprinting"). Raman has been widely used to determine quantitatively or semi-quantitatively the amount of a substance in a sample.[6] Unfortunately, Raman scattering is inherently a weak process (about ~ 1 million incident photons are needed to generate 1scattered photon with a Raman shift). Typical detection limits are in the parts per thousand-range and thus, it is not a sensitive technique. Surface-enhanced Raman scattering (SERS) gives an enhancement of up to 10^6 in scattering efficiency over normal Raman scattering.[6] The enhancement in Raman signals is induced by the presence of a suitable material, usually a metal, when the frequency of the exciting radiation is in resonance with the associated surface plasmon. This resonance effect creates a high-energy field near the surface of the metal and enhances many-fold the intensity of the Raman emission of the target molecule. Recent experimental evidence has shown a significant enhancement in the Raman signals of important analytes when using semiconductor nanoparticles (S-NPs) even though most SERS studies have been conducted on metal "SERS-active substrates", such as Ag, Au, and Cu which provide larger enhancements.[7-9]

1.4 SERS

The strong enhancement of the Raman signals has been attributed to "hot spots" that can be produced at points between metal particles.[10-12] Upon light excitation, electrons of individual particles are loosely held and free to couple with adjacent particles so that the plasmon is actually the plasmon of more than one particle (collective excitation). Since the SERS effect is primarily dominated by these hot spots, there has been an increasing interest to fabricate well-defined, reproducible, and controlled hot spot structures.[11-14] Some of these structures are electrode

surfaces roughened by one or more oxidation–reduction cycles,[15-21] island films deposited on glass surfaces,[22-28] films deposited by evaporation or sputtering in vacuum,[29-31] colloids (especially aggregated colloids),[32-40] and arrays prepared by lithographic techniques.[41-45]

1.5 Nanocomposite Materials and SERS

In recent years composite nanomaterials have received significant attention due to the unique and improved properties that they show over their single counterparts. The diversity in optical and electric properties of composite nanomaterials may be attributed to the proximity of components of different nature. At the interface of a semiconductor-metal composite material a polariton is generated upon surface plasmon (SPs) coupling with a photon. This polariton can propagate along the surface of a metal and in the presence of a molecule enhance the Raman scattering intensity of the molecule.

The exploitation of engineered nanocomposite semiconductor-metal hybrids for analytical purposes is an emerging field of research. The research work for this thesis started addressing the generation of "hot spots" using semiconductor-metal composite nanomaterials. Two approaches were considered: 1) titanium oxide nanoparticles capped with gold (Au-TiO_2) or silver (Ag-TiO_2) islands and self-assembled by evaporation on smooth stainless steel or gold surfaces, and 2) roughened gold films formed by chemical etching of smooth Au films deposited over p-Si/SiO_2 wafers. In the end, we have not only demonstrated the preparation of ordered arrays of "hot spots" by surface enhanced Raman—with a direct application for the detection of trace levels of explosive materials which have been studied in our research group for the past five years or so—but we have observed for the first time enhanced Raman scattering as a direct result of coupling between localized plasmons and surface polariton waves associated with the metal-semiconductor nanocomposites. We have prepared an AuNPs – TiO_2 matrix associated

with an Au coated p-Si/SiO_2 surface. The AuNPs matrix has been prepared by self-assembly of AuNPs – TiO_2 composites and characterized by AFM and Raman spectroscopy. The successful Au surfaces have been microscopically smooth Au films deposited on semiconductor wafers cut from p-Si/SiO_2 single crystals. In addition, chemical etching of the smooth Au surface with full-strength *aqua regia* under well defined conditions has been able to produce a matrix of AuNPs islands on the p-Si/SiO_2 wafers. The etched surface galleries also allowed the observation of enhanced Raman scattering with the explosive TNT and other nitroaromatic materials.

CHAPTER 2

2 LITERATURE REVIEW

2.1 Optical Properties of Metal Nanoparticles (M-NPs)

Metal nanoparticles have a characteristic optical property; they show strong absorption bands (plasmons) in the visible spectrum (Figure 1). When a resonant incident light beam interacts with the surface plasmon, induces electron oscillations on the surface of metal nanoparticles called surface plasmon resonance (SPR).[3] The oscillating field yields a strong light scattering, appearing as strong surface plasmon bands, and an enhancement of the local electromagnetic field. The frequency and the intensity of the surface plasmon absorption bands are characteristic of the type of material, and are highly sensitive to the size, size distribution, and shape of the associated nanostructures. Two distinctive properties of metal NPs are that Au-NPs show surface plasmon bands at longer wavelengths than Ag-NPs and that the corresponding surface plasmon absorption bands shifts to longer wavelengths as the size of the NP increases.[46]

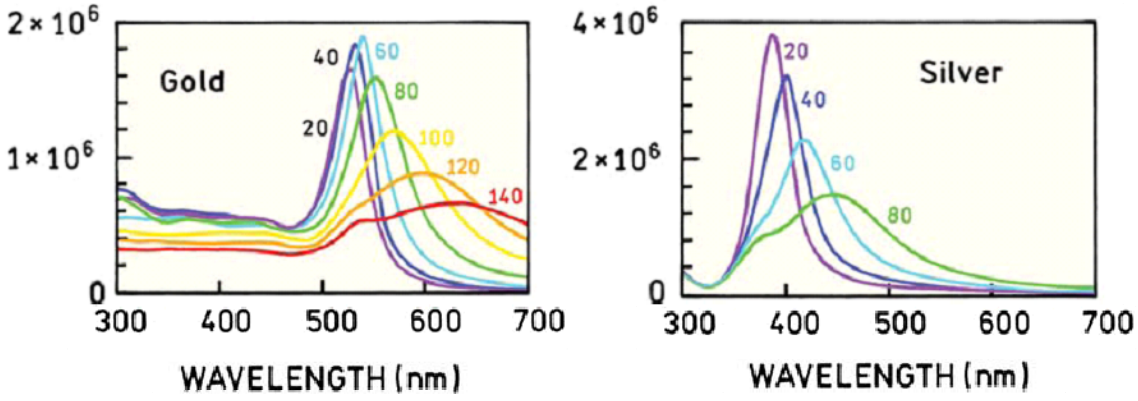

Figure 1: UV absorption spectra of gold and silver nanoparticles.

Link, S., and El-Sayed, M. A., Spectral properties and relaxation dynamics of surface plasmon electronic oscillations in good and silver nanodots and nanorods, J. Phys. Chem. B, 103, 1999, 8410–8426.

2.1.1 Surface Plasmon Resonance

The physical phenomenon of SPR was first observed by Wood in 1902.[47, 48] Wood shone polarized light on a mirror with a diffraction grating on its surface and observed a pattern of inconsistent dark and light bands in the reflected light. The first physical interpretation of the phenomenon was made in 1907 by Lord Rayleigh,[49] and further refined by Fano in 1941,[50] but a complete explanation of the phenomenon was only accomplished in 1968 when Otto[51] and Kretschmann and Raether[52] reported the excitation of surface plasmons. Application of SPR-based sensors to study biomolecular interaction was first shown in 1983 by Liedberg et al.[53] The best way to understand the excitation of surface plasmons is by explaining a simple experiment (Figure 2).

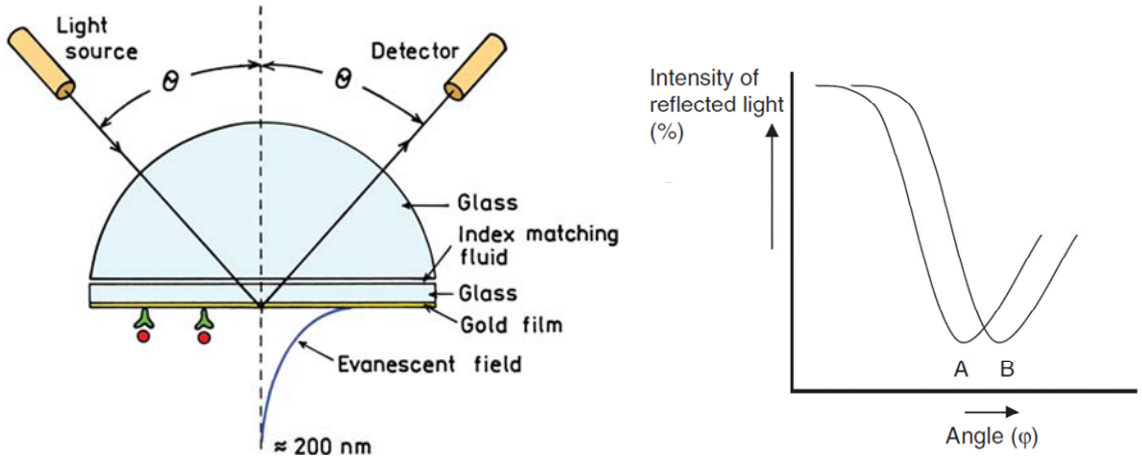

Figure 2: Schematic experimental set-up of surface plasmon resonance excitation.

At a certain angle of incidence, excitation of surface plasmons occurs, resulting in a reduction in the intensity of the reflected light (A). A change in refractive index at the surface of the metal film will cause an angle shift from A to B. C. D. Geddes and J. R. Lakowicz, Radiative Decay Engineering, Springer, 2005. A. J. Tudos and R. B.M. Schasfoort, Introduction to Surface Plasmon Resonance, Royal Society of Chemistry, 2008.

When light that has been passed through a prism interacts with a thin metal film (usually gold), the light will be reflected by the metal film acting as a mirror. When the angle of incidence is varied, and the intensity of the reflected light is monitored, the intensity of the reflected light passes through a minimum. At this angle of incidence, the light will excite surface plasmons, inducing surface plasmon resonance, causing a decrease in the intensity of the reflected light. [54] Photons of the incident light can interact with the free electrons of the metal, generating oscillation of the free electrons and consequently reducing the reflected light intensity.

The angle at which the maximum loss of the reflected light intensity takes place is called surface plasmon resonance angle (SPR angle). The SPR angle is dependent on the optical properties of the system, for example the refractive indices of the media at both sides of the metal.[54] The refractive index near the metal surface will change when a molecule adsorbs on it. Therefore the surface plasmon resonance changes and the shift of the SPR angle can be used to study the kinetics of molecular adsorption on the surface.

It has been shown that SPR is closely related to the surface plasmon coupled emission of radiation (SPCE).[46] SPCE arises when a molecule, near a continuous metallic surface, couples producing surface plasmons. If the metal film is thin and on a suitable substrate, the surface plasmons radiate their energy into the substrate. This optical phenomenon collects the emission and transforms it into directional radiation.

2.1.2 Surface Plasmon Coupled Emission[46]

Figure 3 describes the SPCE phenomenon. When an excited molecule is located above a metal continuous thin film (about 50 nm thick), the emission from the molecule is not reflected but is efficiently transferred through the film. The spatial distribution of this emission is isotropic or nearly isotropic, but the emission seen through the film occurs only at a particular angle θ_F

measured from the normal. As shown in Figure 3, the emission occurs as a cone around the z-axis. Nearly half of the emission appears in the cone and the other half is free space emission away from the film. The emission has the same emission spectrum of the molecule and is called surface plasmon coupled emission (SPCE).

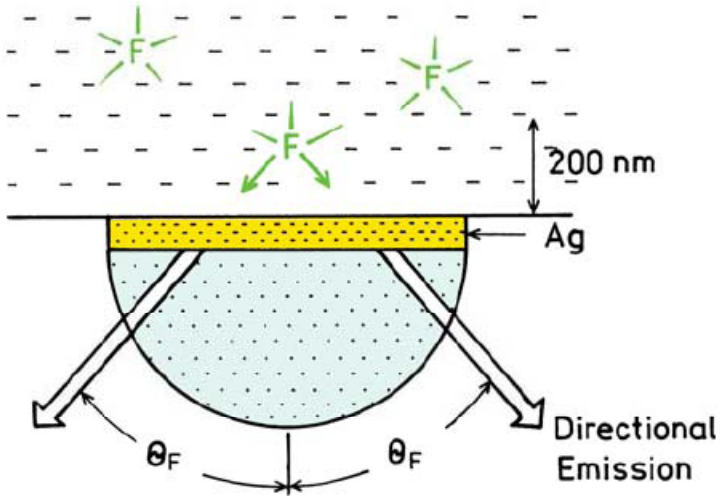

Figure 3: Surface plasmon-coupled emission. F is a molecule.

Geddes, C. D. and Lakowicz, J. R. Radiative Decay Engineering, Springer, 2005.

It is believed that the excited molecule creates surface plasmons in the metal and not the resonance energy transfer (RET) to the surface of the metal since the distances over which SPCE occurs are too large for RET. SPCE occurs over distances of up to 200 nm. In addition, the plasmons radiate into the substrate at an angle determined by the optical properties of the metal and substrate and since the wavelength distribution of SPCE is the same as the molecule emission, it is believed that it originates from the molecule. Since the emission is entirely p-polarized, even if the molecules are randomly oriented and excited with unpolarized light, this polarization indicates that the surface plasmons are radiating and not the molecule.

2.2 Raman Spectroscopy [6]

Raman spectroscopy is an analytical technique that provides chemical and structural information about materials in solution or deposited on surfaces, allowing their positive identification. Differing from rotational and vibrational spectroscopy, Raman examines the scattering, rather than the absorption of radiation. Only a small fraction of the dispersed light shows a change in frequency, as a result of the interaction of light with matter. The light fraction retaining the same frequency as the incident light is known as Rayleigh dispersion, while the fraction with different frequency is known as Raman dispersion. Two situations arise with Raman scattering, Stokes and anti-Stokes scattering (Figure 4). Stokes scattering occurs when a molecule is spontaneously excited from the ground state to a virtual energy state, and relaxes into a vibrational excited state. In anti-Stokes scattering the molecule is already in an elevated vibrational energy state, and relaxes into a vibrational excited state. Since at room temperature almost all the molecules are in the ground state, Raman scatterings gives Stokes scattering. The light frequency change in Raman scattering is attributed to the excitation or relaxation of vibrational modes. Since different functional groups have different characteristic vibrational energies, every molecule has a unique Raman spectrum.

The major limitation of Raman scattering is its inherently weak signal, which requires the use of lasers, and this leads to photodecomposition of the sample, and background fluorescence, that obscures the Raman signal. The inherently low Raman signal intensity makes target molecules in dispersed phases difficult to detect and cannot be positively identified. Such problem can be solved by using two different enhancement methods, resonance Raman enhanced scattering (RRES) involving molecular resonance and surface-enhanced Raman scattering (SERS), both acting as an efficient quencher by removing the background fluorescence.

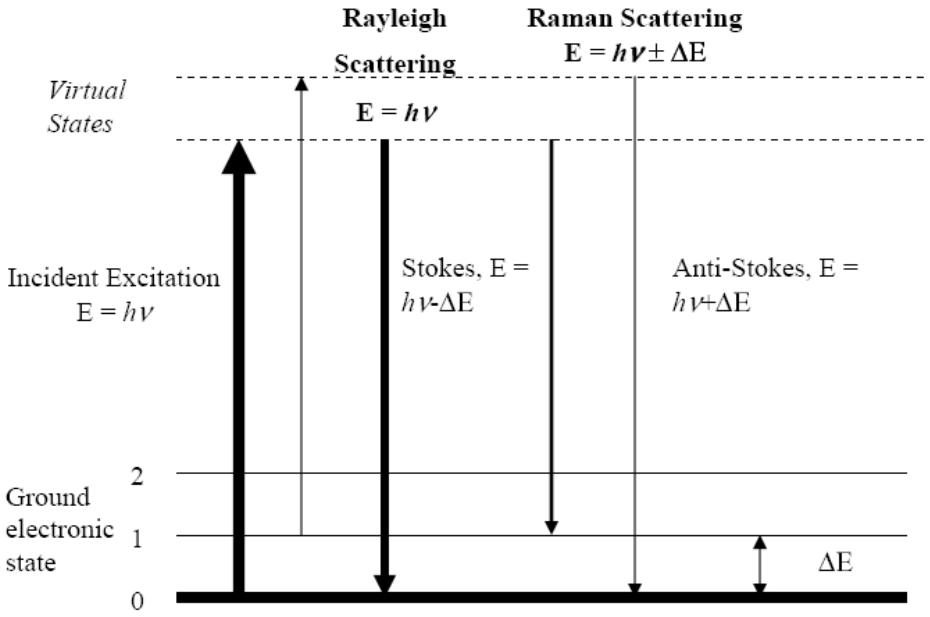

Figure 4: Energy level diagram showing the states involved in Raman Scattering.

Skoog, D.A., Holler, F.J., and Nieman , T.A. Principles of Instrumental Analysis, Orlando, FL, Saunders College Publishing, 1998.

2.2.1 Surface Enhanced Raman Spectroscopy (SERS)

Surface enhanced Raman scattering (SERS) is a sensitive and selective technique for the detection of atomic or molecular species adsorbed on nanostructured metal surfaces called "SERS-active substrates." This SERS phenomenon was first observed in the early 1970s by Fleischmann et al.[55] They observed normal Raman signals from a monolayer of pyridine adsorbed on a roughened silver electrode immersed in a simple aqueous electrolyte solution in an electrochemical cell. They claimed that just the increased surface area was responsible for the observation.

Concerning the mechanism, later on, in 1977 Jeanmaire and Van Duyne[56] successfully repeated, and significantly extended, Fleischmann experiments. They mainly tested the hypothesis that surface roughening, and thus increased surface area, was the basis of the

enhanced Raman scattering. These authors optimized the electrochemical roughening procedure and obtained 10 – 20 times more intense signals than those reported by Fleischmann. They also developed a procedure to measure the surface enhancement factor, which compared the signal intensity per molecule on the surface to the signal intensity per molecule for the same molecule in free solution and discovered the 10^5–10^6 enhancement factor associated with SERS.[56] This result ruled out the surface area hypothesis. In the same year, Albrecht and Creighton[57] independently performed and published the same experiments and obtained identical results.

Up to date, the exact effect behind SERS is not so well clearly understood and therefore it is still an active subject of investigation and discussion (see Epilogue). Nevertheless, two main components have been proposed to explain the SERS effect, namely the electromagnetic component and the chemical component. The electromagnetic effect explains the SERS enhancement by an increase in local optical fields due to resonance excitation of "hot spots" where the molecule is in close proximity with the metal surface.[15, 58] These electromagnetic resonances are due to collective excitation of conduction electrons (SPR) in the small metallic structures (Figure 5). Maximum values for electromagnetic enhancement are on the order of 10^6 – 10^7 for gold and silver isolated particles.[59, 60]

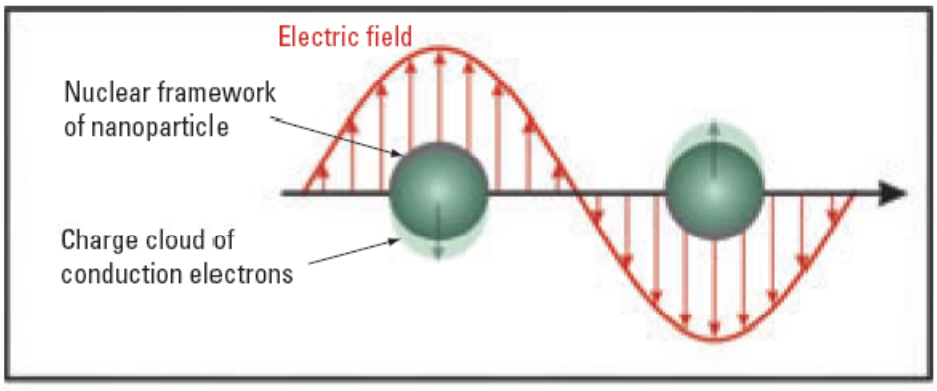

Figure 5: Illustration of the excitation of the localized surface plasmon resonance of a spherical nanoparticle by incident electromagnetic radiation.

Haynes, C. L., McFarland, A. D., and Van Duyne, R. P. Surface-Enhanced Raman Spectroscopy. Anal. Chem. 2005, 338 A-346 A.

Experimental results indicate that the SERS effect has strong molecular selectivity and specificity depending on the chemical nature of the Raman analyte, an indication of the operation of an additional "chemical" mechanism of Raman enhancement. Several theories have been proposed to explain this "chemical" effect on the Raman spectrum. One considers the electronic coupling between the adsorbed molecule and the metal. The formation of an adsorbate surface complex results in an increase in the Raman cross section of the adsorbed molecule.[61, 62] Another takes into account the resonance Raman effects that occur due to shifted and broadened electronic levels in the adsorbate molecule as a result of the influence of the metal. In addition, the "chemical" effect of SERS has been explained by direct charge transfer between the molecule and the metal.[16, 63, 64] Estimates of the contribution of the chemical enhancement of SERS have been in the range of $10 - 10^2$.[16]

2.2.2 SERS Active Substrates

Most SERS studies have been conducted on so-called "SERS-active substrates" such as Ag, Au, and Cu which provide large enhancements.[58] This is mainly due to the wavelength of the plasmon resonances. The enhancement arises when the frequency of the laser excitation is resonant with the surface plasmons on a rough metal surface. Large enhancements are obtained when the SERS active surfaces are roughened on dimensions at a scale of about 10 to 100 nm.[58] Some of these surfaces are electrode surfaces roughened by one or more oxidation–reduction cycles, island films deposited on glass surfaces, arrays of nanoparticles prepared by lithographic techniques, films deposited by evaporation or sputtering in vacuum onto cold substrates.[58]

Metal colloids have also been extensively studied as SERS substrates due to the relative simplicity in the experimental procedure to prepare them and the high SERS enhancements obtained (up to 10^6). This enhancement is influenced by colloidal stability, sensitivity to the

environment, and electro-kinetic properties.[65] The colloid characteristics can be affected when the metal particle surface experiences even small changes. Once colloidal metal particles are dispersed in solutions, they become charged as a result of the adsorption of ions and the ionization of surface functional groups. This resulting surface charge is important in SERS since the adsorption of analyte molecules onto colloidal particles is a key condition for obtaining large surface enhancement of Raman signals.

Unfortunately, the use of metal colloid has a serious problem; nanoparticles must be separated by a specific distance to obtain the SERS effect. Most of the time, the molecules of interest are suspended in solution, so the nanoparticles have to be suspended as well. Pairs of drifting nanoparticles do not create constant, reliable "hot spots," making SERS identification experiments difficult to reproduce. To overcome this problem, colloidal nanoparticles can be transferred onto solid supports. Nanoparticles in thin film form, in addition to make reproducible SERS active substrates are portable SERS active substrates, allowing *in situ* ultrasensitive chemical analysis, and single molecule spectroscopy.[66] Different approaches have been investigated for the organization of nanoparticles in thin film form. Some of the more prominent methods include self assembly by alternative deposition with a cationic polyelectrolyte,[67] silynization of a glass slide,[68] deposition on monolayers of polymer-coated substrates,[69] combination of nanosphere lithography and layer-by-layer self-assembly,[70] and self-assembly by simple solvent evaporation.[71]

Self assembly by solvent evaporation is one of the most frequently used techniques to organize colloidal particles into ordered arrays. Some of the advantages that this technique offers are simplicity, low cost, possibility to grow millimeter-sized arrays, and possibility to control the thickness of the array by varying initial suspension concentration.[72] A key factor for self-

assembly of colloidal nanoparticles is having a narrow size distribution of nanoparticles. Nanoparticle size dispersions that do not go over 5% allow self-assembly of even very small nanoparticles (1 – 20 nm).[71]

2.2.3 SERS Semiconductor Nanomaterials

For many years SERS has been limited to rough noble metal substrates, mainly Ag, Au, and Cu. However, it has been demonstrated that species adsorbed on a semiconductor can be Raman detected. L. G. Quagliano reported Raman enhancement from pyridine molecules adsorbed on InAs islands over a GaAs substrate.[7] She observed a significant enhanced Raman cross section compared to the intensity expected from the same number of non-adsorbed pyridine molecules. Based on these results, Quagliano proposed that it is possible to study adsorption and reactions of molecules on the surfaces of III-V semiconductor quantum dots using enhanced Raman spectroscopy.

Later, Y. Wang et al. reported enhanced Raman scattering from 4-mercapto-pyridine adsorbed on copper nanocrystals and Ag colloids.[8] They observed substantial differences in the Raman spectra of the 4-mercapto-pyridine molecules adsorbed on CuO nanocrystals, Cu nanoparticles, or Ag colloids, concluding that different substrates will display different interactions with the adsorbate. They also observed an excitation wavelength dependent behavior of 4-mercapto-pyridine on CuO nanocrystals. Later on, this group also reported SERS with 4-mercapto-pyridine adsorbed on CdS microclusters.[9] Here, they observed some similarities and differences in the SERS spectra of 4-mercapto-pyridine adsorbed on CdS compared with that on silver colloids.

Z. Sun et al. observed Raman scattering of 4-mercapto-pyridine and 4-mercapto-benzoic acid adsorbed on the surface of ZnO nanocrystals as a function of particle size in the range of

18–31 nm diameter and showed a large increase in Raman intensity near 28–nm diameter particles for both molecules. They believed that this effect is due to formation of a charge-transfer complex between a surface-bound exciton and the adsorbed molecule.[73]

L. Yang et al. observed surface-enhanced Raman scattering from 4-mercapto-benzoic acid, 4-mercapto-pyridine and 4-aminobenzenethiol adsorbed on TiO_2 nanoparticles.[74] They attributed the SERS obtained to a TiO_2–to–molecule charge-transfer mechanism and observed that the higher the crystallinity of the TiO_2 particles was, and thus the particles had a lower content of surface defects, the weaker were the SERS signals. This was interpreted as due to a lower capability of TiO_2–to–molecule charge-transfer. Clearly, the intrinsic semiconductor surface states (surface defects) play an important role in the TiO_2–to–molecule charge-transfer process.[74]

A. Musumeci et al. reported strong enhancement of the Raman scattering signal with a hybrid system consisting of TiO_2 nanoparticles and biologically active enediol molecules.[75] They found that a charge transfer complex is necessary for the enhancement and that the enhancement is correlated to a shift in absorption. They also observed that hybrid complexes exhibited wavelength-dependent Raman signal intensities, with the enhancement of selected vibrations and the appearance of new bands indicating that distinct binding and orientation of the adsorbed molecules on the TiO_2 surface contribute to the molecular specificity of SERS.

L. Yang et al. studied the adsorption for 4-mercapto-benzoic acid on TiO_2 nanoparticles at different pH values.[76] The highest SERS was obtained at pH 6 (no hydrochloric acid or ammonia), and they attributed this enhancement to the bonding of 4-mercapto-benzoic acid to the TiO_2 through the sulfur atom. They also observed that at pH 6 and alkaline pH the 4-mercapto-benzoic acid was bonded to the TiO_2 surface simultaneously through the sulfur atoms

and COO^- groups. The stability of the 4-mercapto-benzoic acid – TiO_2 complex was studied at different temperatures at pH 6 and found that it possesses high stability at high temperatures (150 °C). In addition, concentration-dependent experiments were performed by this group finding that the saturation concentration for 4-mercapto-benzoic acid adsorbed on TiO_2 is 10^{-3} M at pH 6.

2.2.4 SERS Metal-Semiconductor Nanomaterials

It has been demonstrated also that species adsorbed on a semiconductor material can be detected by SERS evaporating silver island films onto the surface of the material. L. G. Quagliano et al. observed SERS spectra of $[Ru(bpy)_3]^{2+}$ molecules adsorbed on glass,[77] InP,[77] silver,[78, 79] GaAs,[77-80] and Si[79, 80] substrates coated with a discontinuous Ag film. The obtained Raman enhancement had an excellent time stability and reproducibility. Raman scattering could not be detected from the surfaces without the deposited Ag film, thus they attributed this Raman enhancement to the excitation of surface-plasmon polariton modes introduced by the Ag surface roughness. Spectral differences were observed from the molecules adsorbed on the semi-conductor and on the glass and silver substrates. This evidence helped to establish that the SERS signals arises also from the substrate surface besides the Ag–islands film. The Quagliano findings show that the Ag – island technique allows use of the enhancement from the Ag – islands films to augment the Raman signal coming from the semiconductor surface. It also demonstrated that it is possible to study adsorption of molecules at low coverage on the surface of semiconductors.

TiO_2 – Ag is another semiconductor-metal hybrid that has attracted attention due to its contribution to the SERS effect. Y. Zhou et al. studied the SERS effect in TiO_2@Ag hybrid nanoparticles with a core-shell structure.[81] The hybrid nanoparticles were synthesized by reducing Ag ions over the metal-oxide semiconductor using a deep UV irradiation technique.

The observed Raman scattering bands of TiO_2 were enhanced with incorporation of Ag particles, showing that TiO_2 can be SERS active. Y. Liu e. al. observed also enhancement of the Raman scattering on TiO_2@Ag hybrids.[82] The incident laser wavelength used in this work coincided with the absorptive band of the TiO_2@Ag system; consequently the surface plasmon modes of silver clusters on TiO_2 were excited and produced a strong local electromagnetic field around the silver clusters giving a strong Raman enhancement. A. Mills et al. obtained SERS of a benzotriazole dye probe with Ag photodeposited on TiO_2 films.[83] They observed an increasing degree of SERS activity with increasing level of Ag deposition, which was controlled by the UV irradiation time. W. Ruey-Chi Wang et al. observed SERS with Ag nanoparticles loaded on a TiO_2 film/Si substrate.[84] This group also observed a size-dependent SERS effect, finding that as Ag – nanoparticles size decreases, the Raman enhancement increases. This was attributed to an increase in the density of "hot spots".

Another semiconductor-metal hybrid composite material that has been reported to be SERS active is TiO_2 – Au. Yu-Chuan Liu et al. studied the SERS of polypyrrole on a roughened Au surface prepared by oxidation-reduction cycles on rutile TiO_2 nanoparticles.[85] Interestingly, they examined the effect of simultaneous irradiation with UV light during the Raman spectrum acquisition. Higher enhancements were observed when the TiO_2 nanoparticles were incorporated on the Au roughened surface and simultaneous irradiation with UV light. Finally, T. Lana-Villarreal et al. investigated the SERS effect with deposited thin films of anatase TiO_2 nanoparticles deposited onto a roughened Au electrode and studied the adsorption of phthalic acid.[86] The observed Raman enhancement was attributed to the adsorption of phthalic acid at the internal surfaces of TiO_2 nanoporous films as well as to the enhancement of the electromagnetic field produced by the roughened gold substrate.

2.2.5 SERS Applications

SERS as a chemical detection technique has been used for a wide variety of analytes such as organics, biochemicals, and other molecules of environmental, biomedical, and pharmaceutical significance.[87-91] It has been demonstrated that minimum amounts of substances can be detected with SERS, down to the picogram level. For instance, adenine, guanine, hypoxanthine, and xanthine were separated by liquid chromatography and detected in combination with SERS.[92] Also, in a forensic science application, dye-modified cotton fibers have been studied by SERS.[93] In the field of catalysis, reduction of NO by CO on Pt and Pd substrates has been studied by SERS coupled with mass spectrometry.[94] And the explosive TNT has been detected by SERS at subpicogram levels using colloidal Ag and Au particles.[95]

Characterization of explosives by infrared absorption spectroscopy is well known and the detection is possible. Nevertheless, the IR technique is mainly limited to bulk detection and detection of small solid fragments using a microscope.[96] As a result of its limited sensitivity and the low volatility of common explosives, the existing detection limits are too high to be useful. Raman spectroscopy is an alternative vibrational technique that provides also a unique finger print for different analytes but with higher sensitivity and accuracy if properly implemented.[96] Other advantages of Raman spectroscopy over other techniques are that little or no sample preparation is required, the process is nondestructive, water can be employed as a solvent and allows simultaneous identification of components mixtures without the necessity of separation procedures.

Some common explosives of interest are 2,4,6-trinitrotoluene (TNT), cyclotrimethylene-trinitramine (RDX), octahydro-1,3,5,7-tetranitro-1,3,5,7-tetrazocine (HMX), and pentaerythritol tetranitrate (PETN) and their study is important for obvious reasons. The use of Raman

spectroscopy for the characterization of explosives was first reported by T. Urbanski while investigating the processes involved in nitration reactions.[97] This technique was severely limited at that time by high background fluorescence and poor instrument efficiency. These limitations were overcome by the improvements in the technique, like Fourier transform Raman and the development of near infrared lasers and charge coupled device detectors (CCD). J. Akhavan[98] used FT-Raman with NIR excitation to distinguish between the two major components in Semtex (a mixture of RDX and PENT). Cheng et al. demonstrated the analysis of TNT and PENT using visible lasers.[99] It was shown that explosive samples of 1 μm^3 (1 pg) can be detected from finger prints and proved that *in situ* detection is possible. As an extension study of the work of Cheng et al., Hayward et al. improved a fiber optic probe to obtain Raman spectra remotely from the spectrometer.[100] They could detect traces of PENT from fingerprints at four meters from the instrument.

Kneipp et al. reported the sensitive detection of TNT using SERS.[95] TNT concentrations of 10^{-7} M were adsorbed onto colloidal Au or Ag in aqueous solution and Raman spectra were obtained using NIR excitation. Under these conditions, vapors of TNT were not possible to detect because it was not sensitive enough. Sylvia et al. reported the vapor detection of 2,4-dinitrotoluene (2,4- DNT) by SERS using NIR laser excitation and specialized Au substrates as an indicator for the position of buried landmines.[101] They detected 2,4-DNT levels as low as 5 ppb or less with acquisition times of up to 30 s using a portable Raman system. However this system was not capable of detecting less volatile TNT due to lack of sensitivity.

Recently, N. A. Hatab et al. reported the use of Au nanoparticles as sensitive SERS substrates for detecting RDX in a contaminated groundwater.[102] They could detect RDX at concentrations as low as about 1×10^{-6} M with a SERS enhancement factor of about 6×10^4.

CHAPTER 3

3 EXPERIMENTAL PROCEDURES

3.1 General Experimental Techniques

A Cavro injector was used to prepare the colloidal TiO_2 suspensions and a magnetic stirrer Fisher Scientific Thermix 210T stirring hot plate, capable to stir at 6000 rpm. The apparatus for the photochemical deposition of noble metals onto the colloidal semiconductor particles is schematically shown in Figure 6. The photoreduction of Au and Ag onto TiO_2 nanoparticles was performed using a reaction assembly made by Ace Glass. The assembly consists of a 250 – mL borosilicate glass reactor, a 450 – W Hg immersion lamp (Hanovia medium pressure) and power supply. The suspension to be photolyzed was kept at room temperature using a VWR Scientific Model 1170 Chiller, Refrigerated Recirculator (Flow rate 3.8 L min^{-1} at 60 psig, 200 – W cooling capacity at 0 °C and 650 – W at 20 °C).

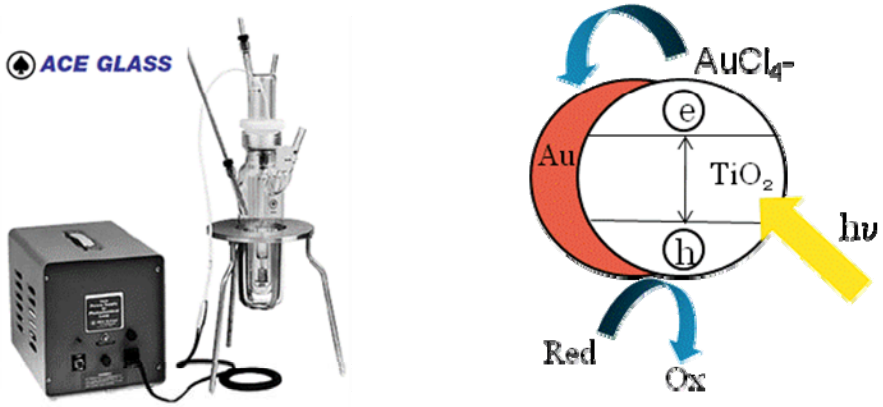

Figure 6: Photolysis reaction assembly showing a schematic photocatalytic reduction of Au onto the Titanium Oxide Particle Surface.

The characterization of the colloidal suspensions was done using a GBC UV-Vis Spectrophotometer equipped with a thermostat-temperature control and reflectance sphere. Transmission electron microscopy (TEM) was used to observe and corroborate the size and shape of the particles. Access to a TEM facility was gained by collaboration with partner institutions. Dynamic light scattering (BI-90Plus Particle Size Analyzer by Brookhaven Instruments) was used to measure the hydrodynamic particle radius and particle size distribution. The surface morphology of roughened p-Si/SiO_2/Au substrates was obtained by scanning electron microscopy (SEM, Cambridge Model 8360) and by atomic force microscopy (AFM, Digital Instruments Nanoscope III).

Raman spectra were recorded with a Renishaw Raman Model 2000 spectrometer coupled to a confocal microscope (Leica with 5x, 10x, 20x, 50x, 100x and 250x objectives). The Raman spectrometer is equipped with an integrated CCD viewing camera aligned with the microscope that allows capturing images of the sample with visible light. This is very useful feature which allows focusing the laser on the sample. The excitation source was a 785 – nm diode laser with a variable output power of up to 75 mW (Process Instruments, Inc). A nominal 2 cm^{-1} resolution was maintained to be able to detect significant shifts in the Raman spectra.

3.2 Chemicals and Solvents

All solvents were commercial grade and were used directly without further purification, with exception of water which was triply distilled when it was used as a solvent for reactions and preparation of sample solutions. The triply distilled water was obtained by demineralization of regular distilled water, provided by a 19 – liter/hour steam heated Barnstead Classic Still, with a Corning Automatic Demineralizer equipped

with an ultra-high capacity demineralizer cartridge. The demineralized singly distilled water was redistilled with an 11 – liter/hr Corning-Megapure Automatic Water Still to obtain the doubly distilled water, which was then fed to a Milli-Q Water Purification System that produces the required triply distilled water (reagent grade water, 18 MΩ.cm).

Perchloric acid (Ultrex Ultrapure Reagent, 70%) and hydrochloric acid (Ultrex High Purity) were supplied by J. T. Baker Chemical Co. Nitric acid (Reagent ACS), isopropanol (HPLC grade), and sodium citrate (Certified) were purchased from Fisher Scientific. Titanium (IV) isopropoxide (Trace Metal Basis, 99.999%), 4-nitrobenzene-thiol (Technical Grade, 80%) and 4-aminobenzenethiol (97%) were obtained from Aldrich. Hydrogen tetrachloroaurate (III) trihydrate (Reagent ACS) was from Acros Organics, 2,4,6-trinitrotoluene (99% TNT) was from Chem Service, and silver nitrate (Puratrem, 99.9995%-Ag) was from Strem Chemicals. Ethanol (95%) was supplied by Destilería Serralles.

3.3 Preparation of Colloidal TiO_2 Nanoparticles [103]

A 10% v/v titanium isopropoxide solution was prepared by adding 0.90 mL of titanium isopropoxide (3.1×10^{-3} mol) to 8.5 mL of anhydrous isopropanol under an Ar atmosphere. Colloidal TiO_2 nanoparticles were prepared by the dropwise addition of 9.0 mL of the 10% v/v titanium isopropoxide solution in isopropanol to 600 mL ultrapure water at pH = 1.5 under an Argon atmosphere and vigorous magnetic stirring. The pH of ultrapure water (18 MΩ.cm) was adjusted to 1.5 using 2 M perchloric acid (30.4 mL of 2 M perchloric acid were added to 950 mL of ultrapure water and the volume was adjusted to 1 L).The dropwise addition of the isopropoxide was performed using an automatic injector (Cavro Model 2000 dispensor), by adding 40 μL per injection every second.

Once the titanium isopropoxide was added, the mixture was stirred for one week at room temperature to reach equilibrium in particle size and particle-size distribution. The colloidal TiO_2 nanoparticle suspensions were stored in a clear vessel at room temperature.

The resulting semiconductor colloids were characterized fully by a collection of standard techniques. UV-VIS absorption spectra of the colloids were acquired to observe the characteristic TiO_2 band gap onset. For this 1.0 – mm quartz cells were used. Stability of the TiO_2 colloids was followed by UV-VIS spectroscopy as a function of time. Spectra were recorded in the range of 200 to 700 nm with a 2.0 – nm spectral bandwidth (SBW), 1000 nm/min scan speed and 0.857 nm data interval. The average hydrodynamic diameter and the particle size distribution of the TiO_2 colloids were obtained using dynamic light scattering (DLS). The as prepared TiO_2 colloid was diluted at a half with ultrapure water at pH 1.5. A disposable plastic cuvette was used for DLS measurements. TEM was used to confirm the core diameter of the colloidal TiO_2 nanoparticles. TEM grids were prepared by dropping 10 μL of the TiO_2 colloid on an ultrathin carbon film/Holey carbon 200 mesh copper grid (Electron Microscopy Sciences) allowing the solvent to evaporate at room temperature in a laminar flow hood. This procedure demonstrated to give highly stable, optically clear and highly monodispersed colloidal TiO_2 nanoparticles with 7 – 13 nm diameter and band gap onset at 325 – 350 nm (see page 33).

3.4 Preparation of Colloidal Au (Ag)/TiO_2 Nanoparticles

Au and Ag were independently photochemically reduced onto colloidal TiO_2 nanoparticles by band gap irradiation ($\lambda > 280$ nm) of TiO_2 colloidal suspensions using a

450 – W Hg immersion lamp (Hanovia medium pressure). A Pyrex absorption sleeve was employed (50% cut off at 308 nm)**.** The procedure for the preparation of colloidal Au or Ag capped TiO_2 nanoparticles consisted in adding a desired amount of an aqueous solution of hydrogen tetrachloroaurate ($HAuCl_4$) or silver nitrate ($AgNO_3$) to a 300. mL suspension of colloidal TiO_2 nanoparticles used as prepared. The Au/TiO_2 nanoparticles were prepared with two different Au loadings, 5% wt/wt and 20% wt/wt. Colloidal Ag/TiO_2 nanoparticles were prepared only with a 54% wt/wt Ag loading. For the 5% wt/wt Au/TiO_2 nanoparticles, 6.0 mL of a 5mM $HAuCl_4$ aqueous solution (3.0×10^{-5} mol) was added to a 300. mL suspension of TiO_2 nanoparticles. The 20% wt/wt Au/TiO_2 nanoparticles were prepared by adding 24 mL of 5.0 mM $HAuCl_4$ aqueous solution (1.2×10^{-4} mol) to a 300. mL suspension of TiO_2 nanoparticles. Photochemical reduction of 54% wt/wt Ag onto colloidal TiO_2 nanoparticles was done by adding 7.0 mL of an aqueous solution 9.0×10^{-2} M in $AgNO_3$ (6.0×10^{-4} mol) to a 300. mL suspension of TiO_2 nanoparticles. In all cases, prior to the irradiation, the solution was flushed with N_2 for 1 hr while stirring vigorously with a magnetic stirring bar. The mixture was irradiated for 2 hr at room temperature while maintained under nitrogen with vigorous stirring. The resulting colloidal Au or Ag TiO_2 nanoparticles were stored in an amber vessel at 4 °C.

UV-VIS spectra of colloidal Au or Ag TiO_2 suspensions were collected over time to examine the absorption-reflectivity plasmon band of the metal. The stability of the nanoparticles was studied by UV-VIS spectroscopy monitoring the position and absorbance of the absorption-reflectivity plasmon band. Spectra were recorded in the range of 200 to 700 nm under the conditions stated above. Core diameter and size distribution of the colloidal Au or Ag TiO_2 nanoparticles were obtained by TEM as

described for bare colloidal TiO_2. UV-VIS spectra of the 5% wt/wt Au/TiO_2 suspensions showed an intense adsorption plasmon band at 525 nm while the 20% wt/wt Au/TiO_2 suspensions were shifted to 540 nm (see page 48). The 54% wt/wt Ag/TiO_2 nanoparticle suspensions showed an intense adsorption band at 422 nm (see page 50).The Au/TiO_2 nanoparticles, both at 5% wt/wt and 20% wt/wt loadings, showed much greater stability than the Ag/TiO_2 nanoparticle counterpart.

3.5 Chemically Etched Au/p-Si/SiO_2 Films

A matrix of SERS-active hot spots was formed by controlled chemical etching of well-defined metal-semiconductor composite films prepared by deposition of smooth Au films on p-Si/SiO_2 wafers using standard techniques. The p-Si/SiO_2 wafers were prepared by oxidation of p-Si single crystals (7.5 cm radius, 393-µm thickness) to SiO_2 using ion sputtering giving a SiO_2 thickness of 171-µm. Then, an 8-µm thick Au film was deposited on the p-Si/SiO_2 wafer by physical vapor deposition. The actual thickness of the p-Si, SiO_2, and Au films was corroborated using SEM (see page 69). The Au surface smoothness was confirmed by optical microscopy with a 100x magnification and by atomic force microscopy (AFM).

Chemical etching was done using pure *aqua regia* prepared with reagent grade materials. In a typical procedure, *aqua regia* was produced adding small portions of a 10.0 mL solution of concentrated HNO_3 to a 30.0 mL solution of concentrated HCl (full strength) in a Pyrex beaker, stirring continuously during the addition with a glass stirring rod. The mixture was then left undisturbed for 20 min at room temperature. Immediately, the p-Si/SiO_2/Au film was immersed in the *aqua regia* so prepared for 5 s and then washed with ultra pure water (18 MΩ.cm). This step was done two times.

SEM was used to characterize the surface of the chemically etched p-Si/SiO_2/Au films. A more detailed study of the surface was done by AFM, taking images of several 20 × 20, 16 × 16, and 8 × 8 μm^2 spots to a 100×100 μm^2 area through the etched Au surface. In this fashion we corroborated that by chemical etching we obtained a rough gold surface with nanostructures of an average diameter of about 100 nm (see page 73).

3.6 Sample preparation for SERS Studies

SERS studies with the colloidal TiO_2, Ag/TiO_2 (54% wt/wt) and Au/TiO_2 (5% wt/wt and 20% wt/wt) nanoparticles were done using 4-nitrobenzenethiol (4-NBT) as probe molecule. The colloidal nanoparticles were self assembled with 4-NBT by evaporation onto the microscopically smooth Au surfaces. An aliquot of a mixture of 20 μL of the colloid and 10 μL of 1×10^{-4} M 4-NBT solution was dropped and evenly dispersed it into a circle of 4.7-mm diameter. The sample was left to evaporate at room temperature in a laminar flow hood. After solvent evaporation, Raman measurements were carried out. The colloidal particles were also self assembled on stainless steel type 316 (austenitic Cr-Ni-Mo) wafers.

Raman measurements of colloidal TiO_2, Ag/TiO_2 (54% wt/wt) and Au/TiO_2 (5% wt/wt and 20% wt/wt) were taken using a 785-nm diode laser focused by a 5x objective. The laser beam was set at 100% in the *Wire*^{TM} Renishaw Software, giving a laser power of 70-75 mW. Spectra were recorded in the Raman shift range of 100 – 2000 cm^{-1} with 10 seconds integration time and 3 averaged scans.

SERS studies on the roughened p-Si/SiO_2/Au films were performed by dropping a controlled volume of 4-aminobenzenethiol (4-ABT) or 4-NBT solutions in the concentration range 10^{-4} – 10^{-7} M. The analyte solution was evaporated at 40^0C in a

laminar flow hood for ~ 30 min. Once the sample was dried, the surface was rinsed thoroughly with ethanol and left it to dry at room temperature. Finally, the Raman measurements were carried out.

The Raman measurements of roughened p-Si/SiO_2/Au films were done using a diode laser with a 785-nm output focused by a 10x objective. The laser beam was set at 100% in the *Wire*^{TM} Renishaw Software, giving a laser power of 71-74 mW. Spectra were recorded in the Raman shift range of 100 – 2000 cm^{-1} with 10 seconds integration time and 3 averaged scans.

SERS studies with 2,4,6-trinitrotoluene (TNT) were performed with both active substrates, 1) the colloidal nanoparticles self assembled on the microscopically smooth Au surface, and 2) the roughened p-Si/SiO_2/Au films. Samples were prepared in the same manner described above with a 10^{-4} M TNT solution.

3.7 Sample Preparation for Normal Raman

Bulk samples of 4-NBT, 4-ABT and TNT were prepared for normal Raman spectra. This was done by adding a concentrated solution of the analyte in ethanol onto a microscopically smooth Au surface. For 4-NBT and 4-ABT, samples were prepared by dropping 50 μL of a 10 mM ethanol solution over an Au surface with an area of 314 mm^2. The 4-NBT sample was left to evaporate at 40 °C for ~ 30 min while the 4-ABT sample was left at room temperature overnight in a laminar flow hood. The TNT bulk sample was prepared dropping 60 μL of a 30 mM ethanol solution over an Au surface with an area of 17 mm^2. The sample was left to evaporate at room temperature for ~ 1 hr in a laminar flow hood. Once the solvent evaporated, Raman spectra were taken.

Normal Raman spectra of the bulk samples of 4-NBT, 4-ABT and TNT were

obtained using a 785-nm diode laser focused by a 10x objective. The laser beam was set at 100% in the *Wire*™ Renishaw Software, giving a laser power of 56-64 mW. Spectra were recorded in the Raman shift range of 100 – 2000 cm^{-1} with 10 seconds integration time and 3 averaged scans.

3.8 Confocal Raman Depth Profile

The observation volume of the Raman confocal microscope was characterized performing a Raman depth profiling using silicon wafers of different thickness (210 μm and 310 μm). We measured the system response to the intensity of the 520 – cm^{-1} Si band as the objective was moved along the z-axis (2000 – μm) in 20 – μm steps through the focal point (see page 77). We used the full width at half maximum (FWHM) as the depth of the confocal microscope. The depth of the bulk samples for 4-NBT, 4-ABT and TNT (as prepared in Part 3.7) was also studied measuring the system response to the intensity of a characteristic band of the molecule as the objective was moved every 20 – μm as it was scanned along the 2000 – μm range through the focal point. The bands used were the 1333, 1082 and 1365 – cm^{-1} characteristic band of 4-NBT, 4-ABT and TNT, respectively (see pages 78 and 84). In the case of both the 210 – μm and 310 – μm silicon wafers, we obtained a depth of 210 – μm. The 4-NBT, 4-ABT, and TNT bulk samples showed a FWHM (depth) of 280 – μm, 240 – μm, and 310 – μm, respectively.

3.9 Theoretical Calculations: Area of a Molecule in a Monolayer

We estimated the number of molecules of 4-NBT, 4-ABT and TNT responsible for SERS (illuminated by the laser) calculating the area that the molecule occupies in a monolayer coverage and in a maximum packing density. The initial geometries of the

molecules 4-NBT, 4-ABT, and TNT were constructed with Gaussview. The molecular geometries were optimized with Gaussian GO3 software package using the DFT method. The B3LYP function was employed in all geometry optimizations with the split valence 6-311+G (d, p) basis set. The non-bonded distances of the optimized geometries were estimated using Jmol. The distances of both ends of the molecules were calculated using van der Waals radii. The non-bonded distances obtained were used in conjunction with ACD/ChemSketch to estimate the area of closed packed molecules in a monolayer. This method was corroborated comparing the area of 4-ABT that we obtained with that experimentally obtained by A. Gole et al. [104] for a maximum coverage over an Au surface.

CHAPTER 4

4 BARE COLLOIDAL NANOPARTICLES

The possibility of single molecule detection sensitivity using SERS has stimulated new approaches for studying biologically relevant systems. This requires abundant, nontoxic, and biologically compatible materials for use as SERS active supports. So far, the majority of SERS experiments up to 2008 have been dependent on the use of metals, in particular Au and Ag nanocrystalline aggregates or the metal nanostructures present in roughened surfaces. Concerns with the biocompatibility of these useful, but otherwise toxic materials, as well as the desire to extend the applicability of SERS to other materials, has spurred a large effort to extend SERS to semiconductor materials. One such material is TiO_2 in various forms, including colloidal nanoparticles. The availability of such materials and the access to research groups with state-of-the-art laboratory know-how and techniques prompted us to explore the applicability of bare colloidal TiO_2 nanoparticles in solution as SERS active supports.

4.1 Preparation of Colloidal TiO_2 Nanoparticles

Colloidal TiO_2 nanoparticles were synthesized by the sol-gel hydrolysis technique of Dawson and Kamat. [103] This involves the dropwise addition of a titanium isopropoxide solution to a bulk acid solution. The procedure seems simple enough to be carried out using standard laboratory techniques without more precautions than to add the isopropoxide dropwise to a vigorously stirred acid solution. Initial attempts in this laboratory and elsewhere were a complete failure in terms of suitable colloidal nanoparticles. The available literature does not detail well how the dropwise addition of the titanium isopropoxide must be done for a successful synthesis. This seemed and seems to be a trade secret. Consequently, we encountered several difficulties

with the initial use of a standard dropping funnel. In particular, the addition time and the drop size were difficult to control. After many unsuccessful trials that provided milky suspensions, we decided to use an automatic injector (Cavro Model 2000 dispensor) capable to do well-defined additions. The most consistent results were obtained by injecting the isopropoxide (9.00 mL, 1.00 mM isopropanol solution) at a rate of 40 μL per injection per second to a vigorously stirred aqueous perchloric acid solution (600 mL in a 1-L round bottomed flask) under a N_2 atmosphere at room temperature. In this fashion, we obtained consistently a near optically clear TiO_2 colloidal suspension that was stirred at room temperature for a week to reach equilibrium.

Our two major findings for the successful preparation of colloidal TiO_2 by the hydrolysis method are the following. On the one hand, we have the requirement of oxygen exclusion during the preparation of the TiO_2 colloid. This is critical if it is to be used for photochemical or electrochemical experiments. The presence of molecular oxygen, which adsorbs readily onto the colloidal particle, causes severe interference, particularly with the photoreduction of noble metals such it is in our case (*vide infra*). On the other hand, in spite of some literature preparations suggesting the use of hydrochloric acid for the hydrolysis of the titanium isopropoxide, it has been our experience that poor results are usually obtained due to the known aggregation properties of chloride ions. We have found that indeed the ideal electrolyte for work with colloidal TiO_2 suspensions is perchloric acid. Perchlorate ions have almost no tendency to aggregate the semiconductor colloidal particles, which remain in this medium for months if left undisturbed from external causes.

The as prepared optically clear suspensions showed in the UV-VIS spectrum a flat baseline with an onset of the semiconductor band gap between 325-350 nm (Figure 7). The colloid was highly monodisperse as determined by dynamic light scattering (DLS), the standard technique

commonly used to estimate the average hydrodynamic particle size as a measure of the turbidity exhibited by colloidal suspensions. The preparations of TiO_2 showed consistently a particle size distribution of 7 – 13 nm diameter with a mean diameter of 10 nm, in good agreement with the values reported in the literature. Figure 8 shows the TEM image of TiO_2 nanoparticles, which confirms the 10 nm mean diameter.

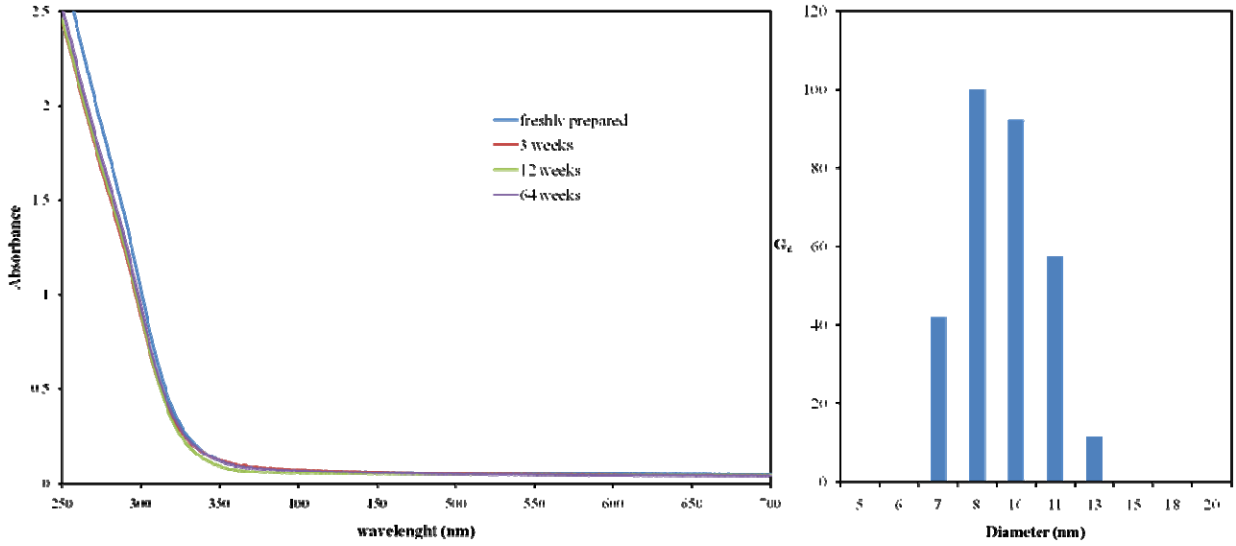

Figure 7: UV-VIS absorption spectra of colloidal TiO_2 nanoparticles up to nearly a year and a half (left), and particle size distribution by volume (right).

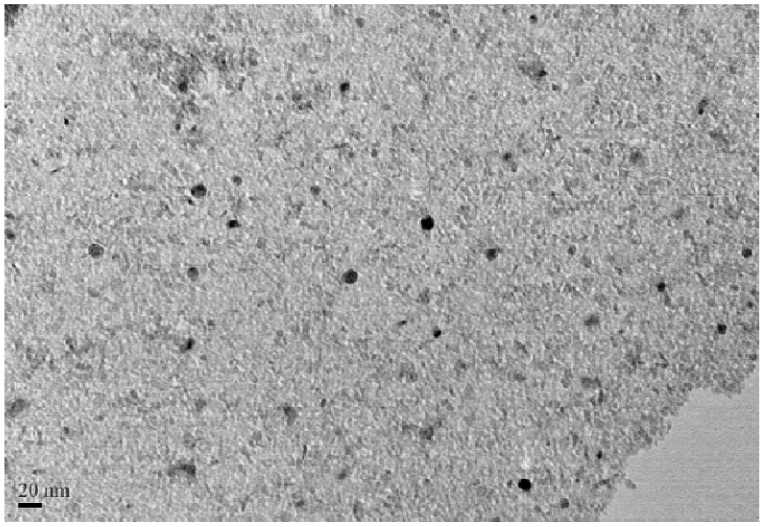

Figure 8: TEM image of colloidal TiO_2 nanoparticles.

4.2 Attempts at SERS with Bare Colloidal TiO_2 Nanoparticles

Initially, SERS was attempted with 4-nitrobenzenethiol (4-NBT) and 2,4,6-trinitrotolune (TNT) with colloidal TiO_2 nanoparticles in the liquid phase. 4-NBT was chosen, on the one hand, as a SERS probe molecule due to its large Raman cross section and strong chemisorption ability of the thiol group. On the other hand, TNT was studied due to its popularity in the SERS community since it is a commonly used explosive and there is a particular interest in its identification and detection at trace levels. Aliquots of the undiluted TiO_2 suspensions (800. μL) were mixed with 100. μL of a 10^{-4} M 4-NBT aqueous solution in a 2 – mL vial, shaken in a vortex apparatus for 30 seconds and then transferred to a 1 – mm capillary tube. These experiments were unsuccessful with the excitation lasers available, λ = 514 nm, and 785 nm.

Since this direct method did not show any Raman enhancement at all, in another experiment we subsequently added 100 μL of salt (NaCl or KCl) to the 4-NBT–colloid mixture. This was done at different concentrations (5×10^{-2} – 1M) to induce partial aggregation. However, under these conditions none of the analytes of interest showed any hint of Raman enhancement at any excitation wavelength. These trials with and without salt aggregation were done at the original pH of the colloid (pH 1.5). We interpreted that the SERS failure was due to a misbalance in the electrical double layer charge between molecule and colloid. Molecular charge is a key factor to promote surface binding and complex formation to generate surface states within the laser excitation power in the visible. The surface of colloidal TiO_2 has a positive potential at pH 1.5. Thus, molecules may interact with the TiO_2 nanoparticles when they are negatively charged or have a negative functional group. The charge of 4-NBT was modified adjusting the pH of the mixed suspensions to pH 7 and 11 with ammonium hydroxide and perchloric acid. At neutral pH the thiol group of 4-NBT will be partially deprotonated ($-S^{\delta-}-H^{\delta+}$) whereas at basic pH it will

be fully deprotonated (– S^-). Our best hope was to obtain SERS at pH 7 because at pH 11, when the thiol group bears a full negative charge, the colloid is also negatively charged and again there would be strong particle-to-molecule repulsion at the double layer and it would inhibit complex formation. SERS experiments were done as described above but, unfortunately, again no Raman enhancement was observed.

In spite of all our best efforts to detect Raman enhancement with bare colloidal TiO_2 particles, all attempts were unsuccessful. Recently, well after this work was completed, reports by Tijana Rajh et al. (2011)[105] have appeared detailing the observation of SERS on hybrid TiO_2-molecular composites in liquid suspension, but with very modest enhancement factors (less than about 10^3). These successful experiments, together with the theoretical single-unified treatment of the SERS effect published earlier by Lombardi and Birk (2009), bear direct clues as to why our initial experiments with 4-NBT and TNT were so unsuccessful (see Epilogue). One reason is the absence in the bare semiconductor particle of surface-plasmon resonances in the visible. The second is the inability of our analytes to bind and form charge-transfer states on the semiconductor surface. These authors, as well as most investigators in the field, now agree that there are three possible sources for the Raman enhancement. The one, most often cited, is the existence of surface plasmon resonances (SPR) due to the collective excitation of the electrons in the conduction band of the particle. This would require band-gap excitation of the semiconductor for positive SERS. The second most important contribution is the chemical or charge transfer (CT) mechanism between the molecule and the conduction band of the particle. When orbital mixing occurs between the molecular orbitals of the analyte and the orbitals which constitute the conduction band of the nanoparticles, the result is a charge transfer complex that leads to a shift in the effective band gap of the material to a lower energy. This charge transfer can occur in

either direction depending on the relative energies of the semiconductor Fermi level and the HOMO and LUMO levels of the adsorbed molecule. The third possible contribution is due to resonances within the adsorbed molecule itself. None of these mechanisms are likely to work with the analytes of interest and the colloidal semiconductor in liquid suspension.[16, 63, 64, 105]

The positive SERS results observed by Tijana Rajh et al. with bare colloidal TiO_2 are due to the specificity of the dopamine type analytes they used. The surface plasmon resonance of most semiconductors is located in the infrared region, which is far from the 514 or 785-nm excitation lines used in our experiments. Therefore, the semiconductor SPR cannot be a contribution for SERS with bare semiconductor particles. This leaves the chemical mechanism (CT) and molecular resonances on the particle surface as the two other possibilities to contribute to SERS with bare semiconductors, but this requires, as stated earlier, very specific molecular interactions with the semiconductor surface as is the reported case between TiO_2 and dopamine by Tijana Rajh et al. Enhancement of the Raman signals was observed with dopamine absorbed on the surface of bare TiO_2 nanoparticles.[75, 106] Tijana Rajh et al. observed a red shift in the band gap of the TiO_2 with the TiO_2 surface-modified by dopamine and attributed it to charge transfer from dopamine to TiO_2. The relationship between the observed CT absorption shifts and the Raman enhancement was clearly demonstrated. When the excitation energy was below the energy of the charge transfer complex, Raman enhancement was not observed. These results suggest that the charge-transfer complex state was in resonance with the laser when SERS was observed.

The theoretical explanation proposed by this group for the TiO_2 – dopamine system is summarized in Figure 9. It basically involves charge transfer from the molecule to the TiO_2 particle. Dopamine binding onto the TiO_2 surface results in charge transfer and the appearance of

surface states within the TiO_2 band gap which reduces the TiO_2 excitation energy to 1.6 eV (776 nm). This allows excitation from the midgap state to the conduction band with radiation of a frequency lower than the band gap of bare TiO_2 (3.2 eV at 388 nm). Therefore, to be able to observe SERS with bare semiconductors, a charge transfer complex has to be formed between the molecule and the semiconductor surface. Formation of a CT complex under these conditions depends on the surface properties of the semiconductor, the frequency of the excitation, and the specific nature of both the molecule and the semiconductor. We, therefore, conclude that SERS studies based on the molecule-to-semiconductor charge transfer model is very limited and difficult to extend to the type of analyte of interest for further applications at this time.

L. Yang et al.[76, 107] have further clarified this aspect of SERS with bare semiconductor particles. They observed again modest enhancements of the Raman signals with 4-mercapto-benzoic acid (4-MBA), 4-mercapto-pyridine (4-MPY) and 4-aminothiophenol (PATP) adsorbed on TiO_2 nanoparticles. Here, a blue shift in onset of the TiO_2 band gap was observed when they

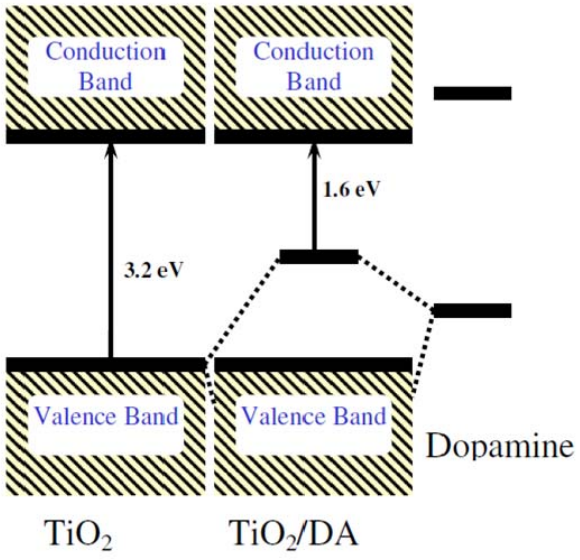

Figure 9: Schematic presentation of dopamine to TiO_2 charge transfer.

Musumeci, A., Gosztola, D., Schiller, T., Dimitrijevic, N. M., Mujica, V., Martin, D., and Rajh, T. SERS of Semiconducting Nanoparticles (TiO_2 Hybrid Composites). J. Am. Chem. Soc. , 131, 2009, 6040–6041.

modified the surface of the TiO_2 particles by immobilization of the analytes by precipitation. It can be concluded that this blue shift is the result of TiO_2 – to – molecule charge transfer. Stronger SERS signals were obtained with increasing electron attracting ability for the groups para to the thiol group (4-MBA > 4-MPY > PTAP), thus demonstrating that the SERS observed was a result of a charge transfer complex. To examine whether the TiO_2 surface states are involved in the charge transfer process, they performed SERS experiments varying the crystallinity of the TiO_2 particles. The enhancement of Raman signal of 4-MBA decreased with increasing TiO_2 crystallinity (lowering surface defects). Therefore, it can be concluded that the charge transfer process depends on the nature of the adsorbed molecules and the surface properties of the semiconductor. It can be theorized that the charge transfer involved excitation of the valence band electrons of TiO_2 to surface state energy levels by the incident light with the sub-band gap energy (2.7 eV at 459.7 nm) and then injected into the LUMO of the adsorbed molecules (Figure 10).

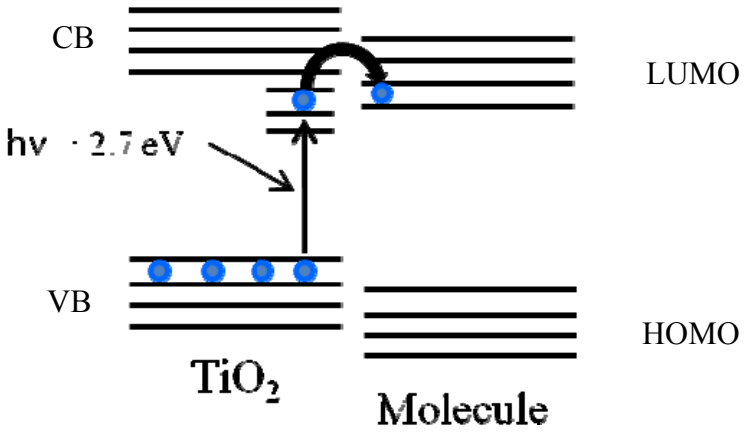

Figure 10: Charge transfer between the adsorbed molecule and TiO_2.

Adapted from L. Yang et al. Observation of Enhanced Raman Scattering for Molecules Adsorbed on TiO_2 Nanoparticles: Charge-Transfer Contribution. J. Phys. Chem. C, 112, 2008, 20095–20098.

4.3 Attempts at SERS with TiO_2 Nanoparticles over Composite Au Films

The following attempt was made to create surface states on TiO_2 nanoparticles by self-assembly over Au films deposited on p-Si/SiO_2 wafers. The most successful Raman-signal enhancements have been observed for well defined "hot spots" on noble metal structures. In metals, "hot spots" are produced at points between particles. Nanoparticles drifting suspended in solution are hard to pin down in a controlled manner, thus they do not make a good base for constant, reliable "hot spot" structures. Therefore, we came up with a different approach to fabricate SERS active "hot spot" structures: namely by self assembly of the bare semiconductor nanoparticles by evaporation onto smooth metal surfaces. Two metal systems were tried in succession: 1) microscopically smooth Au films deposited on p-Si/SiO_2 wafers and 2) stainless steel Type 316 (austenitic Cr-Ni-Mo).

Several trials were made before we realized that it was quite likely that a major component was missing. In our first approach to this experiment, a 30 – μL aliquot of the TiO_2 nanoparticle suspension was dropped and evenly dispersed into a 4.7-mm ID metal circle confined within the smooth metal structure. The colloid was left to evaporate at room temperature in a laminar flow hood. Over the resulting smooth semiconductor film, we dropped 5 – 30 μL aliquots of a 10^{-4} M 4-NBT aqueous solution which was evenly dispersed on the dry colloid. Raman measurements were done right after evaporation of the solvent. Unfortunately, enhancement of the Raman signal was not observed in this case either. In a second trial, aliquots of a mix of the nanoparticle suspension with 10^{-4} M 4-NBT aqueous solution were dropped and evenly dispersed within the 4.7-mm ID metal circle. The samples were allowed to evaporate at room temperature in a laminar flow hood. Raman measurements were attempted after solvent evaporation with negative results. To complete the study we tried 4-NBT/TiO_2 mixes with different solution ratios: 25 μL

of the colloid with 5μL of 4-NBT, 20 μL of the colloid with 10 μL of 4-NBT and 15 μL of the colloid with 15 μL of 4-NBT. Unfortunately, Raman enhancement was never observed under these conditions.

4.4 Colloidal Metal Nanoparticles

Since the most successful SERS studies have been reported with metal based substrates, it was worthwhile to explore this possibility before abandoning the bare particles approach to SERS. The dominant contribution to SERS with metal nanoparticles is the SPR or electromagnetic mechanism, which consists on the generation of a high local field near the metal surface. Thus, for operation of the SPR mechanism molecules do not have to be adsorbed on the surface but restrained in the vicinity of the local field near the surface. Consequently, SERS with metal nanomaterials was a more promising approach.

Noble metals in colloidal form seemed a good alternative to the TiO_2 nanoparticles in suspension or in thin films. We immediately found that colloidal metals have been extensively used in SERS studies due to the simplicity in their preparation and the high enhancements observed, usually in the range of 10^6. It has been established that the Raman enhancement is determined by the metal colloid stability and the surface charge on the particles. Typically, colloidal metal nanoparticles are prepared by reduction of the metal ions from their salts. We attempted to prepare stable colloidal Ag nanoparticles by the method of Lee and Meisel.[32] In this method, silver nitrate ($AgNO_3$) is reduced by sodium citrate in a hot aqueous solution. We attempted also to prepare stable colloidal Au nanoparticles by reduction of tetrachloroaurate ions ($AuCl_4^-$) with sodium citrate as reported by Turkevich and coworkers.[108] In spite of our best efforts and great interest, it proved practically impossible to prepare any consistently stable and well defined metal nanoparticles that might be candidates as active SERS substrates. It is

concluded that although the chemical reduction methods may seem convenient for the preparation of colloidal metals, they are very difficult to implement in a practical manner. Particle formation depends heavily on solution conditions, such as the rate and sequence of reducing agent addition, and the local over concentration of the reducing agent. The colloids prepared in this fashion were highly unstable and heterogeneous. Moreover, the excess of reducing agent and the resulting oxidation products are actually contaminants of the final material. So even if we had been lucky in obtaining stable, monodisperse colloidal metal nanoparticles, they would not have been suitable for SERS studies since for this technique to be successful, it is important to have substrates that are free of contaminants to avoid contaminant-analyte competition for the adsorption sites. In consequence, we decided to abandon this approach altogether in favor of better defined and more controllable synthetic methods.

CHAPTER 5

5 COMPOSITE SEMICONDUCTOR-METAL NANOPARTICLES

The theoretical and practical experience acquired during the execution of the experimental work described in the previous chapter provided us with a much deeper understanding of the key conditions to achieve SERS. It was soon realized that we needed to prepare a different type of material incorporating simultaneously several components that would allow the three Raman enhancement mechanisms to operate in turn. Notwithstanding the desirability to use bare semiconductor materials for biocompatibility reasons, the best surface plasmon resonators are metals and have to be incorporated into the substrate for efficient operation of the SPR mechanism. The charge-transfer mechanism requires the formation of surface states on the semiconductor and this can be promoted by the presence of an active metal forming a metal-semiconductor junction capable to interact with the analytes of interest. The nature of the underlying substrate surface plays also an essential role for active SERS. The substrate surface can 1) be inactive under the observation conditions, 2) quench the electronic excited states responsible for Raman or 3) can further enhance the localized SPR on the particles by coupling with a delocalized surface plasmon polariton or plane delocalized plasmon.

These considerations led us to search for practical, efficient methods to prepare metal-semiconductor nanocomposites using the available facilities and experimental capabilities. The new methods had to yield materials that were homogeneous, free of contaminants and incorporate noble metals with varied mass composition. Since during the execution of the bare particle work described above we found an efficient and consistent method to prepare stable and highly monodispersed colloidal TiO_2 particles, this was the semiconductor of choice for the rest of the work. In terms of metals, Ag is preferable over Au because Ag surface chemistry is better

known than Au chemistry. However, this preference is offset by the much less noble nature and instability of Ag over Au, which immediately becomes the metal of choice. There are still some considerations against the use of Au because it is well known for its ability to quench the fluorescence of the analyte, i.e., it quenches the same electronic-excited state responsible for Raman scattering. Nevertheless, we persisted in the use of Au because quenching is effective in close proximity by a radiationless mechanism and SPR operates by an electromagnetic mechanism in the near field. Finally, in terms of fabrication procedure, a photochemical reduction method was sought since this would provide an *in situ* clean synthesis with full control of metal loading, irradiance, and wavelength.

5.1 Photo-deposition of Au on n-TiO_2 Nanoparticles

This part of the research has been a tremendous success for this project since, as we relate below, with Au/n-TiO_2 particles, under the right observation conditions and on the correct underlying substrate, the desired observation of enhanced Raman signals could be successfully realized. We will describe in detail the rationale and theoretical background behind this approach since it was in this way that we arrived successfully at this SERS active system.

Firstly, we consider again the benefits of the photochemical synthesis compared to the thermal reaction. The photo-reduction of metal ions does not require the use of an excess of reducing agent which will later compete with the analyte for active sites on the surface of the substrate. In addition, photochemistry offers other advantages such as 1) the reaction takes place uniformly in the solution 2) radiation of the right frequency can be selected to be absorbed by the target species despite the presence of other light absorbing solutes or products, and 3) the rate of reaction is well known, since the number of reducing equivalents generated by radiation is well defined.

Secondly, we look at the theoretical background of why such a photochemical synthesis would be possible and how it would have to be performed to be successful. The photochemistry of wide-band semiconductor materials is well known for single-crystals. Photochemical reactions take place on the semiconductor surface by photo generated conduction-band electrons and valence-band holes. It has been a marvel of science to discover that by decreasing the size of simple materials to the nanometer length or below, quantum effects are generated and most materials at this size show novel and improved characteristics.

Insulators have the valence band full of electrons while the conduction band is empty. The gap between the valence band and the conduction band (band gap) is considerably large so no net motion of charge results from the application of an electric or electromagnetic field (Figure 11). On the other hand, in metals the valence band and the conduction band are adjacent to each other. Electrons travel freely through the metal since the energy needed to promote a valence electron to the conduction band is negligible. This freedom of electron movement results in very high conductivities of the metals. In semiconductors the situation is similar to that in insulators, except that the band gap is smaller and electrons can be thermally or electromagnetically promoted to the conduction band.[109] Promotion of electrons from the valence band to the conduction leaves a positively charged vacancy in the valence band, which is referred to as a "hole". These holes can move through the semiconductor by transfer of one electron to the vacancy, therefore holes are also charge carriers.

Generation of charge carriers within a single-crystal semiconductor can be done by adding small amounts of impurities to the semiconductor, the process called "doping".[72] The simplest example of this involves the introduction of a group V element (P, As, Sb) or of a group III element (B, Al, Ga, In) to a group IV element like Si. If the impurity provides conduction

electrons (group V element), the majority carriers within the semiconductor are electrons and the semiconductor is of *n-type*. Contrary, if the impurities are electron acceptors by adding a group III element, holes are the dominant charge carriers and the semiconductor is of *p-type*. However, when the size of the material is reduced to the nanometer length, no formal doping process as such is needed to behave as semiconductor with improved properties.

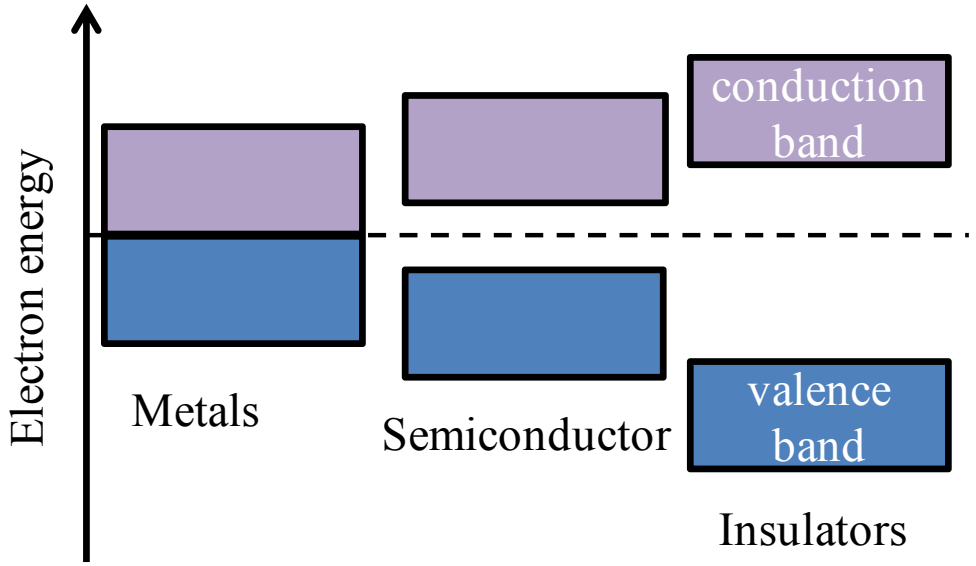

Figure 11: Diagram of the electronic band structure of metals, semiconductors, and insulators.

Colloidal TiO_2 in liquid suspension have thus semiconductor behavior. When a semiconductor is present in an electrolyte solution, an electric double layer emerges at the semiconductor/solution interface.[109] This electric double layer develops when the electro-chemical potential of a solution—determined by the redox potential of the electrolyte—and the electrochemical potential of the semiconductor—determined by its Fermi level—do not lie at the same energy. The charge movement across the interface leads to an establishment of thermodynamic equilibrium between the two contacting phases.[109] The Fermi level, the highest energy level occupied by electrons at a temperature of absolute zero, is located just below the

conduction band in an *n-type* semiconductor, whereas in a *p-type* is located just above the valence band. The Fermi level of an *n-type* semiconductor is usually higher than the redox potential of the electrolyte; hence electrons are transferred from the semiconductor to the solution. Therefore there is a positive charge associated with the electric double layer which is reflected in an upward bending of the semiconductor band edges (Figure 12). On the other hand, *p-type* semiconductors have a Fermi level lower than the redox potential of the electrolyte and thus electrons move from the solution to the semiconductor. This creates a negatively charged electric double layer causing a downward bending of the semiconductor bands edges.

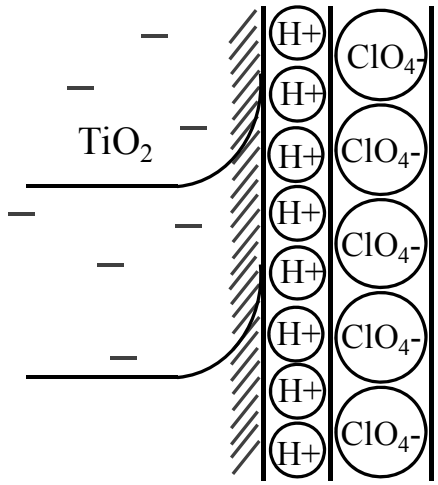

Figure 12: The schematic structure of the electric double layer at the semiconductor/electrolyte interface (*n*-TiO_2/$HClO_4$).

Band gap excitation of colloidal n-TiO_2 particles under these conditions would result in the promotion of electrons from the valence band to the conduction band, generating a "hole" and an electron (Figure 13). The hole is a strong oxidizer; the empty orbitals must retrieve the electron density just lost after light absorption, whereas the electron promoted to the conduction band is a strong reductant, capable to reduce metal ions to atomic metals. Taking into account all of this information, the following experiments were carried out resulting in the successful

preparation of the colloidal Au/n-TiO_2 nanocomposite particles. Eventually, these nanoparticles provided the basis for highly successful Raman enhancement experiments with our analytes.

5.2 Preparation of Au Islands on n-TiO_2 Nanoparticles

Typically, the photochemical reactor system described in the experimental part was charged with 300. mL of stable colloidal TiO_2 particles at pH 1.5 with the required amounts of chloroauric acid ($H^+AuCl_4^-$) to obtain the desired Au loadings. The resulting yellow colloidal suspension was stirred vigorously under a stream of N_2 bubbles for 1 h while cooled to 18°C with a cooling recirculator set at that temperature. The mixture was irradiated with a 450 – W Hanovia medium pressure Hg lamp through a Pyrex filter (50% cut off at 308 nm) for 2 h. Following photolysis, the reaction mixture was allowed to cool, filtered through a glass wool plug and analyzed by electronic spectroscopy. Nanoparticles with 5% and 20% wt/wt Au loading showed an intense plasmon band at 526 nm and 539 nm, respectively, which is the characteristic region where colloidal Au nanostructures show the plasmon oscillations bands (Figure 14). The stability of the 5% wt/wt and 20% wt/wt colloidal Au/TiO_2 nanoparticles was studied by monitoring the plasmon oscillation band using UV-VIS spectroscopy. The colloids have shown to be stable for more than a year now. For instance, the Au/TiO_2 colloid with a 5% wt/wt Au loading did not show any significant changes in plasmon band intensity or position. Absorbance values were in the 0.075 – 0.078 per mm range and the position fixed in 526 nm. The 20% wt/wt Au/TiO_2 colloid has been stable for almost one and a half years. Absorbance values in this case have decreased from 0.20 to 0.18 per mm and the band position stayed around 539 nm.

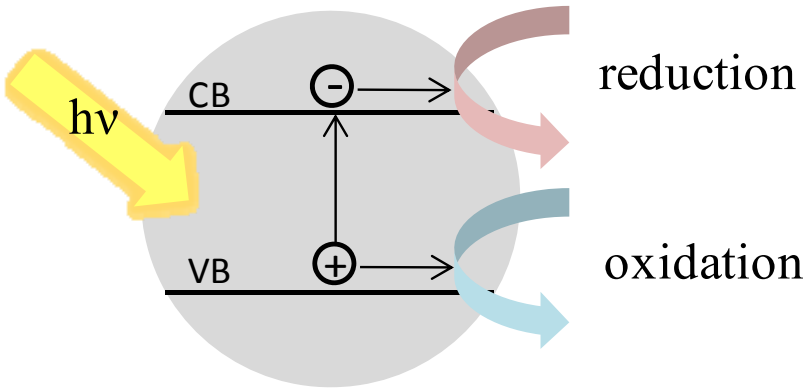

Figure 13: Band gap excitation of the semiconductor TiO_2 particle by UV light absorption.

The chemistry behind the preparation is as follows. In the absence of any other materials, water on the surface of the semiconductor can be oxidized to hydroxyl radicals by the TiO_2 holes generated by band gap irradiation. Hydroxyl radicals would be further oxidized to molecular oxygen. However, in the presence of a secondary alcohol such as isopropanol, the electron-deficient hole will preferentially oxidize the hydroxyl group of the alcohol to the acetone carbonyl group. The redox potential of secondary alcohols is more positive than the redox potential of water. Actually, the oxidation of water is thermodynamically very demanding:

$$2\ H_2O \rightarrow O_2 + 4\ H^+ + 4\ e^- \qquad 1.2\ V\ vs\ SHE\ (pH\ 0)$$

The theoretical potential required to drive water oxidation falls to 0.82 V at pH 7. In practice, however, mechanistic complexity coupled with a substantial activation barrier means that a large electrochemical overpotential is needed to drive this reaction. Typical water electrolyzers therefore operate at ca. 2 V.

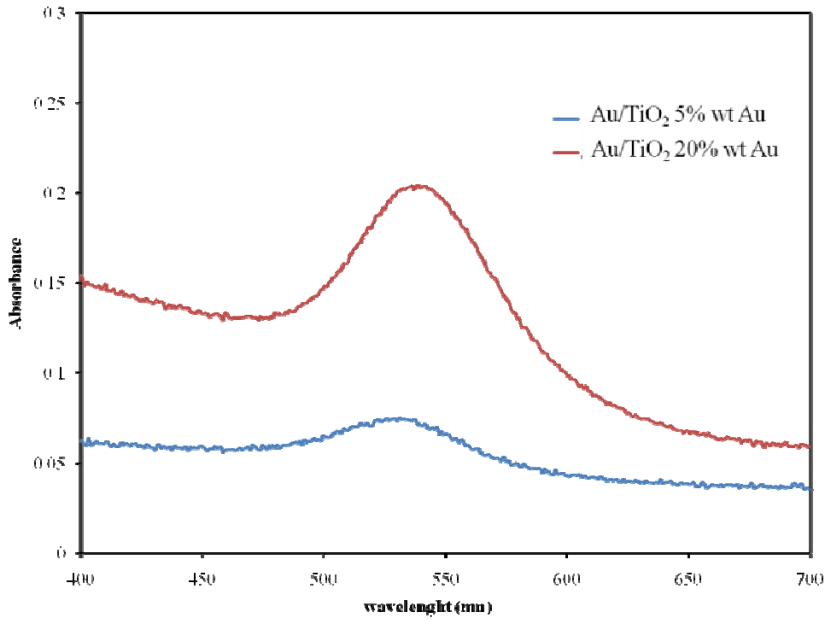

Figure 14: Plasmon oscillations bands of Au/TiO_2 5% wt/wt and 20% wt/wt Au (1mm path).

The fate of the photoelectron promoted to the semiconductor conduction band is as follows. The positive charge associated with the electric double layer responsible for the upward bending of the semiconductor band edges (Figure 12) facilitates at pH 1.5 the adsorption of the $AuCl_4^-$ ions to the TiO_2 nanoparticles replacing ClO_4^- ions. Upon band gap irradiation, the photo-generated electrons in the conduction band migrate to the TiO_2 surface and reduce the adsorbate ions. This produces the first few Au atoms which act as catalysts for the ensuing faster photo-deposition reaction resulting in the formation Au atom clusters on the surface of the TiO_2 particle (Figure 15).

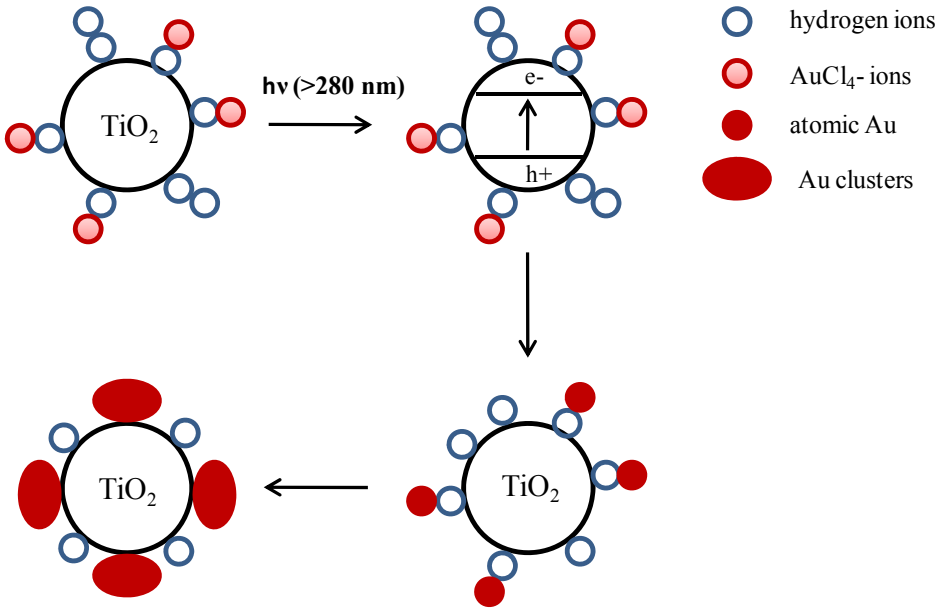

Figure 15: Schematic photochemical reduction of $AuCl_4$- ions on the surface of colloidal TiO_2 nanoparticles.

Adapted from W. Chuanyi et al., Chi. Sci. Bull., 43, 210-213, 1998.

The photo-deposition reaction is likely to follow the reaction scheme shown below.

$TiO_2 + h\nu \rightarrow h_{vb}^+ + e_{cb}^-$	Charge Separation
$e_{cb}^- + [AuCl_4]^- \rightarrow Au_{(s)} + 4Cl^-$	Atomic Metal Generation
$h_{vb}^+ + (CH_3)CH\text{-}OH \rightarrow (CH_3)_2CO + H_2O$	Acetone Generation
$h_{vb}^+ + H_2O \rightarrow \bullet OH$	•OH Generation
$\bullet OH + (CH_3)CH\text{-}OH \rightarrow (CH_3)_2CO + H_2O$	Acetone Generation

5.3 Full Characterization of Au Doped TiO_2 Nanoparticles

The amount of Au metal deposited on the colloidal TiO_2 particles was determined using as a reference the number of metal atoms needed to obtain a full coverage on the TiO_2 surface. This requires comparing the number of metal atoms per TiO_2 particle for a full surface coverage with the occupancy indices (O.I), i.e., the average number of metal atoms per TiO_2 particle, for different concentrations of the metal ions. The number of metal atoms per TiO_2 particle for a full

coverage was determined by dividing the surface area of a TiO_2 nanoparticle by the area that the metal atom project on the surface:

$$\frac{4\pi r_{TiO_2}{}^2}{\pi r_{metal}{}^2}$$

where r_{TiO_2} and r_{metal} are the average radii of the TiO_2 particles and metal atoms, respectively. Using the average particle radius of 50 Å determined by dynamic light scattering and the atomic radii of 1.44 Å for both Au and Ag, the number of metal atoms per TiO_2 particle for a full coverage is 4.82×10^3.

The occupancy index of metal atoms per TiO_2 particle was obtained by:

$$\frac{[M]_{atoms}}{[TiO_2]_{particle}}$$

where [M] and $[TiO_2]_{particle}$ are the molar concentrations of metal atoms and molar TiO_2 particle concentration, respectively in the total reaction volume. The TiO_2 particle concentration was estimated by:

$$[TiO_2]_{particle} = \frac{[TiO_2]}{\theta}$$

where $[TiO_2]$ and θ are the stoichiometric TiO_2 concentration and the average number of TiO_2 molecules per particle, respectively. From the bulk molar density (ρ_M in mol cm^{-3}) and the molar particle volume (V_M in cm^3 mol^{-1}), we obtained:

$$\theta = \rho_M \times V_M$$

$$\text{with} \quad V_M = \frac{4}{3} \times \pi \times {R_0}^3 \times N_A$$

where R_0 is the particle radius and N_A is Avogadro's number.

Dynamic light scattering gives the hydrodynamic volume of the TiO_2 nanoparticles while electron microscopy provides the core volume. Therefore, one must use the core TiO_2 radius in

combination with the bulk density of the semiconductor. Since our colloidal TiO_2 nanoparticles showed a average core radius of 50 Å, the molar particle volume is 8.65×10^5 cm^3 mol^{-1}. Using the bulk density of TiO_2 (3.84 g cm^{-3}), we find that each particle contains about 4.15×10^4 TiO_2 units. Since the stoichiometric TiO_2 concentration in our experiments is 4.98×10^{-3} M, this provides a TiO_2 particle concentration of 3.29×10^{-7} M.

Table 1 shows the occupancy indices of Au atoms per TiO_2 particle obtained upon photolysis of $AuCl_4^-$ solutions with different concentrations (% wt/wt). Enough Au was photo-reduced amounting from 0.88% to 100% Au wt/wt for percentage Au coverage ranging from 1.1% to 120%. Due to the catalytic nature of the Au atoms initially reduced on the particle surface, full monolayer Au coverage of the TiO_2 surface is out of the question. Therefore, clusters and metal islands are likely to be formed on the TiO_2 surface. Moreover, the metal cluster – to – metal cluster negative repulsion potential would even prevent these Au islands to be close together.

Of all the colloidal Au/TiO_2 nanoparticles prepared, the more stable were those with 5% Au wt/wt and 20% Au wt/wt (6.3% and 24% monolayer coverage, respectively). This is in good agreement with the inter-island repulsion model because when there is monolayer coverage larger than 24% a strong repulsion results between neighboring Au clusters which leads to desorption of the Au clusters into the bulk of the solution. Both 5% Au wt/wt and 20% Au wt/wt particles showed an intense plasmon band at 526 nm and 539 nm, respectively as shown above in Figure 14. The stability over time of both colloids was monitored by UV-VIS spectroscopy using this band. Figure 16 shows the plasmon oscillations band for the 5% Au wt/wt colloid from when it was freshly prepared until nearly about a year. It can be observed (inset Figure 16b) that for the 5% wt/wt loading the plasmon band position and intensity did not change significantly over time.

Table 2 lists these results in more detail. Absorbance values were in the 0.075 – 0.078 range and the band maximum was fixed at 526 nm. Figure 17 shows the spectra for the 20% Au wt/wt colloid collected for almost over one and a half years. The spectra (inset Figure 17b) show a slight change in the intensity of the plasmon band for this loading (a decrease from 0.20 to 0.18 absorbance units) with a position of the band maximum at around 539 nm. Table 3 summarizes these results.

% wt	*Occupancy*	*% of coverage*
0.88	54	1.1
5.0	303	6.3
8.7	520	11
14	910	19
20	1100	24
39	2400	50
61	3700	76
99	5800	120

Table 1: Concentration, occupancy indices and percent of coverage of Au atoms on colloidal TiO_2.

Further characterization of the Au/TiO_2 colloids with 5% Au wt/wt and 20% Au wt/wt has been done by transmission electron microscopy (TEM). Figure 18 shows TEM micrographs obtained for both colloids. It can be seen that the particles so prepared have Au and show a mean core diameter of 26 nm and 34 nm, respectively.

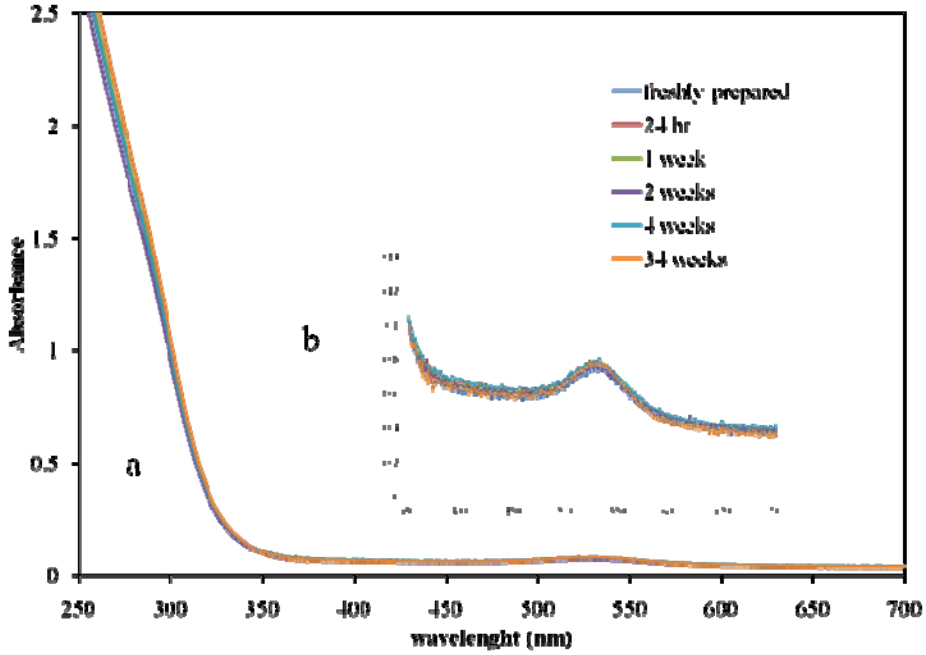

Figure 16: UV-VIS absorption spectra (1mm path) of a) Au/TiO_2 with 5% Au wt/wt nanoparticles b) Au absorption plasmon band region of Au/TiO_2 with 5% Au wt/wt, over time.

Weeks	*Absorbance*	*Plasmon position (nm)*
0	0.075	526
1	0.078	526
2	0.075	526
4	0.079	526
34	0.078	526

Table 2: Values of absorbance (1 mm path) and position of the Au/TiO_2 with 5% Au wt/wt absorption plasmon band over time.

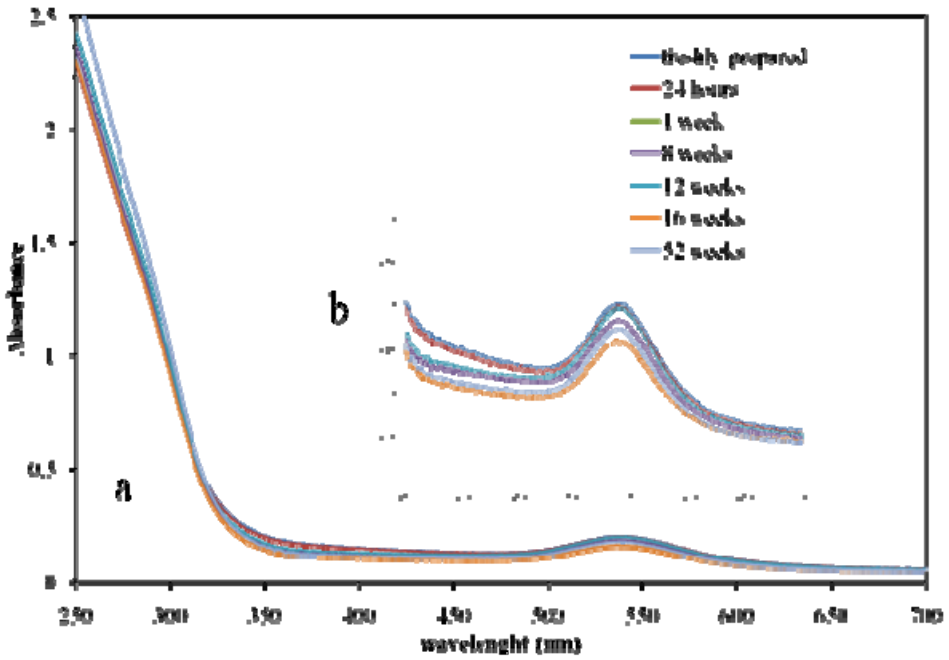

Figure 17: UV-VIS absorption spectra (1 mm path) of a) Au/TiO_2 with 20% Au wt/wt nanoparticles b) Au absorption plasmon band region of Au/TiO_2 with 20% Au wt/wt, over time.

Week	*Absorbance*	*Plasmon position (nm)*
0	0.20	539
1	0.20	539
8	0.19	538
12	0.19	539
16	0.18	539
52	0.18	539

Table 3: Values of absorbance (1 mm path) and position of the Au/TiO_2 with 20% Au wt/wt absorption plasmon band over time.

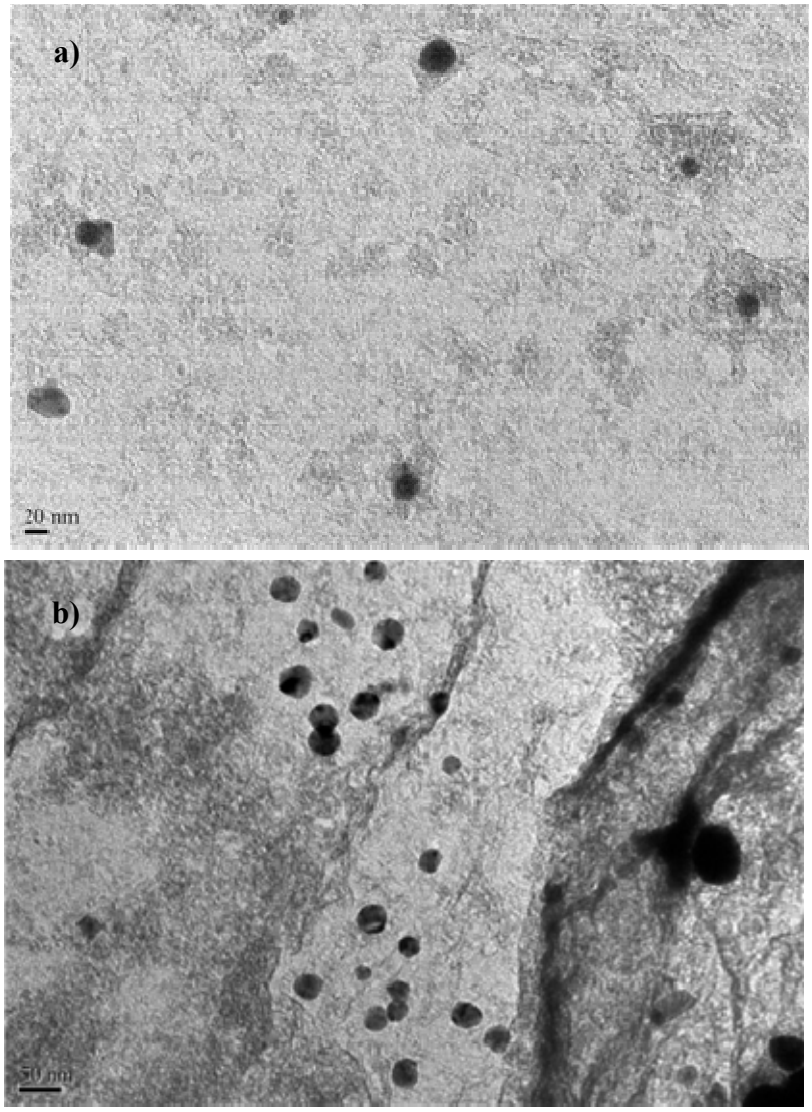

Figure 18: TEM image of colloidal Au/TiO_2 nanoparticles: a) 5% Au wt/wt, b) 20% Au wt/wt.

5.4 Preparation of Ag Islands on n-TiO_2 Nanoparticles

For the reasons already stated (*vide supra*), Ag was the second metal of choice for the preparation of metal-TiO_2 nanocomposites. The metal ion precursor available was $AgNO_3$ which in solution provides plainly hydrated positively charged Ag ions. This in principle poses a problem for successful photo-reduction on the semiconductor since to reach the surface of the TiO_2 particles, the Ag ions have to exchange the firmly bound double-layer protons. Anticipating this situation, we decided to increase the chemical potential of the Ag ions in the bulk of the solution adding an excess of $AgNO_3$ to force the Ag ions in closer proximity to the TiO_2 surface and facilitate the photo-deposition of Ag islands. In the manner described for the Au nanocomposites, a 54% Ag wt/wt colloidal suspension of TiO_2 nanoparticles was band-gap irradiated for 2 h. The 54% wt/wt metal loading represents 1.5 times the amount needed for a full Ag coverage (125% coverage). The resulting colloidal Ag/TiO_2 suspension showed an intense plasmon oscillation band centered at 422 nm (Figure 19). The stability of the Ag colloid was studied in the same manner using UV-VIS spectroscopy. Figure 19b shows the electronic spectra since when the colloid was freshly prepared to nearly over a year. This Ag colloid was stable for just three weeks when the position of the plasmon band shifted from 423 nm to 421 nm and the absorbance decreased 0.04 units per mm. Table 4 summarizes these results in more detail. Most Ag ions did not photo-reduced on the surface of the TiO_2 nanoparticles and it was quite evident that a mixture of colloidal Ag and TiO_2 particles was obtained. Colloidal Ag particles are extremely unstable due to the less positive oxidation potential of Ag compared to Au. It is well known that Ag metal objects tarnish readily under conditions where Au is stable.

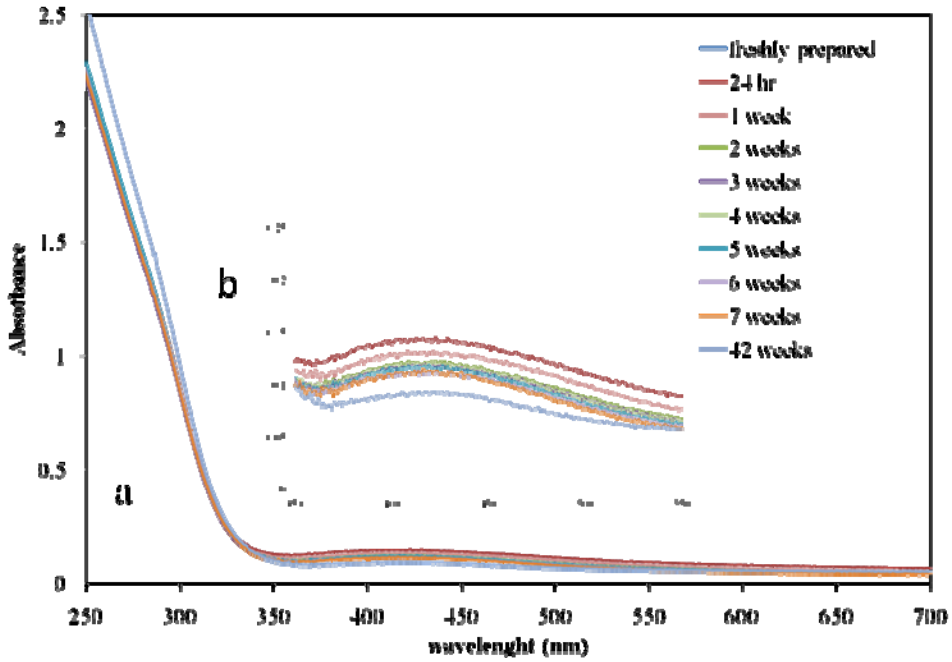

Figure 19: UV-VIS absorption spectra (1 mm path) of a) Ag/TiO_2 with 54% Ag wt/wt nanoparticles b) Ag absorption plasmon band region of Ag/TiO_2 with 54% Ag wt/wt, over time.

Weeks	*Absorbance*	*Plasmon position (nm)*
0	0.15	423
1	0.13	423
2	0.12	423
3	0.12	421
4	0.11	421
5	0.12	419
7	0.11	420
42	0.09	421

Table 4: Values of absorbance (1mm path) and position of the Ag/TiO_2 with 54% Au wt/wt absorption plasmon band over time.

5.5 Raman Experiments with Noble Metal Loaded n-TiO_2 Nanoparticles

Following the full characterization of the metal doped TiO_2 nanoparticles with the available nanomaterial characterization techniques, SERS studies were performed with the particles in colloidal suspension (Ag/TiO_2 54% wt/wt and Au/TiO_2 5% wt/wt and 20% wt/wt) as described earlier for bare colloidal TiO_2. The lack of success in the earlier experiments motivated in this case the use of 4-NBT (4-nitrobenzenethiol) as Raman probe molecule. The rationale to use this thiophenol was not only for its larger Raman cross section and strong chemisorption ability of the thiol group but also for its ability to self assemble into a close packed monolayer on a noble metal surface. The same standard procedure for Raman experiments was followed as detailed previously (Section 4.2), but unfortunately no enhancement of the Raman signals was observed in this case either.

5.6 Initial SERS Experiments by Self Assembly

The frustrating results in the search of a simple, inexpensive way to induce SERS in a nonspecific manner highly motivated us to further analyze the remaining variables in the system that might have been overlooked in our initial analysis. As stated earlier, the strongest Raman enhancements have been observed when large arrays of "hot spots" are produced at points between particles. Particles drifting in solution are hard to pin down into fixed positions and thus they do not make constant, reliable "hot spots" during the Raman experiment. Consequently, a different approach was needed and this consisted in generating active "hot spots" structures by self assembly of colloidal nanoparticles by evaporation onto suitable underlying substrates.

The selection of the underlying substrate was again a frustrating quest since SERS still resisted to manifest itself in a glorious manner. All sorts of underlying substrates were examined, from glass slides to smooth stainless steel and aluminum. Eventually we arrived at the use of

microscopically smooth Au films deposited on p-Si/SiO_2 wafers. In this case, the intently sought Raman enhancement manifested itself in the form of strong SERS. Subsequently, we tried as underlying substrate a special stainless steel, Type 316, austenitic stainless steel with Cr-Ni-Mo. In both cases enhancement of the Raman signals was recorded upon: 1) dropping an aliquot of a mixture of the metal loaded particles (20 μL, stock) with 4-NBT in aqueous solution (10 μL of 10^{-4} M stock); 2) evenly dispersing it into a 4.7-mm ID circle; 3) letting the sample evaporate at room temperature in a laminar flow hood.

5.6.1 Initial SERS Experiments with TNT

Once we observed Raman enhancement of 4-NBT with the self assembled colloidal nanoparticles, we immediately performed SERS experiments with TNT using the same successful preparation method. The TNT molecule does not possess a functional group that allows a strong sorption on to the metal surface like 4-NBT does, but we believed that it could interact with the metal *via* the para nitro group (4-NO_2). To further clarify the experimental variables affecting the SERS phenomenon, we studied the effect of the electrical charge on the functional groups of 4-NBT and TNT.

The initial charge of the molecule was modified adjusting the pH of the 4-NBT and TNT 10^{-4} M aqueous solutions. The pH was adjusted to 7 and 11 using perchloric acid and ammonium hydroxide. The surface of the metal loaded colloidal TiO_2 particles is positively charged at the preparation pH of 1.5. Thus, molecules will interact strongly with the surface through a negatively charged group. Since the pKa of 4-NBT is 5.1,[110] the thiol group at pH 1.5 is fully protonated (99.9% –SH), whereas at pH 7 is deprotonated (98% $–S^-$), and at pH 11 it would be 100% ionized. Deprotonation of the thiol group is known to increase its affinity for noble metal and semiconductor surfaces. Therefore, larger Raman enhancements of 4-NBT were likely to be

observed at higher pH values. The TNT molecules are a different story due to its much lower acidity, pKa H_2O 13.6.[111] The nitro groups are strongly polarized ($– N^{\delta+}O_2^{\delta–}$) irrespective of pH value; therefore they are expected to be much less sensitive to pH changes. TNT is expected to interact with the metal or semiconductor surface with the para (4-NO_2) group since molecular models show the existence of severe steric hindrance between the 2,6-nitros and the CH_3 group ortho to them. At pH 11 the CH_3 group in the TNT benzene ring is 0.25% deprotonated ($–CH_2^{--}$) forming the 2,4,6-trinitrobenzyl anion which could possibly help in the metal-semiconductor interaction. So even at higher pH values, it is more likely that TNT will interact with particle surface via its para NO_2 group since any approach to the surface through the $–CH_2^–$ anion will experience severe steric hindrance. Specific molecular interactions of TNT and 4-NBT with the self assembled nanoparticles were confirmed in the observed SERS spectra.

5.6.2 Rationale for the Self-assembled Experiments

The rationale behind the successful observation of enhanced Raman by self assembly of metal-loaded nanoparticles on the microscopically (micron size) smooth Au films on p-Si/SiO_2 wafers is as follows. Firstly, these wafers contain a semiconductor-metal junction on a Si based substrate. Secondly, the laser can induce electron oscillations on the semiconductor-metal junctions (plasmon). Thirdly, these electron oscillations delocalize in the continuous Au metal film generating a delocalized plasmon or so called polariton which induces a highly enhanced local field. Lastly, when the highly enhanced local field of the polariton couples with the localized surface plasmons of the metals on the TiO_2 surfaces, they induce the enhanced emission of light with the Raman shift of the analyte. In summary, in these experiments the laser photons play a three pronged roles: 1) they provide the photons needed to induce the polariton in the underlying semiconductor-metal junction of the substrate, 2) they serve as the excitation

source to induce the localized plasmons within the metal-semiconductor junction of the particle, and 3) they are the photons scattered by the analyte bearing the fingerprint of its ro-vibrational spectrum manifested as a Raman shift.

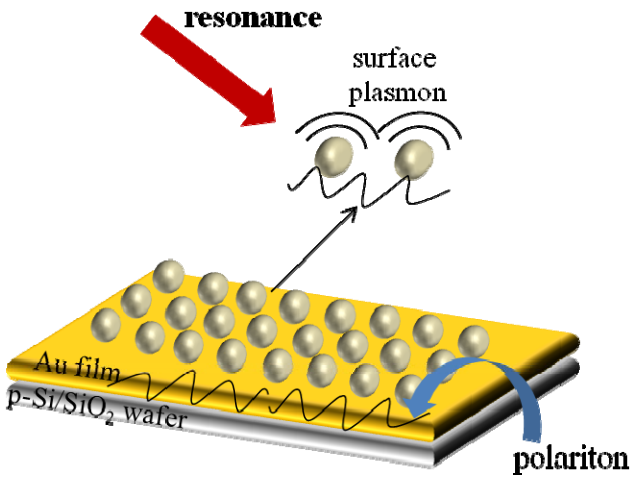

Figure 20: Surface plasmon and polaritons generated on self assembled metal-semi-conductor nanoparticles on microscopically smooth Au films on p-Si/SiO_2 wafers.

5.7 Raman Experiments with 5% wt/wt Au/TiO_2 Self Assembled Nanoparticles

The Raman enhancement of 4-NBT was observed as described above and detailed in the experimental part using self assembled colloidal TiO_2 nanoparticles loaded with 5% wt/wt Au. The analyte-nanoparticle suspension was allowed to self-assemble both onto the microscopically smooth Au films on p-Si/SiO_2 wafers and onto the austenitic stainless steel Type 316. In Figures 21 and 23 we show the SERS spectra of 4-NBT at acid pH obtained with 5% wt/wt Au loading deposited on the Au and austenitic substrates, respectively. In both Figures we show from top to bottom the Raman spectra of (a) 4-NBT ~5.76×10^{-9} mol/cm^2 at neutral pH with Au/TiO_2 5% Au wt/wt, (b) Au/TiO_2 5% Au wt/wt, and (c) 4-NBT ~5.76×10^{-9} mol/cm^2 at neutral pH. The thiol group (–S–H) of 4-NBT at pH 7 will be fully deprotonated and is expected to be chemisorbed more strongly on Au than the fully protonated thiol group. Appearance of the prominent SERS peak at 1337 cm^{-1}, assigned to the symmetric stretching vibration of the –NO_2 group suggests

that the chemical environment of the group did not change much when the 4-NBT molecule was near the Au surface, confirming that the 4-NBT molecule strongly interacts with the Au surface via the thiol group. SERS peaks at 724 and 857 cm^{-1} arises from the C–S stretching and the C–H ring wagging. Peaks at 1082 and 1112 cm^{-1} are mainly from the in-plane C–H ring bend vibration. The peak around 1575 cm^{-1} is due to the C–C ring stretching. Figures 22 and 24 show the Raman spectra of 4-NBT on smooth Au films and stainless steel at neutral pH (a), and the normal Raman spectrum of 4-NBT (b). In summary, there was a good correlation between the normal Raman spectra of 4-NBT and the observed SERS spectra (Table 5).

ν (cm^{-1})			Assignment
SERS		Raman neat	
p-Si/SiO_2/Au	Stainless steel		
724 m	724 m	724 m	C–S stretching
857 m	856 m	856 m	C–H wagging
1082 s	1081 s	1080 s	C–H bending
1112 m	1112 m	1110 m	C–H bending
1337 vs	1340 vs	1340 vs	NO_2 symmetric stretch
1574 s	1575 s	1572 s	C=C stretching

Table 5: Raman vibrational modes of 4-NBT in the bulk and SERS of 4NBT with Au/TiO_2 5% Au wt/wt nanoparticles on microscopically smooth Au films on p-Si/SiO_2 wafers and stainless steel Type 316 at neutral pH.

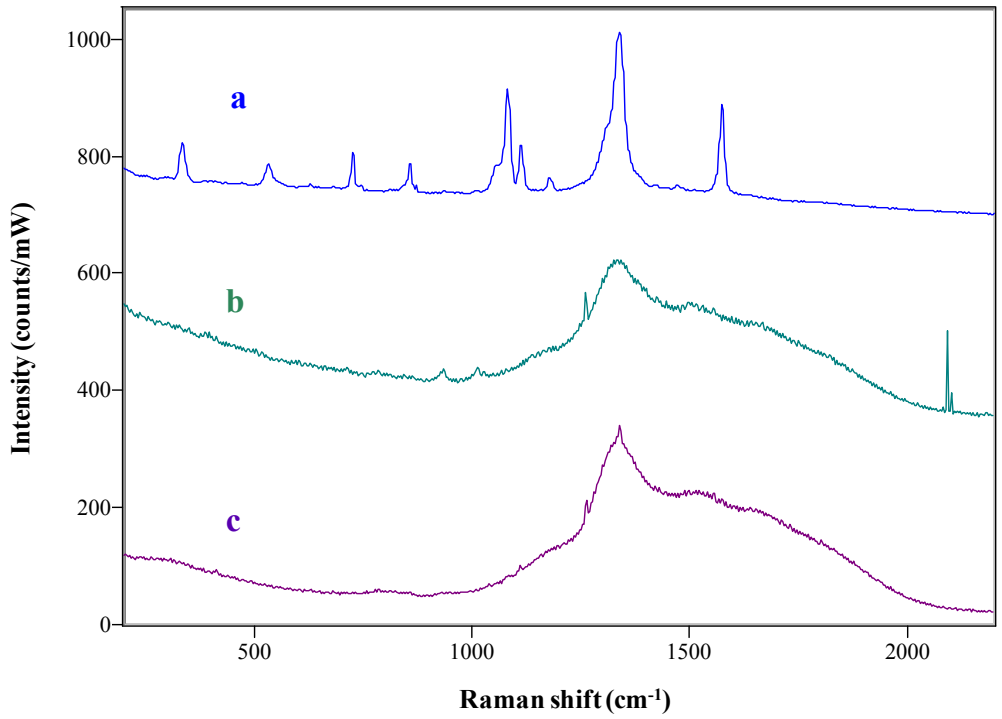

Figure 21: Raman spectra on microscopically smooth Au films on p-Si/SiO_2 wafers: a) 4-NBT ~5.76 × 10^{-9} mol/cm^2 (neutral pH) with Au/TiO_2 5% Au wt/wt; b) Au/TiO_2 5% Au wt/wt; c) 4-NBT ~ 5.76 × 10^{-9} mol/cm^2 (neutral pH). Data normalized to laser power.

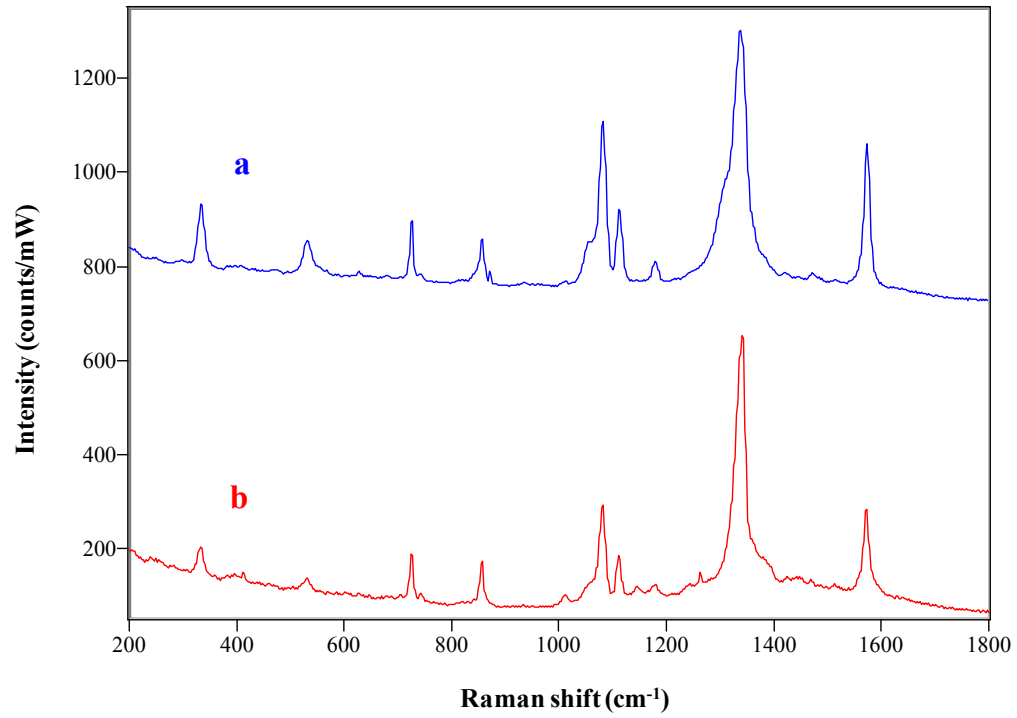

Figure 22: Raman spectra on microscopically smooth Au films on p-Si/SiO_2 wafers: a) 4-NBT ~5.76 × 10^{-9} mol/cm^2 (neutral pH) with Au/TiO_2 5% Au wt/wt; b) normal Raman spectra of neat 4-NBT. Data normalized to laser power.

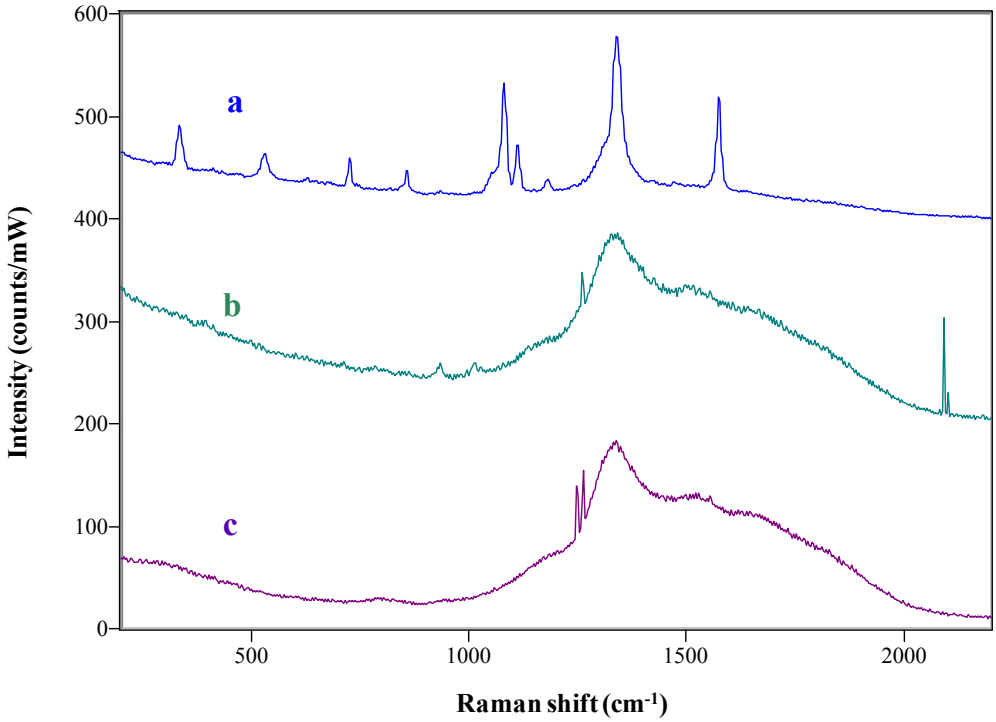

Figure 23: : Raman spectra on stainless steel Type 416: a) 4-NBT ~5.76 × 10^{-9} mol/cm^2 (neutral pH) with Au/TiO_2 5% Au wt/wt; b) Au/TiO_2 5% Au wt/wt; c) 4-NBT ~ 5.76 × 10^{-9} mol/cm^2 (neutral pH). Data normalized to laser power.

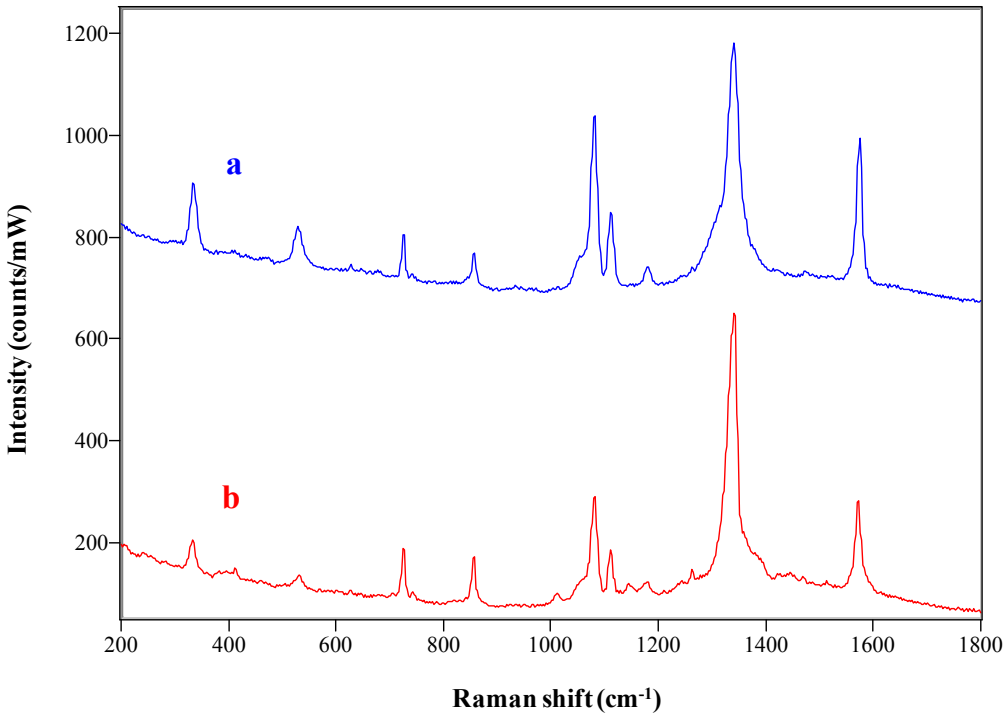

Figure 24: Raman spectra on stainless steel Type 316: a) 4-NBT ~5.76 × 10^{-9} mol/cm^2 (neutral pH) with Au/TiO_2 5% Au wt/wt; b) normal Raman spectra of neat 4-NBT. Data normalized to laser power.

When we changed the analyte to TNT using still the self-assembled Au/TiO_2 5% wt/wt nanoparticles no enhancement of the Raman signal was observed in either the smooth Au films or the austenitic stainless steel at any pH value. As anticipated, the TNT molecule does not possess groups with high affinity for Au like the 4-NBT molecule does; hence interaction of TNT with the Au/TiO_2 nanoparticles would be very weak at this loading. Therefore, anticipating that the SPR electromagnetic mechanism was going to be more important, presumably dominant, for SERS with TNT and considering the inherently lower Raman cross section of TNT, we concluded that the local field generated near the Au surface by surface plasmons was not going to be capable to enhance the extremely week Raman signals. Consequently, we decided to increase the amount of Au photo-deposit onto the colloidal TiO_2 nanoparticles, foreseeing that the higher loading will produce a more intense local field.

5.8 Raman Experiments with 20% wt/wt Au/TiO_2 Self Assembled Nanoparticles

The same experiments were done with Au/TiO_2 20% Au wt/wt nanoparticles with both 4-NBT and TNT. Raman enhancement with 4-NBT was observed again when self assembled on the colloidal Au/TiO_2 nanoparticles over our microscopically smooth Au films on $p\text{-}Si/SiO_2$ wafers and over austenitic stainless steel. The SERS spectra of 4-NBT at neutral pH with Au/TiO_2 20% Au wt/wt on $p\text{-}Si/SiO_2/Au$ and austenitic stainless steel are show in Figures 25 and 27, respectively. In both Figures we show from top to bottom the Raman spectra of (a) 4-NBT $\sim 5.76\times10^{-9}$ mol/cm^2 at neutral pH with Au/TiO_2 20% Au wt/wt, (b) Au/TiO_2 20% Au wt/wt, (c) 4-NBT $\sim 5.76\times10^{-9}$ mol/cm^2 at neutral pH. We observed the characteristic SERS peaks of 4-NBT: the C–S stretching mode, at 724 cm^{-1}, the C–H ring wagging at 857 cm^{-1}, the in-plane C–H ring bending modes at 1082 and 1112 cm^{-1}, the NO_2 symmetric stretching at 1345 cm^{-1} and the C–H stretching mode at 1575 cm^{-1}. The presence of the intense peak at 1345 cm^{-1} indicates that

the nitro group was not affected upon sorption of 4-NBT onto the Au surface. SERS peaks of 4-NBT at acid and neutral pH appear nearly at the same position suggesting that the thiol group chemisorbs strongly onto the Au surface either if it was protonated or partially deprotonated. Figures 26 and 28 show the Raman spectra of 4-NBT on smooth Au films and stainless steel at acid pH (a) and neutral pH (b), respectively; together with the normal Raman spectrum of 4-NBT (c). The SERS spectra of 4-NBT at both pH values are in good agreement with the normal Raman spectra of 4-NBT (see detail in Table 6).

ν (cm^{-1})					
SERS					
p-Si/SiO_2/Au		Stainless steel		Raman neat	Assignment
acid	neutral	acid	neutral		
725 m	725 m	724 m	724 m	724 m	C–S stretching
857 m	857 m	857 m	857 m	856 m	C–H wagging
1082 s	1083 s	1081 s	1080 s	1080 s	C–H bending
1113 m	1113 m	1112 m	1112 m	1110 m	C–H bending
1345 vs	1342 vs	1347 vs	1345 vs	1340 vs	NO_2 symmetric stretch
1575 s	1575 s	1574 s	1574 s	1572 s	C=C stretching

Table 6: Raman vibrational modes of 4-NBT in the bulk and SERS of 4NBT with Au/TiO_2 20% Au wt/wt nanoparticles on microscopically smooth Au films on p-Si/SiO_2 wafers and stainless steel Type 316 at acid and neutral pH.

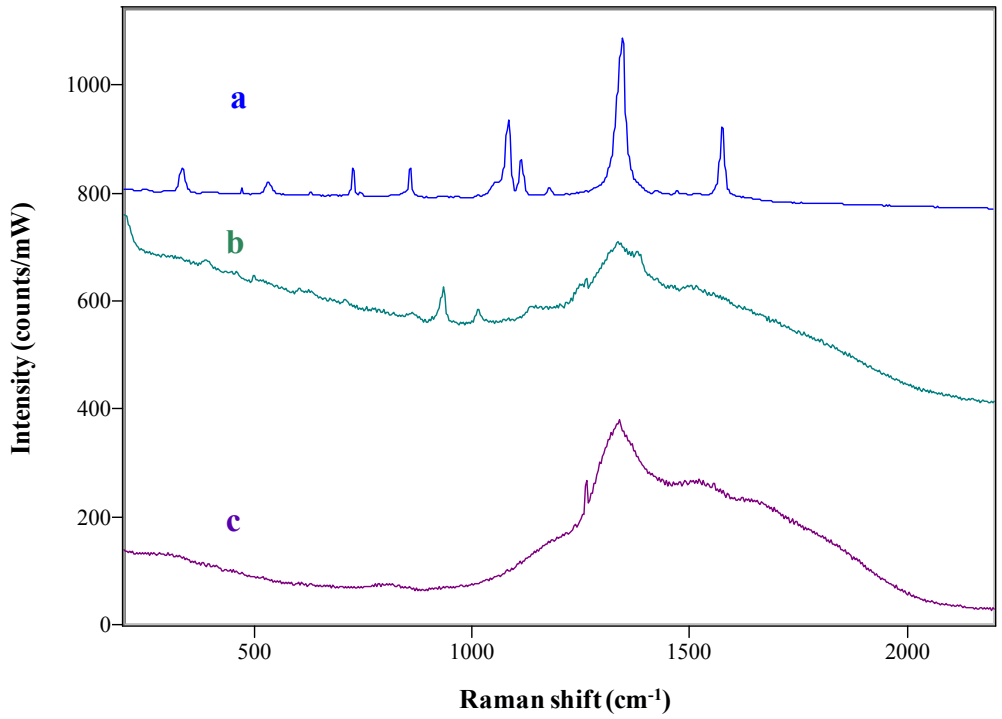

Figure 25: Raman spectra on microscopically smooth Au films on p-Si/SiO_2 wafers: a) 4-NBT ~5.76 × 10^{-9} mol/cm^2 (neutral pH) with Au/TiO_2 20% Au wt/wt; b) Au/TiO_2 20% Au wt/wt; c) 4-NBT ~ 5.76 × 10^{-9} mol/cm^2 (neutral pH). Data normalized to laser power.

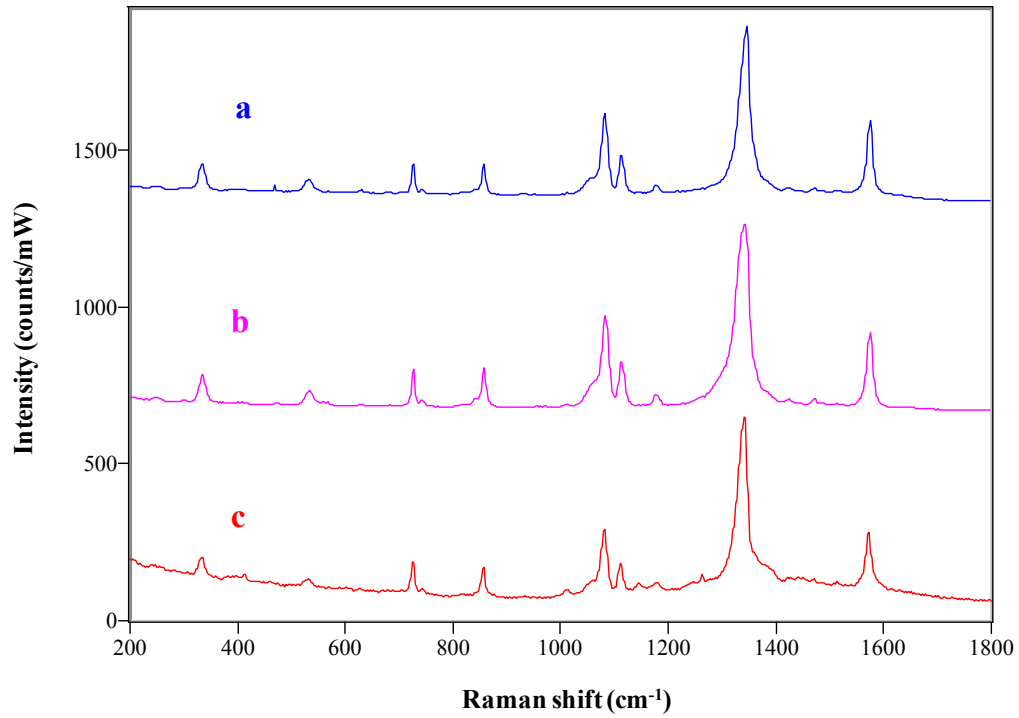

Figure 26: Raman spectra of 4-NBT ~5.76 × 10^{-9} mol/cm^2 with Au/TiO_2 20% Au wt/wt on microscopically smooth Au films on p-Si/SiO_2 wafers: a) acid pH, b) neutral pH; c) normal Raman spectra of neat 4-NBT. Data normalized to laser power.

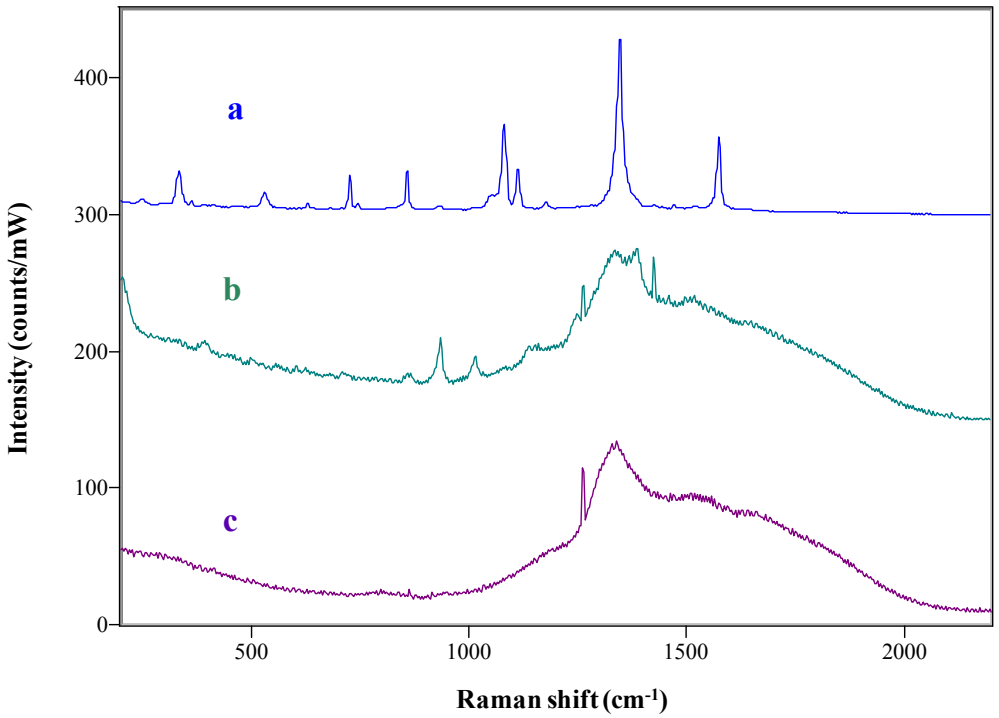

Figure 27: Raman spectra on stainless steel Type 316: a) 4-NBT ~5.76 × 10^{-9} mol/cm^2 (neutral pH) with Au/TiO_2 20% Au wt/wt; b) Au/TiO_2 20% Au wt/wt; c) 4-NBT ~ 5.76 × 10^{-9} mol/cm^2 (neutral pH). Data normalized to laser power.

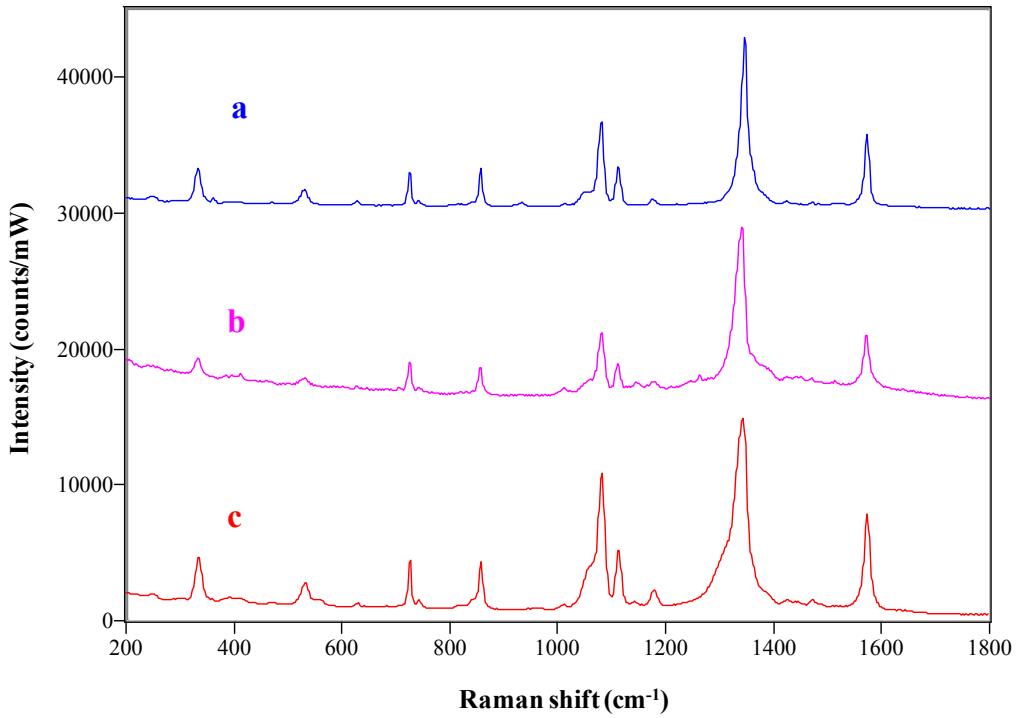

Figure 28: Raman spectra of 4-NBT ~5.76 × 10^{-9} mol/cm^2 with Au/TiO_2 20% Au wt/wt on stainless steel Type 316: a) acid pH, b) neutral pH; c) normal Raman spectra of neat 4-NBT. Data normalized to laser power.

Cautiously we turned again to the TNT experiments whishing that finally the enhancement of the Raman signals could be observed at the higher Au loading. To our surprise when TNT was self assembled with Au/TiO_2 20% Au wt/wt colloidal nanoparticles both onto our smooth Au films on the p-Si/SiO_2 wafers and the austenitic stainless steel, the long sought enhancement of the Raman signals was observed for the first time. The SERS spectra of TNT at acid pH obtained with Au/TiO_2 20% Au wt/wt on the Au films and on the austenitic stainless steel are shown in Figures 29 and 31, respectively. In both Figures we show from top to bottom the Raman spectra of (a) TNT ~5.76×10^{-9} mol/cm^2 at neutral pH with Au/TiO_2 20% Au wt/wt, (b) Au/TiO_2 20% Au wt/wt, (c) TNT ~5.76×10^{-9} mol/cm^2 at neutral pH. The SERS peaks at 714 and 857 cm^{-1} arise from the 2,6-NO_2 and 2,4,6-NO_2 scissoring, respectively. Peaks at 931 and 1010 cm^{-1} are attributed to the C-H ring bending out of plane. The peak at 1132 cm^{-1} comes from the C–H ring bending in plane, and the peak at 1212 cm^{-1} from the ring breathing. The 4-NO_2 and 2,4,6-NO_2 symmetric stretch vibration were observed at 1340 and 1393 cm^{-1}, respectively. Peaks at 1497 and 1585 cm^{-1} are due to the 4-NO_2 and 2,4,6-NO_2 asymmetric stretch vibration, respectively.

Figures 30 and 32 show the SERS spectrum of TNT obtained on smooth Au films and stainless steel at acid pH (a) and neutral pH (b), respectively; together with the normal Raman spectrum of TNT (c). Differences in the SERS peaks intensities were observed with the change in pH values. The intensity of the peaks at 714, 869 and 1132 cm^{-1} decreased when the pH was adjusted to 7. This suggests that orientation of TNT near the Au surface was affected. Comparing the normal Raman spectra of TNT to the observed SERS spectra, we noticed that some peaks were considerably shifted (see detail in Table 7). Shifts of the Raman peaks indicate that the molecular orientation was affected because of the interaction between the TNT and the metal-

semiconductor surface. In addition, we observed differences in intensity in some peaks of the SERS spectra compared to the normal Raman spectrum. SERS peaks at 869, 1497 and 1585 cm^{-1}, which involves vibrations of the nitro groups, where less intense than in the normal Raman. This indicates that TNT may be interacting with the metal-semiconductor surface through the nitro groups. The vibration modes due to the benzene ring at 931, 1010, and 1242 cm^{-1} were more intense in the SERS spectra than in the normal Raman suggesting that the benzene ring of TNT was near the metal-semiconductor surface.

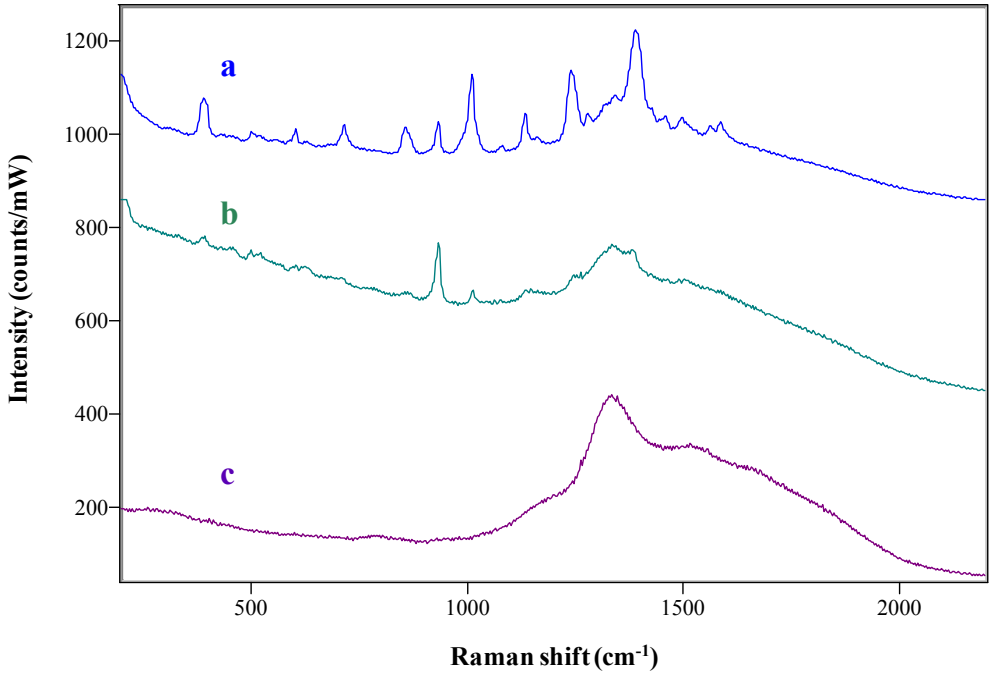

Figure 29: Raman spectra on microscopically smooth Au films on p-Si/SiO_2 wafers: a) TNT ~5.76 × 10^{-9} mol/cm^2 (acid pH) with Au/TiO_2 20% Au wt/wt; b) Au/TiO_2 20% Au wt/wt; c) TNT ~ 5.76 × 10^{-9} mol/cm^2 (acid pH). Data normalized to laser power.

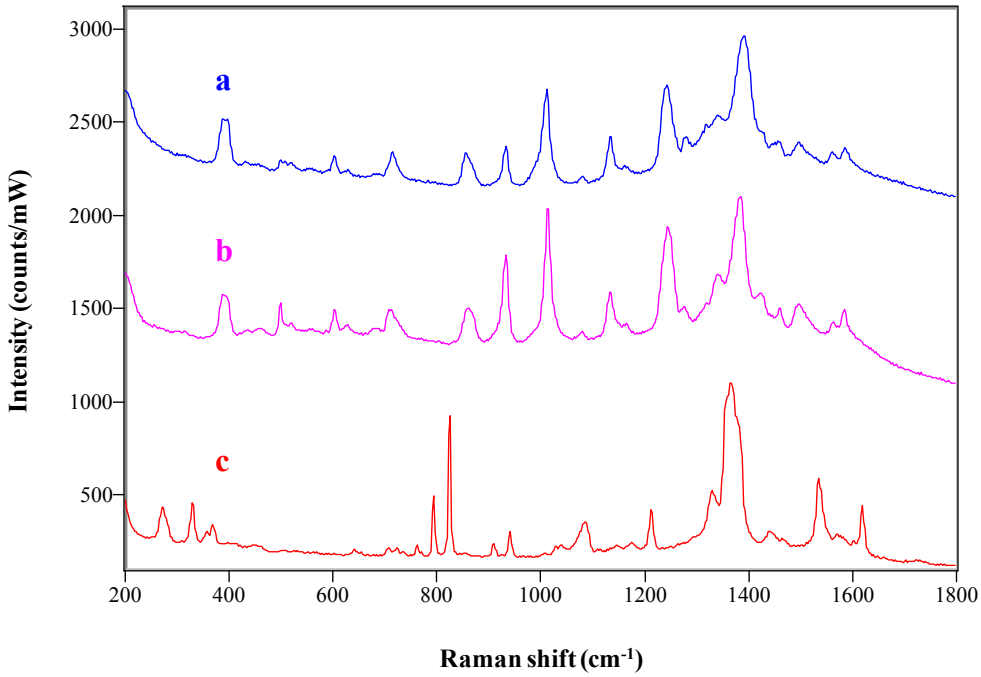

Figure 30: Raman spectra of TNT ~5.76 × 10^{-9} mol/cm^2 with Au/TiO_2 20% Au wt/wt on microscopically smooth Au films on p-Si/SiO_2 wafers: a) acid pH, b) neutral pH; c) normal Raman spectra of neat TNT. Data normalized to laser power.

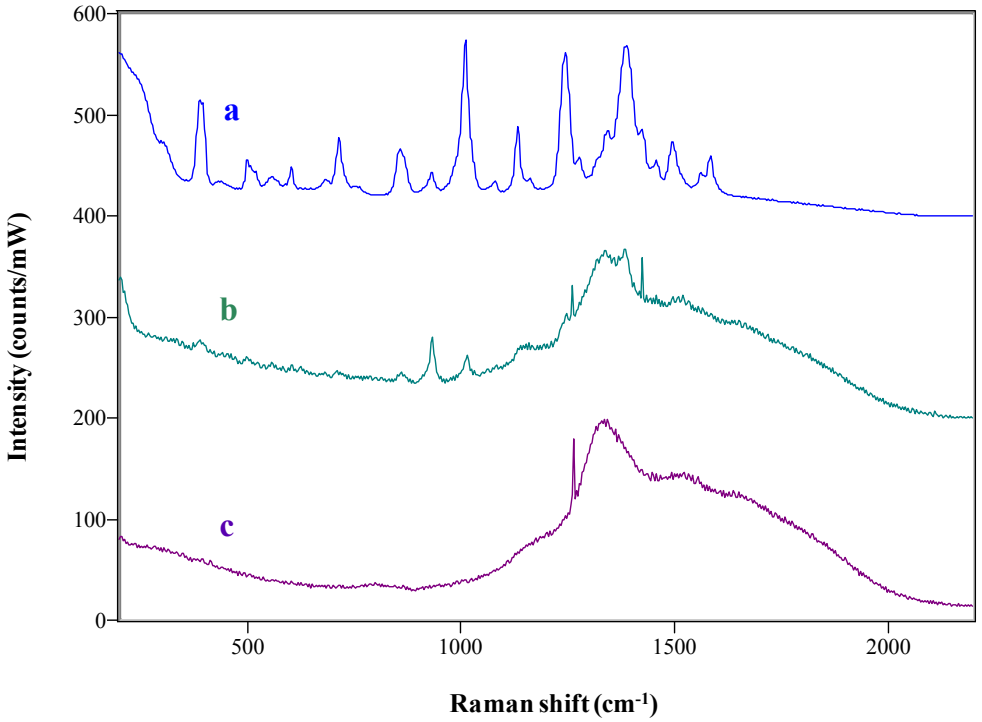

Figure 31: Raman spectra on stainless steel Type 316: a) TNT ~5.76 × 10^{-9} mol/cm^2 (acid pH) with Au/TiO_2 20% Au wt/wt; b) Au/TiO_2 20% Au wt/wt; c) TNT ~ 5.76 × 10^{-9} mol/cm^2 (acid pH). Data normalized to laser power.

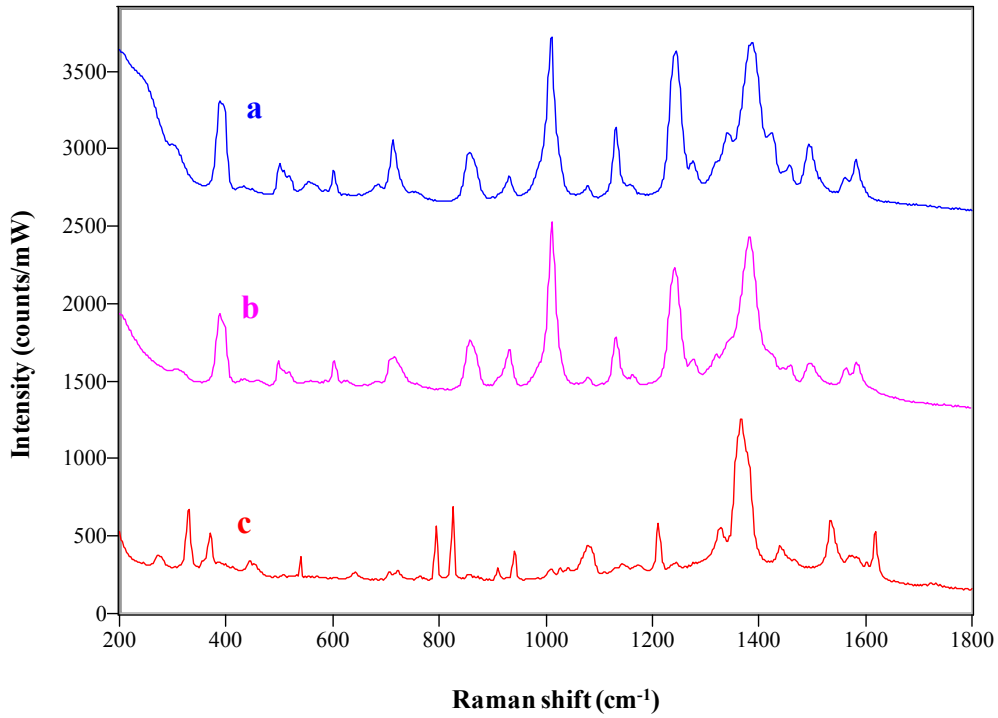

Figure 32: Raman spectra of TNT ~5.76 × 10^{-9} mol/cm^2 with Au/TiO_2 20% Au wt/wt on stainless steel Type 316: a) acid pH, b) neutral pH; c) normal Raman spectra of neat TNT. Data normalized to laser power.

ν (cm^{-1})					
SERS					
p-Si/SiO_2/Au		Stainless steel		Raman	Assignment
acid	neutral	acid	neutral	neat	
714 m	717 w	713 m	714 w	724 w	2,6-NO_2 scissoring
857 m	860 w	859 m	860 w	824 s	2,4,6-NO_2 scissoring
932 m	932 m	931 m	931 m	909 w	C–H bending (ring) out of plane
1009 vs	1011 vs	1010 vs	1011 vs	941 m	C–H bending (ring) out of plane
1133 m	1132 w	1132 m	1132 w	1084 m	C–H bending (ring) in plane
1243 vs	1242 vs	1243 vs	1242 vs	1212 s	ring breathing
1341 sh	1343 sh	1340 sh	1342 sh	1329 sh	4-NO_2 symmetric stretching
1393 vs	1385 vs	1386 vs	1382 vs	1367 vs	2,4,6-NO_2 symmetric stretching
1497 w	1498 w	1496 w	1498 w	1536 s	4-NO_2 asymmetric stretching
1585 w	1585 w	1583 w	1585 w	1620 s	2,4,6-NO_2 asymmetric stretching

Table 7: Raman vibrational modes of TNT in the bulk and SERS of TNT with Au/TiO_2 20% Au wt/wt nanoparticles on microscopically smooth Au films on p-Si/SiO_2 wafers and stainless steel Type 316 at acid and neutral pH.

5.9 Raman Experiments with 54% wt/wt Ag/TiO_2 Self Assembled Nanoparticles

The stability of the colloidal Ag/TiO_2 nanoparticles (54% Ag wt/wt) was an impairing issue; but nevertheless we performed Raman studies in the search of SERS with both 4-NBT and TNT. The Raman spectra of 4-NBT at acid and neutral pH were recorded with 54% wt/wt Ag loading TiO_2 particles assembled the smooth Au and austenitic stainless steel substrates, as show in Figures 34 and 36, respectively. In Figures 33 and 35 we show from top to bottom the Raman spectra of (a) 4-NBT ~5.76×10^{-9} mol/cm^2 at acid pH with Ag/TiO_2 54% Ag wt/wt, (b) Ag/TiO_2 54% Ag wt/wt, and (c) 4-NBT ~5.76×10^{-9} mol/cm^2 at acid pH. The characteristics peaks of 4-NBT were observed: C-S stretch vibration at 724 cm^{-1}, C–H ring wagging at 857 cm^{-1}, in-plane C–H ring bending at 1082 and 1112 cm^{-1}, NO_2 symmetric stretching at 1345 cm^{-1} and the C–H ring stretch vibration at 1575 cm^{-1}. The presence of the prominent peak at 1345 cm^{-1} indicate that sorption of 4-NBT onto Ag surface did not affect the nitro group. SERS peaks of 4-NBT at both pH values appear nearly at the same position, suggesting that the thiol group also adsorbs strongly onto the metal-semiconductor surface at either pH. Figures 34 and 36 show the SERS spectrum of 4-NBT obtained on smooth Au films and stainless steel at acid pH (a) and neutral pH (b), respectively; together with the normal Raman spectrum of 4-NBT (c). The SERS spectra of 4-NBT at both pH values were consistent with the 4-NBT normal Raman spectra (see details in Table 8).

Unfortunately, however, TNT was again a frustrating failure with this colloid. In spite of our best efforts, no Raman enhancement was observed for TNT when self assembled with colloidal Ag/TiO_2 nanoparticles. The procedure used was the same as previously described by deposition of an analyte-colloid mix onto our smooth Au films on p-Si/SiO_2 wafers and onto the austenitic stainless steel.

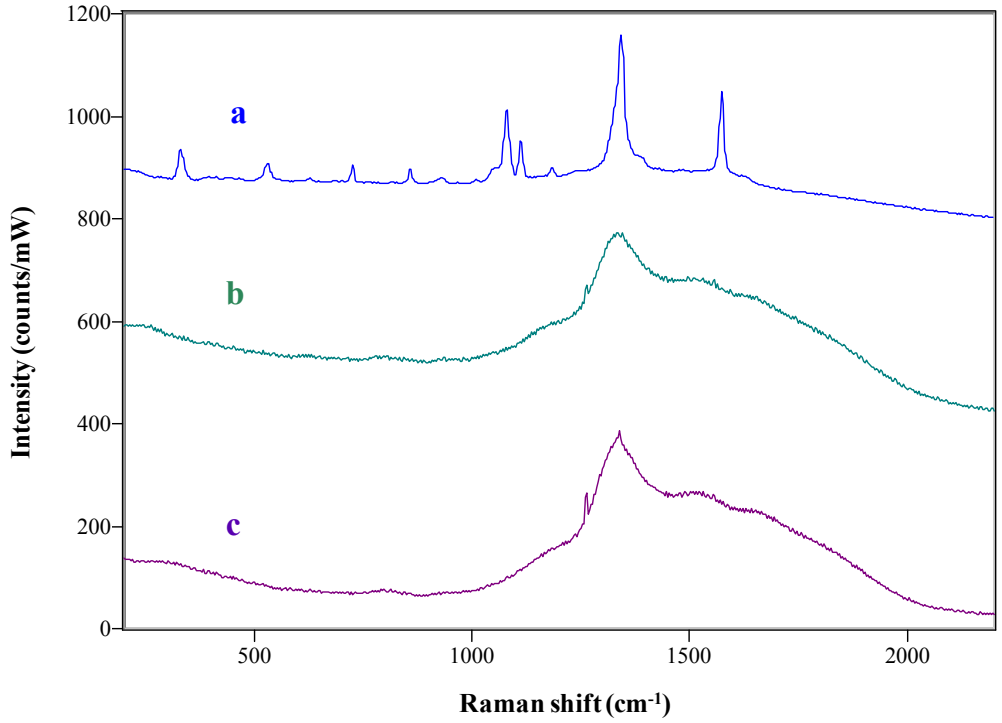

Figure 33: Raman spectra on microscopically smooth Au films on p-Si/SiO_2 wafers: a) 4-NBT ~5.76 × 10^{-9} mol/cm^2 (neutral pH) with Ag/TiO_2 54% Ag wt/wt; b) Ag/TiO_2 54% Ag wt/wt; c) 4-NBT ~ 5.76 × 10^{-9} mol/cm^2 (neutral pH). Data normalized to laser power

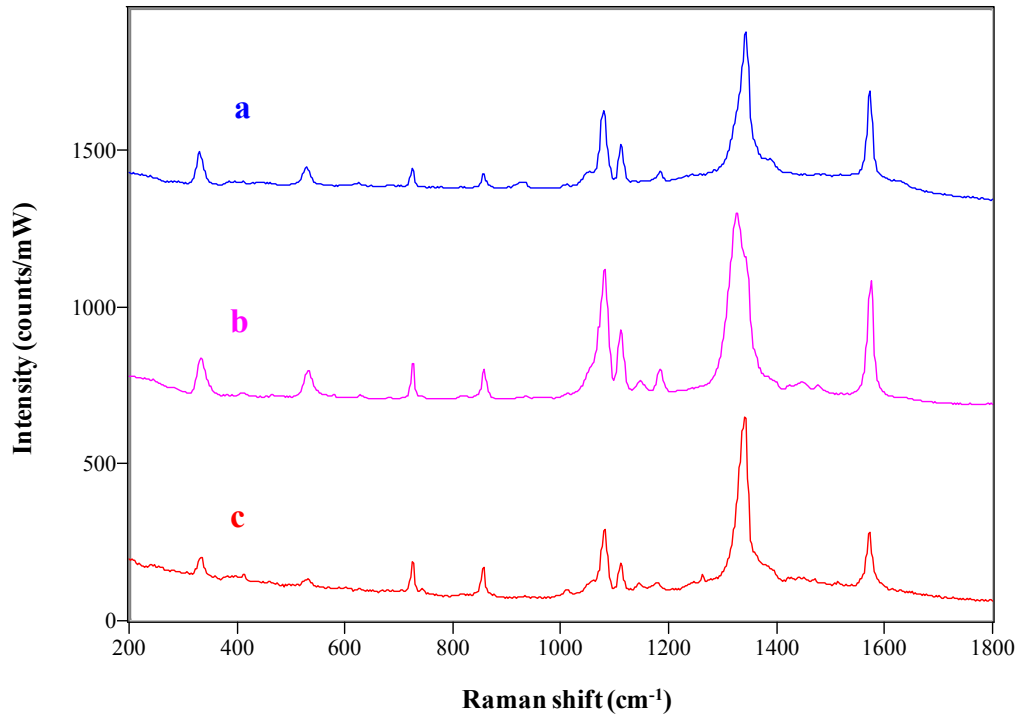

Figure 34: Raman spectra of 4-NBT ~5.76 × 10^{-9} mol/cm^2 with Ag/TiO_2 54% Ag wt/wt on microscopically smooth Au films on p-Si/SiO_2 wafers: a) acid pH, b) neutral pH; c) normal Raman spectra of neat 4-NBT. Data normalized to laser power.

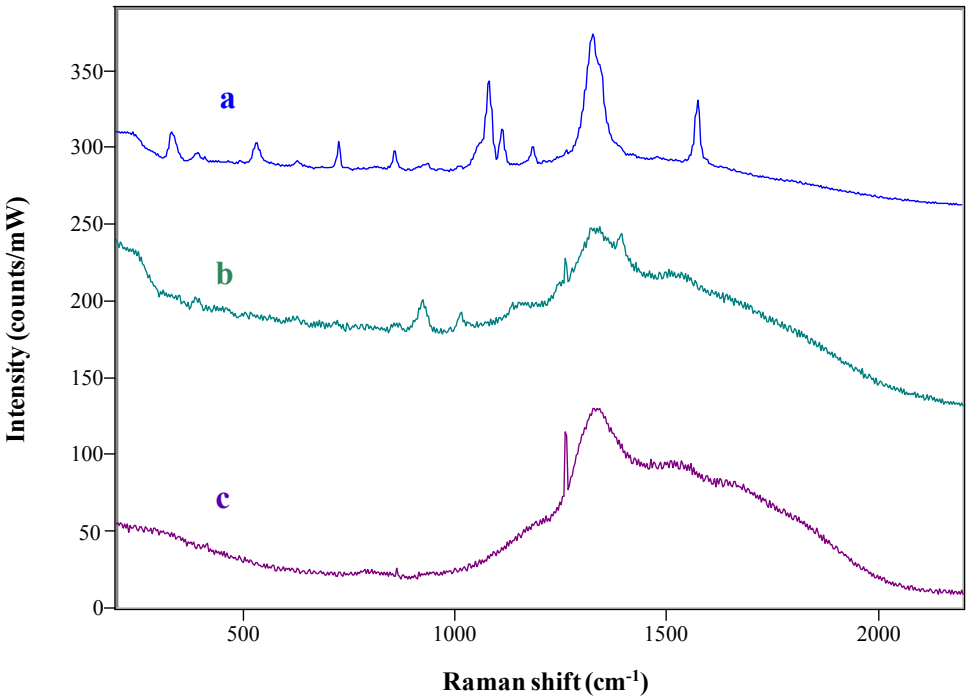

Figure 35: Raman spectra on stainless steel Type 316: a) 4-NBT ~5.76 × 10^{-9} mol/cm^2 (neutral pH) with Ag/TiO_2 54% Ag wt/wt; b) Ag/TiO_2 54% Ag wt/wt; c) 4-NBT ~ 5.76 × 10^{-9} mol/cm^2 (neutral pH). Data normalized to laser power.

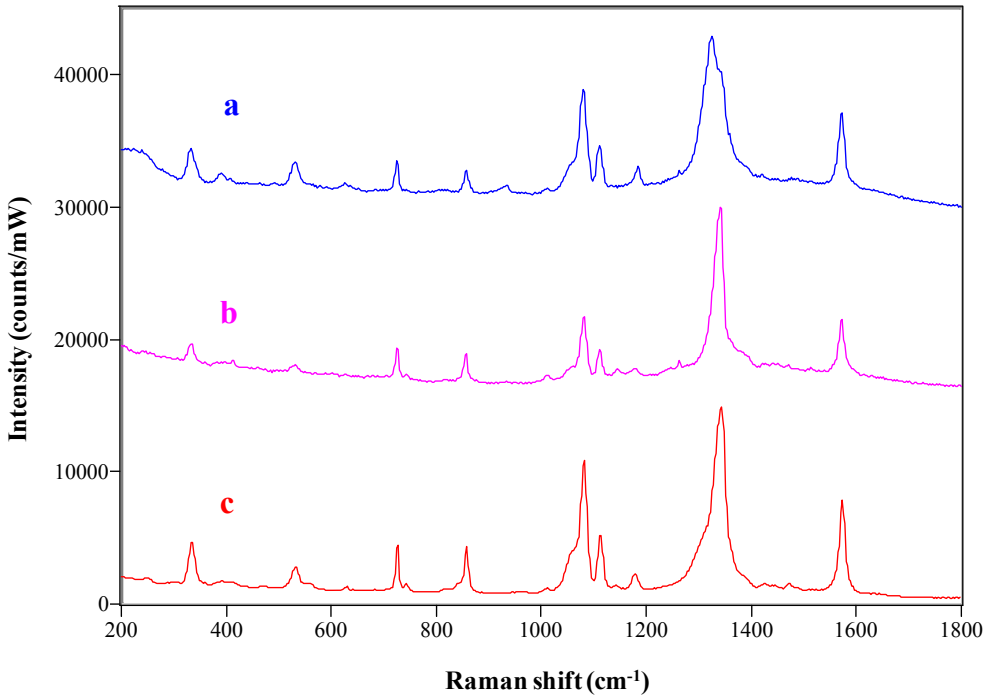

Figure 36: Raman spectra of 4-NBT ~5.76 × 10^{-9} mol/cm^2 with Ag/TiO_2 54% Ag wt/wt on stainless steel Type 316: a) acid pH, b) neutral pH; c) normal Raman spectra of neat 4-NBT. Data normalized to laser power.

ν (cm^{-1})					
SERS					
p-$SiSiO_2$/Au		Stainless steel		Raman	Assignment
acid	neutral	acid	neutral	neat	
725 m	725 m	725 m	725 m	724 m	C–S stretching
857 m	857 m	858 m	858 m	856 m	C–H wagging
1082 s	1081 s	1085 s	1084 s	1080 s	C–H bending
1113 m	1110 m	1110 m	1111 m	1110 m	C–H bending
1330 vs	1326 vs	1325 vs	1325 vs	1340 vs	NO_2 symmetric stretch
1575 s	1575 s	1574 s	1575 s	1572 s	C=C stretching

Table 8: Raman vibrational modes of 4-NBT in the bulk and SERS of 4NBT with Ag/TiO_2 54% Ag wt/wt nanoparticles on microscopically smooth Au films on p-Si/SiO_2 wafers and stainless steel Type 316 at acid and neutral pH.

The failure to observe Raman enhancement with TNT was due presumably to the laser line of 785-nm used to induce the required electron oscillations. The literature shows, as mentioned earlier, that Raman enhancement is observed when the frequency of the incident light is in resonance with the metal surface plasmons and for colloidal Au nanoparticles, the resonance is attained with a 785-nm laser line whereas for colloidal Ag nanoparticles with a 514/532-nm laser line is needed. Raman enhancement of 4-NBT with colloidal TiO_2 loaded with 54% Ag wt /wt was observed using the 785-nm laser line because 4-NBT strongly chemisorbs onto the metal-semiconductor surface forming a charge transfer complex which resonates with the laser line used. Since the TNT molecules are not sorbed strongly on the metal-semiconductor surface, no charge transfer complex can result and hence the laser line used would not be able to make the Ag surface plasmon resonate. Further studies with different laser lines were not pursued with colloidal Ag/TiO_2 nanoparticles due to the poor stability of the colloid.

5.9.1 Conclusion

In conclusion of this part, successful Raman enhancement were achieved with the prepared metal-semiconductor nanoparticles when self assembled onto microscopically smooth Au films on the p-Si/SiO_2 wafers not only due to the localized plasmons generated on the metal surface, but due to the simultaneous induction of a delocalized plasmon or polariton within the underlying smooth Au surface. It was anticipated that excitation of the polariton on the semiconductor-metal junctions would generate an intense local field. Coupling of both plasmon resonances produces the observed Raman enhancements. It is intriguing that comparable enhancements of the Raman signals can be observed with austenitic stainless steel (Type 316, Cr-Ni-Mo) suggesting that the minor components added to increase the steel stability act as surface states capable to induce the generation of delocalized surface plasmons (polaritons).

These observations strongly suggested that we were in the presence of an effect more general than it had been anticipated. In view of the successful Raman enhancements achieved with the combination of metal-semiconductor nanoparticles self assembled over microscopically smooth Au films with an underlying p-Si/SiO_2 structure, we decided to explore the possibility of preparing SERS active substrates by chemical etching of the very same microscopically smooth Au films. The rationale for this approach was that ordered arrays of Au "hot spots" could be generated on smooth Au/p-Si/SiO_2 wafers when etched with *aqua regia* under finely controlled reaction conditions. We had made the observation that etched materials when analyzed by electron microscopy showed etched galleries with a nanoscopic grain structure that ought to be suitable as SERS active hot spots. Raman enhancements as strong as those observed in the self assembly experiments were anticipated. In this case, the underlying substrate would have to serve to generate both the delocalized surface plasmon (polariton) and the localized surface plasmon on the metal nanograins.

CHAPTER 6

6 SERS ACTIVE GOLD SUBSTRATES BY CHEMICAL ETCHING

The rationale behind this part of the work has been delineated above and emanates from the proposed SERS mechanism for noble metal loaded semiconductor particles self assembled on continuously smooth metal surfaces. In summary, in the case of the silicon wafers, the rationale is that 1) these wafers contain a semiconductor-metal junction on a Si based substrate, 2) the laser can induce at the semiconductor-metal junction a delocalized plasmon or polariton which induces a highly enhanced local field, and 3) when the polariton couples with the localized surface plasmons induced at the of metal-semiconductor junctions on the TiO_2 nanoparticles, they induce a enhanced emission of light with the Raman shift of the analyte. It seemed to us that it was worthwhile to explore the possibility of preparing SERS active substrates by chemical etching of microscopically smooth Au films.

We anticipated that the underlying substrate would serve to generate both the delocalized surface plasmon (polariton) and the localized surface plasmon on the metal nanograins present in the galleries that usually form by chemical etching in microscopically smooth Au films. We wish to report that ordered arrays of SERS-active hot spots can be formed on well-defined metal-semiconductor layers by chemical etching of smooth Au films prepared by conventional vapor phase deposition on p-Si/SiO_2 wafers using standard techniques. Our results show that highly localized plasmon excitations can be created in disordered metallic nanostructures. These simple and effective SERS active systems have a practical advantage in that the “hot spots” can be readily generated by controlled chemical etching with *aqua regia* and are easily visualized by Raman spectroscopy.

6.1 Controlled Etching of Smooth Au Films on p-Si/SiO_2 Wafers

The Au films used in this part of research are the same microscopically smooth mirrors described above. The films were prepared by physical vapor deposition using standard techniques. Even though the wafers were prepared to order at Neûchatel, they were characterized locally to confirm their thickness and composition. This was done by standard SEM finding that as ordered, the thickness of p-Si was 222 μm, the thickness of SiO_2 was 171 μm and, most importantly, the Au film was 8.4 μm (Figure 37). The smoothness of the Au was confirmed by optical microscopy with a 100x magnification (Figure 38), AFM (Figure 39), and SEM (Figure 40a). It was anticipated that for successful gallery creation the Au surface had to be smooth at the micron size level.

Following the characterization described above, we proceeded with the chemical etching experiments. This required careful control of the strength, age and time of action of reagent grade *aqua regia* on the microscopically smooth Au surfaces. Initial deepings of the Au wafers in concentrated H_2SO_4 and HNO_3 acids failed to produce SERS. A stronger but brief treatment with *aqua regia* was chosen as an alternative. *Aqua regia* was formed mixing concentrated nitric and hydrochloric acids, each acid carrying out a different task. Nitric acid is a powerful oxidizer, it dissolve gold producing gold ions (Au^{3+}). In turn, the chloride ions (Cl^-) from the hydrochloric acid form coordination complexes with Au^{3+} producing chloroaurate ions ($AuCl_4^-$). The dissolved gold in solution becomes chloroauric acid ($HAuCl_4$) which is suitable for photochemical deposition experiments. Several trials were performed in turn until Raman enhancement was observed. The successful conditions were when the microscopically smooth Au wafers were immersed in full strength *aqua regia* for 5 s and then washed with ultra pure water (18 MΩ.cm). This step was done two times.

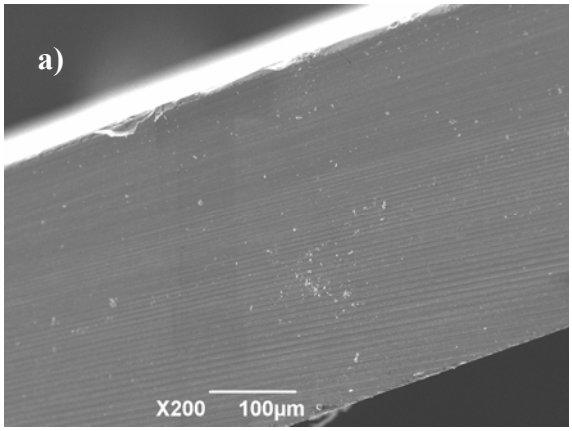

Measurement	*length (µm)*	*Error*
1	391.5	2.0
2	395.3	1.8
3	395.8	2.3
4	394.5	1.0
5	390.0	3.5
6	393.8	0.3
Average	393 ± 2	2

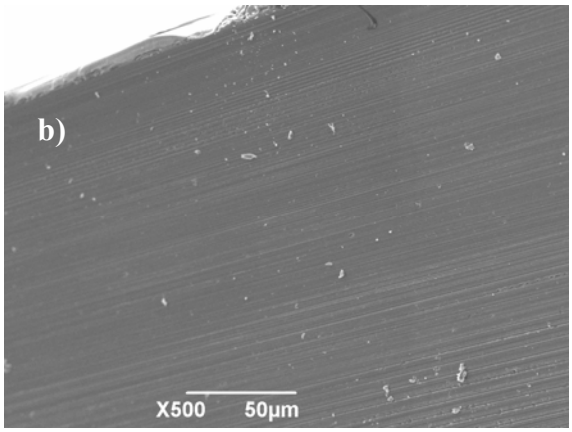

Measurement	*length (µm)*	*Error*
1	169.9	1.0
2	173.5	2.6
3	167.8	3.2
4	174.2	3.3
5	173.3	2.4
6	166.7	4.2
Average	171 ± 3	3

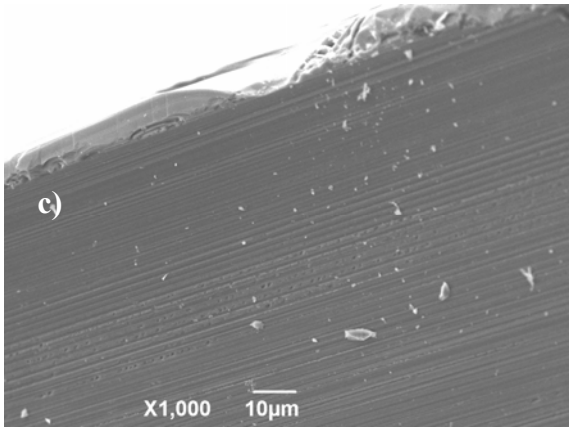

Measurement	*length (µm)*	*Error*
1	8.13	0.25
2	8.13	0.24
3	7.97	0.40
4	7.97	0.40
5	8.76	0.38
6	9.36	0.99
7	8.79	0.42
8	7.88	0.50
Average	8.4 ± 0.4	0.4

Figure 37: SEM image Au films on p-Si/SiO_2 wafers: a) total composite thickness, b) SiO_2 thickness, c) Au film thickness.

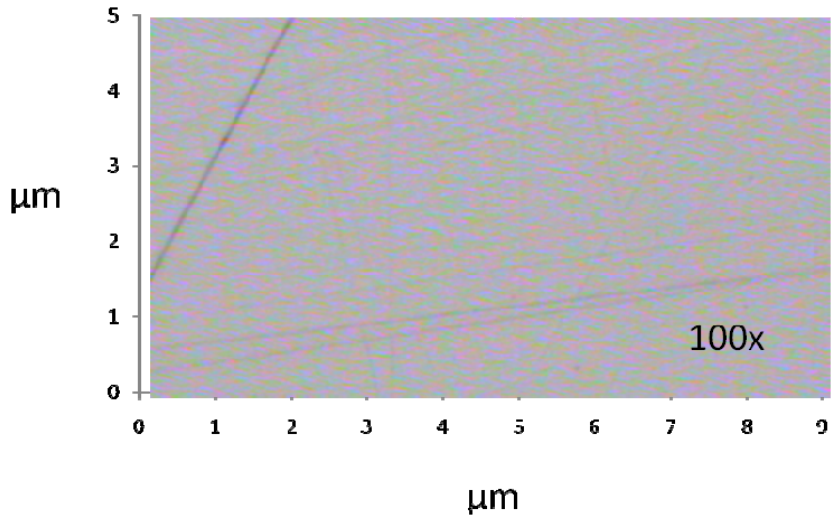

Figure 38: Optical microscope image of microscopically smooth Au films on p-Si/SiO_2 wafers.

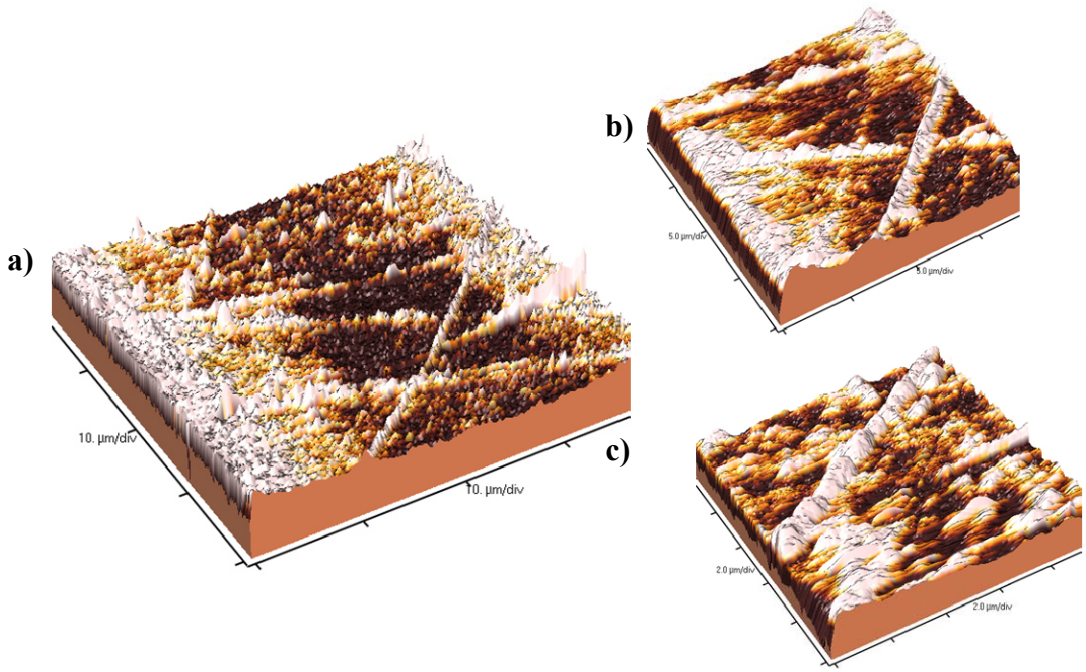

Figure 39: AFM images of microscopically smooth Au films on p-Si/SiO_2 wafers: a) 40×40 μm^2; b) 20×20 μm^2 and c) 10×10 μm^2 scan sizes.

The gold surface roughness of the chemically etched Au films were corroborated by SEM. Figures 40a and 40b show the SEM image (magnification 20,000 x) of the Au film on the p-Si/SiO_2 wafers before and after the chemical etching treatment with *aqua regia*. The etched Au films exhibited a typical aspect of a rough surface, with nanostructures of an average diameter of 195 ± 3 nm. Gold surface morphology was characterized by AFM. Scan windows of 20 × 20, 16 × 16 and 8 × 8 μm^2 were performed to a 100×100 μm^2 area through the etched Au surface. Figure 41 shows the AFM image of etched Au films on p-Si/SiO_2 wafers at the three scan sizes measured. By the naked eye we can establish that surface roughness was achieved. A detailed study was done considering two parameters: the root mean square (Rms) and the arithmetic average height (Ra). Rms is the standard deviation of the height values within a given area. Ra, the most frequently used roughness parameter, is the average deviation of the roughness irregularities from the mean line over one sampling length. Homogeneity of surface roughness through the substrate was studied comparing the Ra values obtained. Rms and Ra values obtained are typical of roughened metal surfaces. Table 9 shows the Rms and Ra values of the etched Au films obtained at different spot areas.

scan size (μm^2)	*Rms*	*Ra*
20 × 20	13.9 ± 1.7	11 ± 1.5
16 × 16	11.8 ± 1.4	9.4 ± 1.2
8 × 8	10.5 ± 1.6	8.2 ± 1.1

Table 9: Surface Roughness values express as the root mean square height (Rms) and the arithmetic average height (Ra) of etched Au films obtained with scans windows of 20 × 20, 16 × 16 and 8 × 8 μm^2.

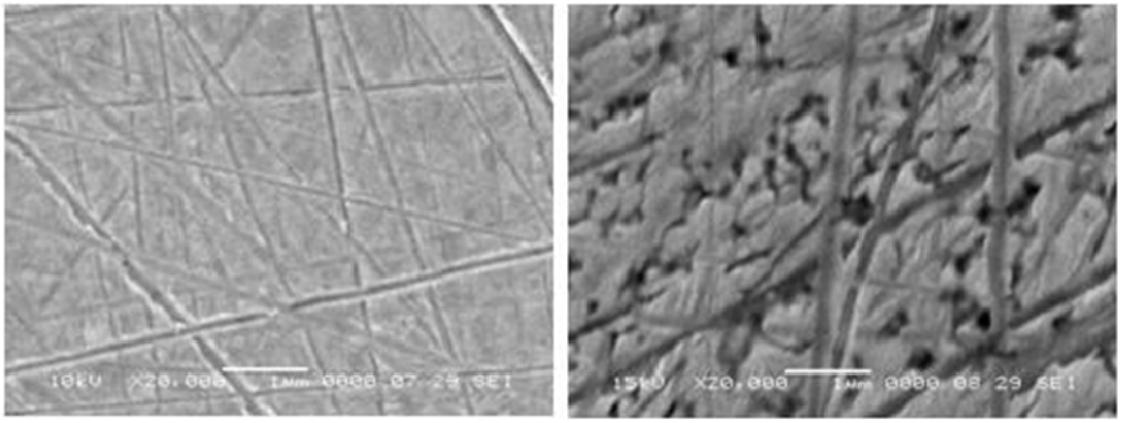

Figure 40: SEM image of Au films on p-Si/SiO_2 wafers: a) microscopically smooth; b) etched.

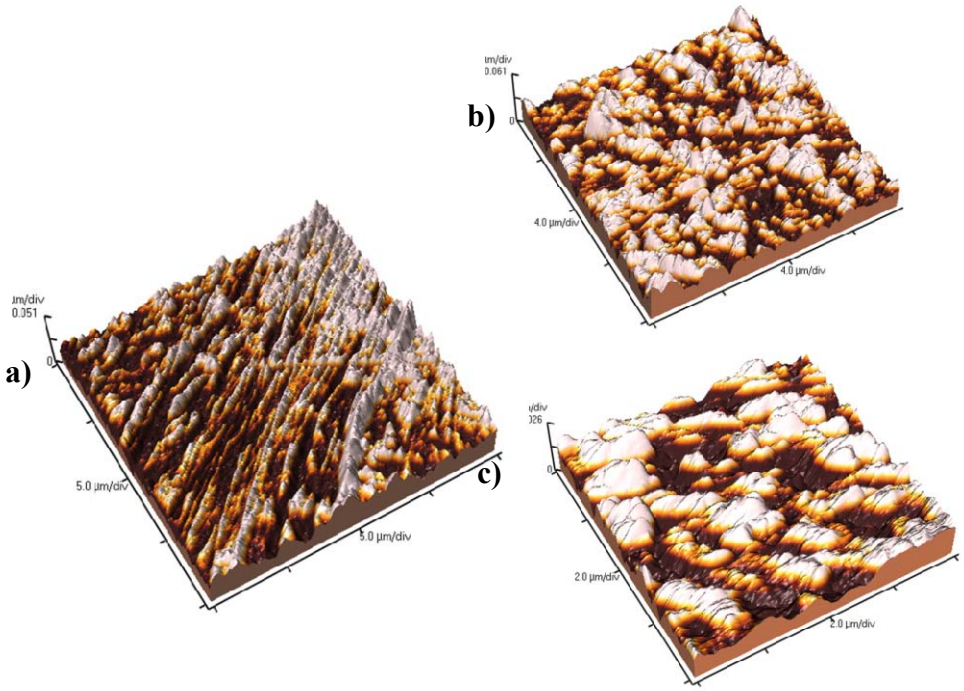

Figure 41: AFM images of etched Au films on p-Si/SiO_2 wafers: a) 20×20 μm^2; b) 16×16 μm^2 and c) 10×10 μm^2 scan sizes.

6.2 Raman Studies with Etched Au Films on p-Si/SiO_2 Wafers

SERS studies of etched Au films on p-Si/SiO_2 wafers were performed with 4-ABT (4-aminobenzenethiol) and 4-NBT in ethanol solutions of concentrations ranging from 10^{-4}-10^{-7}M. Ethanol was used as a solvent in these experiments due to its high volatility. Ethanol quickly evaporates, leaving the dried molecules adsorbed on the surface. Also, the excellent wetting properties of ethanol make it ideal to be well dispersed across the surface, yielding a uniform distribution of dried molecules. The analyte solutions were evaporated at 40 °C in a laminar flow hood for ~ 30 min. Once the sample was dried, the Au surface was rinsed with ethanol to remove any material not strongly adsorbed to the surface. This method ensures that all soluble material is removed and at most one monolayer of the probe molecule is present on the etched gold surface. SERS studies were also performed with TNT using the same sample preparation method described above.

We anticipated that Raman enhancement would be observed for 4-NBT under these conditions and effectively it was observed for concentrations as low as 1.59×10^{-11} mol/cm^2. Figure 42 show the SERS spectrum of 4-NBT on etched Au films on p-Si/SiO_2 wafers. We show from top to bottom the Raman spectra of 4-NBT~ 1.59×10^{-11} mol/cm^2 on: (a) etched Au film on p-Si/SiO_2 wafers, and b) microscopically smooth Au films on p-Si/SiO_2 wafers. The SERS spectrum shows a prominent peak at 1334 cm^{-1} which is attributed to the NO_2 symmetric stretch vibration. Appearance of this peak suggests that the nitro group was not affected when 4-NBT was adsorbed on the Au surface. This indicates that 4-NBT is absorbed on the Au surface through the thiol group. Other strong peaks at about 1081 and 1572 cm^{-1} are assigned to the in-plane C–H ring bending and to the C–C ring stretching, respectively. Other weak peaks at 724 and 857 cm^{-1} arise from the C–S stretch vibration and C–H ring wagging, respectively. Figure 43

shows the SERS Raman spectrum of 4-NBT on the etched Au films on p-Si/SiO_2 wafers (a) and 4-NBT normal Raman spectrum (b). The SERS spectrum of 4-NBT was consistent with the normal Raman spectra of 4-NBT (see details in Table 10).

Similarly, Raman enhancement of 4-ABT was observed with etched Au films on p-Si/SiO_2 wafers at a concentration of 1.59×10^{-11} mol/cm^2. Figure 44 show the SERS spectrum of 4-ABT on etched Au film on p-Si/SiO_2 wafers. We show from top to bottom the spectra of 4-ABT at ~ 1.59×10^{-11} mol/cm^2 on: (a) etched Au film on p-Si/SiO_2 wafers, b) microscopically smooth Au films on p-Si/SiO_2 wafers. The intense peak at 1080 cm^{-1} arises from the C-S stretch vibration. Other strong peak at 1585 cm^{-1} came from the C–C ring stretch and NH_2 bend vibrations. The peak at 393 cm^{-1} came from the ring deformation and NH_2 wagging. The weak peak at 1333 cm^{-1} is assigned to ring deformation and NH_2 rocking. Appearance of peaks that arise from the characteristic vibrational modes of the amino group suggest that the amino group was not affected when 4-ABT absorb onto the gold surface. This indicates that 4-NBT was adsorbed on the Au surface through the thiol group. Figure 45 shows the SERS spectra of 4-ABT on etched Au films (a) and 4-ABT normal Raman (b). SERS spectra of 4-ABT was in a good agreement with the normal Raman of 4-ABT (see detail in Table 11).

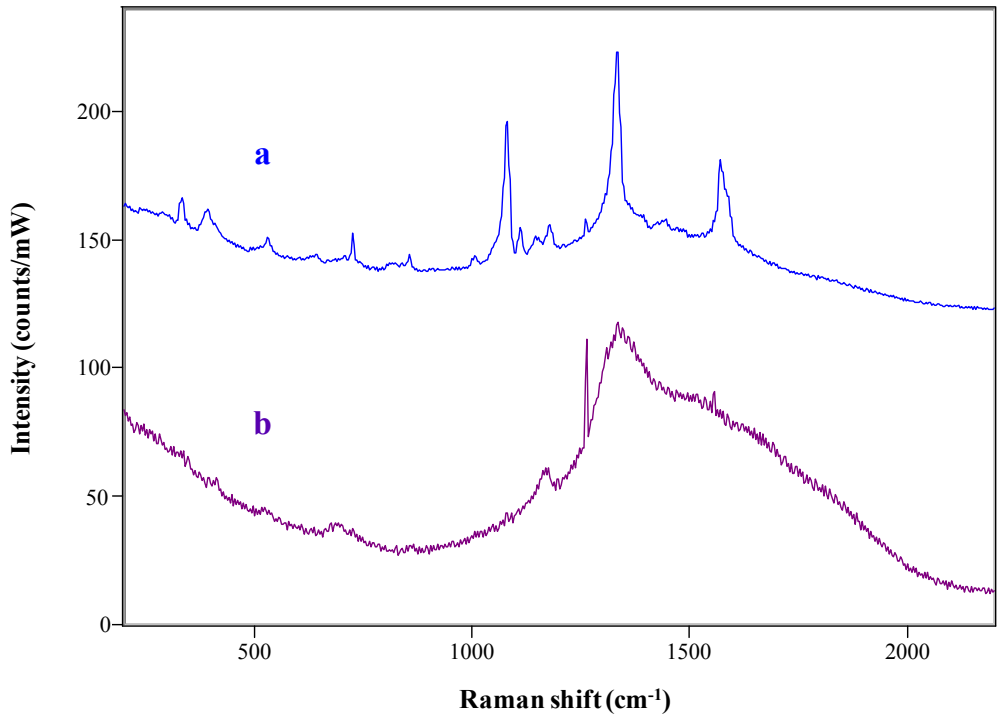

Figure 42: SERS spectrum of 4-NBT ~ 1.59×10^{-11} mol/cm^2 on: a) roughened Au film on p-Si/SiO_2 wafers, b) microscopically smooth Au films on p-Si/SiO_2 wafers. Data normalized to laser power.

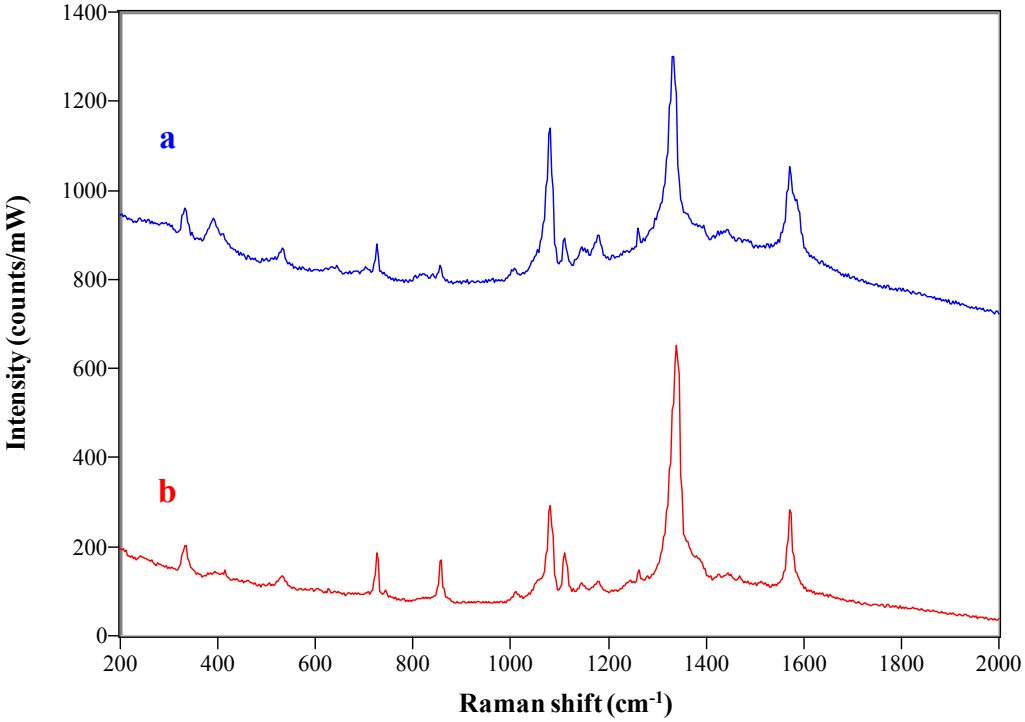

Figure 43: SERS spectrum of 4-NBT ~ 1.59×10^{-11} mol/cm^2 on: a) roughened Au film on p-Si/SiO_2 wafers, b) normal Raman neat 4-NBT. Data normalized to laser power.

ν (cm^{-1})		Assignment
SERS	Raman neat	
724 w	724 w	C–S stretching
854 w	856 w	C–H wagging
1081 s	1082 s	C–H bending (ring) in-plane
1110 w	1110 w	C–H bending (ring) in-plane
1333 vs	1340 vs	NO_2 symmetric stretching
1572 s	1572 s	C=C stretching

Table 10: Raman vibrational modes of 4-NBT in the bulk and SERS of 4-NBT with etched Au film on p-Si/SiO_2 wafers.

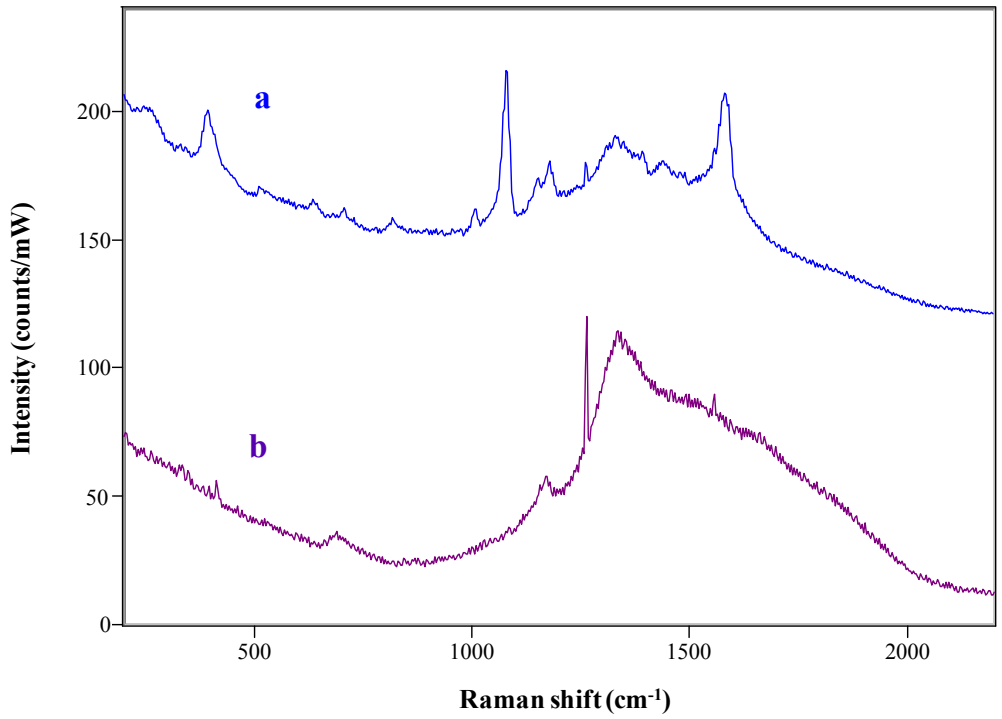

Figure 44: SERS spectrum of 4-ABT ~ 1.59×10^{-11} mol/cm^2 on: a) roughened Au film on p-Si/SiO_2 wafers, b) microscopically smooth Au films on p-Si/SiO_2 wafers. Data normalized to laser power.

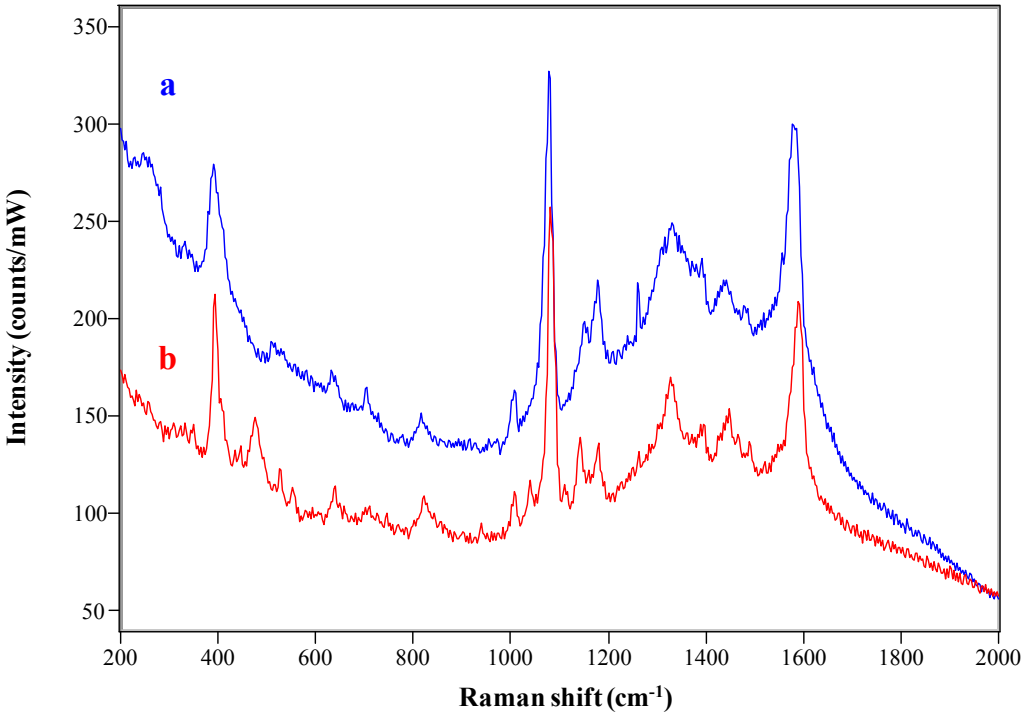

Figure 45: SERS spectrum of 4-ABT ~ 1.59×10^{-11} mol/cm^2 on: a) roughened Au film on p-Si/SiO_2 wafers, b) normal Raman neat 4-ABT. Data normalized to laser power.

ν (cm-1)		
SERS	Raman neat	Assignment
393 m	390 m	ring deformation + NH_2 wagging
1080 vs	1082 vs	C–S stretching
1333 w	1330 w	ring deformation + NH_2 rocking
1585 s	1592 s	C=C stretch + NH_2 bending

Table11: Raman vibrational modes of 4-ABT in the bulk and SERS of 4-ABT with etched Au film on p-Si/SiO_2 wafers.

We were fortunate again to observe a strong enhancement of the Raman with TNT at a concentration of 7.96×10^{-9} mol/cm^2 using the etched Au films. Figure 46 show the SERS spectrum of TNT on etched Au film on p-Si/SiO_2 wafers. We show from top to bottom the Raman spectra of TNT~ 7.96×10^{-9} mol/cm^2 on: (a) etched Au film on p-Si/SiO_2 wafers, b) microscopically smooth Au films on p-Si/SiO_2 wafers. The strong peaks at 1080, 1331 and 1570 cm^{-1} came from the in-plane C-H ring bending, 2,4,6-NO_2 symmetric stretching and 4-NO_2 asymmetric stretching. The peak at 1110 cm^{-1} is assigned to the in-plane C–C ring bend, 2,4,6-C–N and C–CH_3 stretch vibration. Other weak peaks at 723 and 854 cm^{-1} arise from the 2,6-NO_2 and 2,4,6-NO_2 scissoring, respectively.

Figure 47 shows the SERS spectra of TNT on etched Au films (a) and TNT normal Raman (b). Shifts in the position of some peaks between the TNT normal Raman and the SERS spectra were observed (see detail in Table 12). This indicates that the molecular orientation was affected because of the interaction between the TNT and the active sites on the gold surface. Presence of the strong peaks at 1331 and 1571 cm^{-1} assigned to the 4-NO_2 symmetric and asymmetric stretching indicates that the para nitro group was not affected by the TNT interaction with the active sites on the gold surface. Normal Raman peaks at 1367 and 1620 cm^{-1}, corresponding to the 2,4,6-NO_2 symmetric and asymmetric stretch vibration were not present in the SERS spectrum. This suggests that interaction between TNT and the active sites on the gold surface was through the ortho nitro groups.

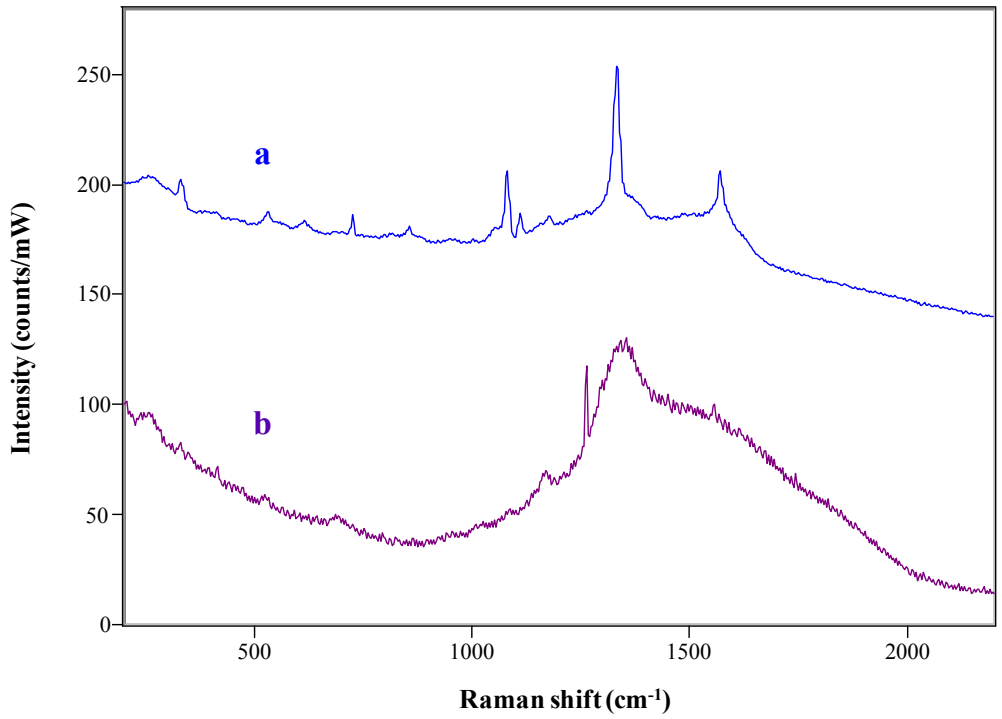

Figure 46: SERS spectrum of TNT ~ 7.96×10^{-9} mol/cm^2 on: a) roughened Au film on p-Si/SiO_2 wafers, b) microscopically smooth Au films on p-Si/SiO_2 wafers. Data normalized to laser power.

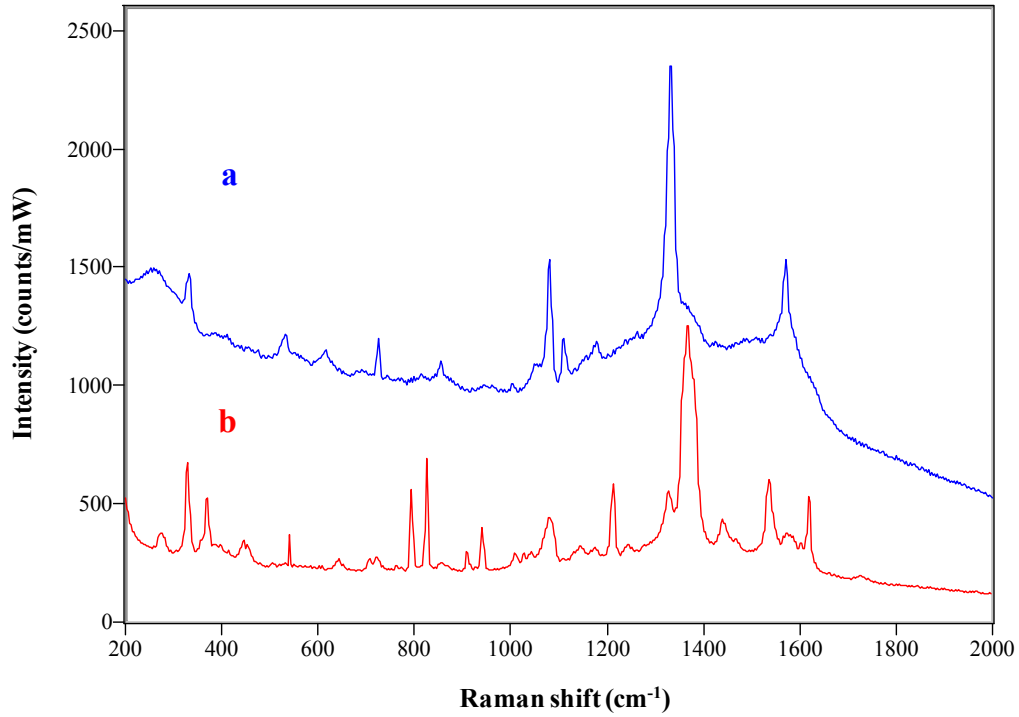

Figure 47: SERS spectrum of TNT ~ 7.96×10^{-9} mol/cm^2 on: a) roughened Au film on p-Si/SiO_2 wafers, b) normal Raman neat TNT crystals. Data normalized to laser power.

ν (cm^{-1})		
SERS	Raman neat	Assignment
723 w	720 vw	2,6-NO_2 scissoring
854 w	823 s	2,4,6-NO_2 scissoring
1080 s	1085 m	C-H bending (ring) in plane
1110 vw	1146 vw	C–C (ring) in plane bend + 2,4,6-C–N stretch + C–CH_3 stretch
1331 vs	1329 sh	4-NO_2 symmetric stretching
1570 s	1535 s	4-NO_2 asymmetric stretching

Table 12: Raman vibrational modes of TNT in the bulk and SERS of TNT with etched Au film on p-Si/SiO_2 wafers.

CHAPTER 7

7 SURFACE ENHANCEMENT FACTOR

The magnitude of the enhancement observed in SERS is estimated through the surface enhancement factor (SEF). The SEF is a key parameter for a better fundamental understanding of SERS and for its potential applications. This factor compares the increased intensity in Raman signal obtained under SERS conditions to that under normal Raman conditions. The SEF is normally expressed by,

$$\frac{I_{SERS}}{I_{bulk}} \times \frac{N_{bulk}}{N_{SERS}}$$

where I_{SERS} and I_{bulk} are the peak intensity of a vibrational mode of the molecule on the SERS spectrum and in the normal Raman spectrum (bulk), respectively, and N_{bulk} and N_{SERS} are the number of molecules sampled (illuminated by the laser) in the bulk and adsorbed on the SERS active substrate, respectively. This SEF definition is used to compare the average enhancement across different substrates and is called SERS substrate enhancement (SSEF).[112]

I_{SERS} and I_{bulk} were measured at a characteristic vibrational peak of the molecule using GRAMS/Al Spectroscopy Software by Thermo Scientific. N_{bulk} was calculated using the density of the solid and the interrogation volume,

$$N_{bulk} = \frac{d_{solid} \times V}{MW} \times N_A$$

were d_{solid} is the density of the solid, V is the observation volume, MW is the molecular weight of the molecule and N_A is Avogadro's number.

The observation volume is given by,

$$V = area\ laser\ spot \times depth\ confocal\ microscope$$

The area of the laser spot is determined by the microscope objective used in the measurements (Table 13). In our SERS experiments the 5x and 10x confocal microscope objectives were used.

Objective	*length (μm)*	*width (μm)*
5x	180	100
10x	90	50
20x	45	25
50x	18	10
100x	9	5
250x	3.6	2

Table 13: Dimensions of the laser focus by the confocal microscope objectives.

7.1 Confocal Raman Depth Profile

The observation volume of the Raman confocal microscope was characterized by performing a Raman depth profiling using silicon wafers of different thickness (210 and 310 μm). In a confocal system, the Raman signal decreases quickly as the microscope stage is raised or lowered, and the surface goes out of focus. We measured the system response to the intensity of the 520 – cm^{-1} peak of Si every 20 – μm as it was moved along the z-axis (2000 – μm) through the focal point (Figure 48). The full width at half maximum (FWHM) was taken and used as the depth of the confocal microscope. For silicon wafers, 210 and 310 – μm of thickness, we obtained for both a depth of 210 – μm. This indicates that our Raman confocal microscope has a limit of 210 – μm depth for silicon.

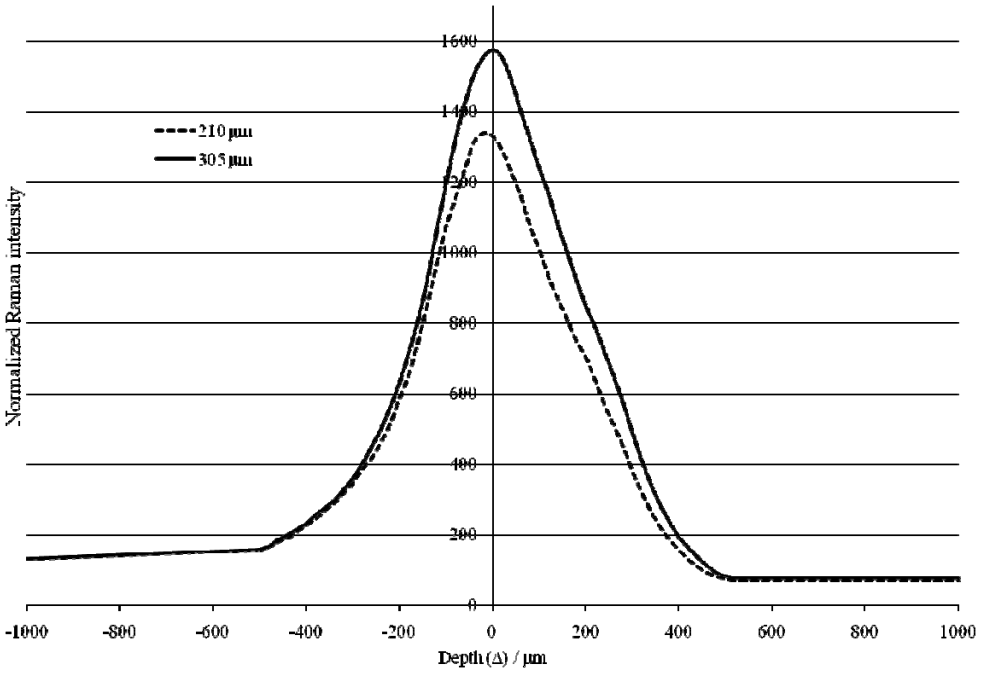

Figure 48: Intensity response of the 520 cm^{-1} band of silicon plotted against depth as it was moved through the focus point.

The number of molecules responsible for the normal Raman spectra (N_{bulk}) was estimated by measuring the depth of the bulk samples of 4-NBT, 4-ABT and TNT. We measured the system response to the intensity of a characteristic band of the molecule every 20 – μm as it was moved along 2000 – μm through the focal point. We used the 1333, 1082 and 1365 – cm^{-1} intense characteristic band of 4-NBT, 4-ABT and TNT, respectively (Figures 49, 50 and 51).

Initially we took the normal Raman spectrum of 4-NBT, 4-ABT and TNT as they were purchased. However, to be able to obtain a well defined depth profile a uniform surface is required. Bulk samples of 4-NBT were prepared by dropping 50 μL of a 10 mM ethanol solution over the smooth Au film the on p-Si/SiO_2 wafers with an area of 314 mm^2. The sample was left to evaporate at 40 °C for ~ 30 min. Bulk samples of 4-ABT were prepared in the same way as the 4-NBT bulk sample but evaporation was done at room temperature overnight. A slow evaporation was needed in order to obtain an evenly deposited film through the Au surface. TNT bulk samples were prepared by dropping 60 μL of 30 mM ethanol solution over the smooth Au film with an area of 17 mm^2. A smaller area of the gold surface and a higher concentration of TNT were used because we did not observe a normal Raman spectrum until small TNT crystals were formed.

Figures 49, 50, and 51 show the Raman depth profiles for the 4-NBT, 4-ABT and TNT bulk samples, respectively. The full width at half maximum (FWHM) of the Raman depth profiles was taken and used as the depth of the bulk samples. The 4-NBT, 4-ABT and TNT bulk samples showed a FWHM of 280 – μm, 240 – μm, and 310 – μm, respectively. Comparing the depths obtained from the silicon wafers (Figure 48) and the ones obtained from the bulk samples we can notice that our Raman confocal microscope seems to depend on the nature of the sample.

The observation volume for the normal Raman spectra is given by the area of the laser spot (i.e., 4.50×10^3 μm^2 for the10x confocal microscope objective) multiplied by the depth obtained from the Raman depth profiles. Density of 4-NBT, 4-ABT and TNT are 1.2, 1.362 and 1.608 g/cm^3, respectively. Multiplying the density with the observation volume and dividing by the molecular weight the moles responsible for the normal Raman spectra of 4-NBT, 4-ABT and TNT are 9.74×10^{15}, 1.17×10^{16}, and 9.88×10^{15}, respectively. Multiplying by the Avogadro's umber, N_{bulk} is 5.87×10^{39}, 7.08×10^{39}, and 5.95×10^{39} molecules of 4-NBT, 4-ABT and TNT, respectively.

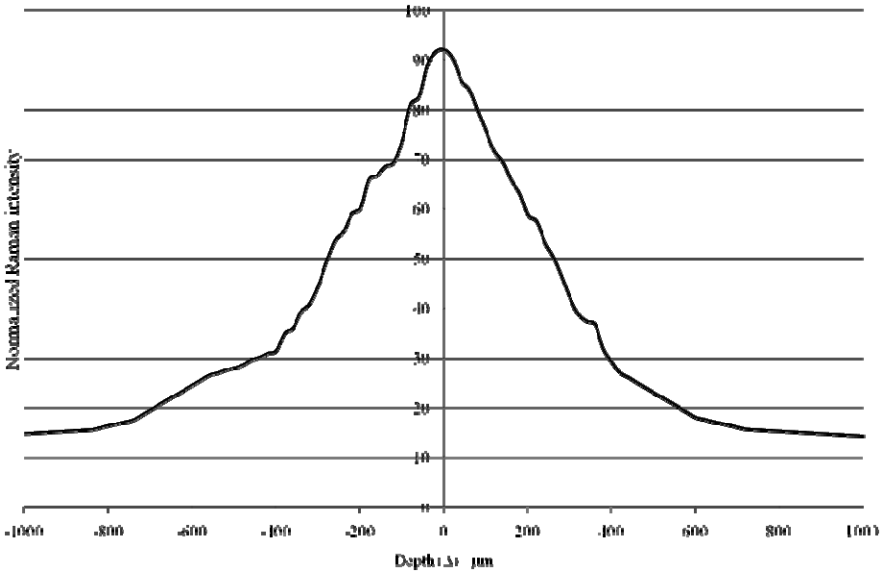

Figure 49: Intensity response of the 1082 cm^{-1} band of the 4-ABT plotted against depth as it was moved through the focal point.

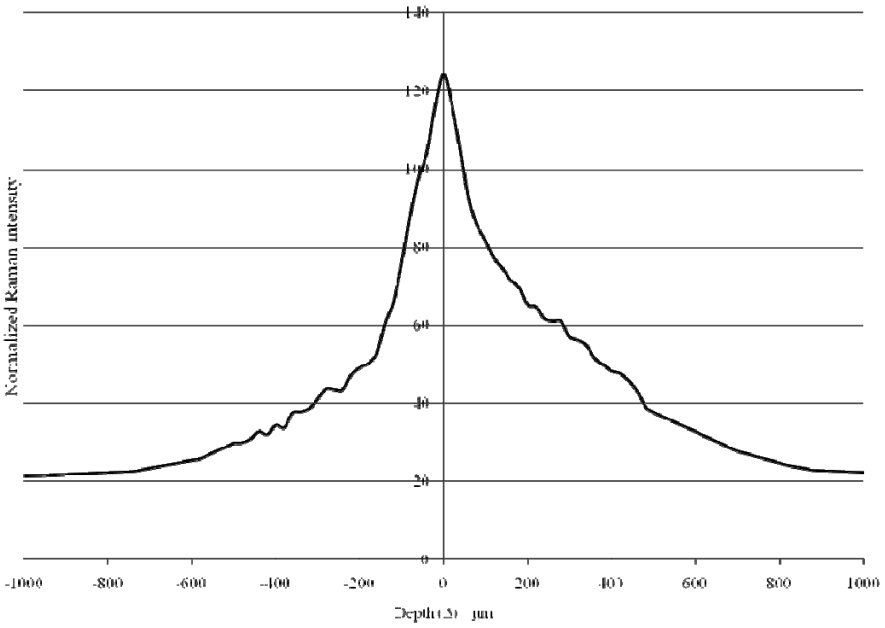

Figure 50: Intensity response of the 1336 cm^{-1} band of the 4-NBT plotted against depth as it was moved through the focal point.

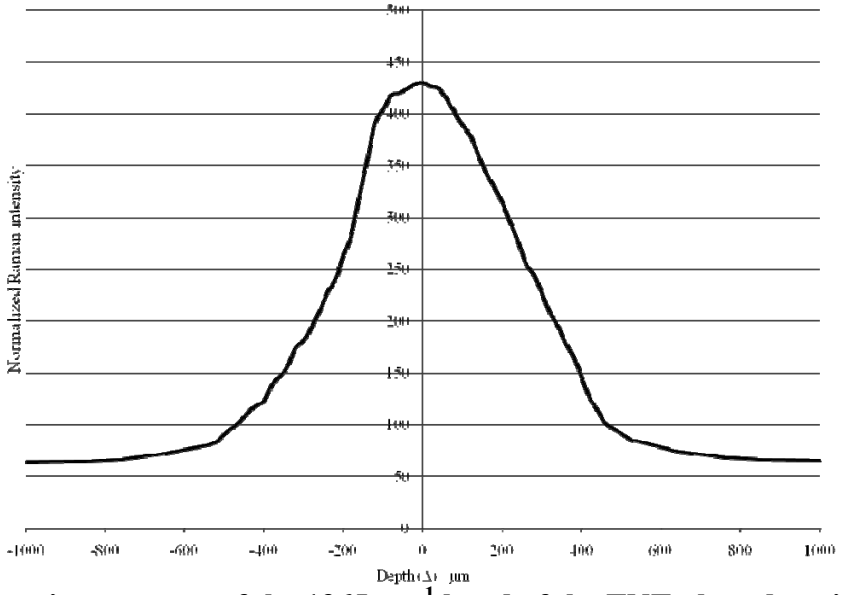

Figure 51: Intensity response of the 1365 cm^{-1} band of the TNT plotted against depth as it was moved through the focal point.

7.2 Theoretical Calculations: Area of a Molecule in a Monolayer

N_{SERS} was estimated calculating the area that the molecule occupies in a monolayer coverage and maximum packing density. The initial molecular geometries were constructed with Gaussview. Optimization of the molecular geometries was done with Gaussian GO3 software package using the B3LYP DFT method in conjunction with the split valence 6-311+G (d, p) basis set. The non-bonded distances of the optimized geometries were determined using Jmol. The distances to both ends of the molecules were estimated using the van der Waals radius. Using the non bonded distances and ACD/ChemSketch we estimated the area of closed packed molecules in a monolayer. This method was corroborated comparing the area of 4-ABT obtained with the one experimentally obtained by A. Gole et al.[104] for a maximum coverage over an Au surface.

Table 14 shows the values of non-bonded distances obtained by Jmol and the van der Waals radii at the molecular ends. The non-bonded distances of 4-ABT and 4-NBT were measured from the center of the N atom to the center of the S atom located at C4 and C1 of the benzene ring, respectively. In TNT the non-bonded distance was from the N located in C4 to the center of the C atom of the CH_3 group at C4 and C1 of the benzene ring, respectively. N and S van der Waals radii were used as the ends of the 4-ABT molecule. In 4-NBT, instead of using the N van der Waals radii as one end, the N to O atom projection was used since the optimized geometry of 4-NBT showed that this was so. The same was done for TNT using the van der Waals radii of the CH_3 group as the other end of the TNT molecule.

The area occupied by 4-ABT was estimated likewise as shown in Figure 52. A vertical orientation normal to the 4-ABT was assumed. The same was done for 4-NBT. The TNT area was estimated presuming a flat orientation as shown in Figure 53. It is appropriate to assume that

TNT was lying down on the substrate since our SERS spectra suggested it. The areas occupied in monolayer coverage and maximum packing density for 4-ABT, 4-NBT, and TNT were 23.8, 20.5 and 91.5 $Å^2$, respectively. N_{SERS} is given by dividing the area of the laser spot (i. e. 4.50×10^{11} $Å^2$ 10x confocal microscope objective) by the area of the molecule in a monolayer. Thus, N_{SERS} is 1.90×10^{10}, 2.20×10^{10}, and 4.92×10^{9} molecules for 4-ABT, 4-NBT and TNT, respectively.

4-ABT		*4-NBT*		*TNT*	
Distance (Å)	description	Distance (Å)	description	Distance (Å)	description
1.55	Nitrogen radii*	2.18	projection N–O	2.18	projection N–O
6.01	N–S**	6.05	N–S**	5.82	N–CH_3**
1.80	Sulfur radii*	1.80	Sulfur radii*	2.00	CH_3 radii*

Table 14: Non-bonded distance calculated by Jmol and van der Waals radii values* used to calculate the area of 4-ABT, 4-NBT and TNT.**

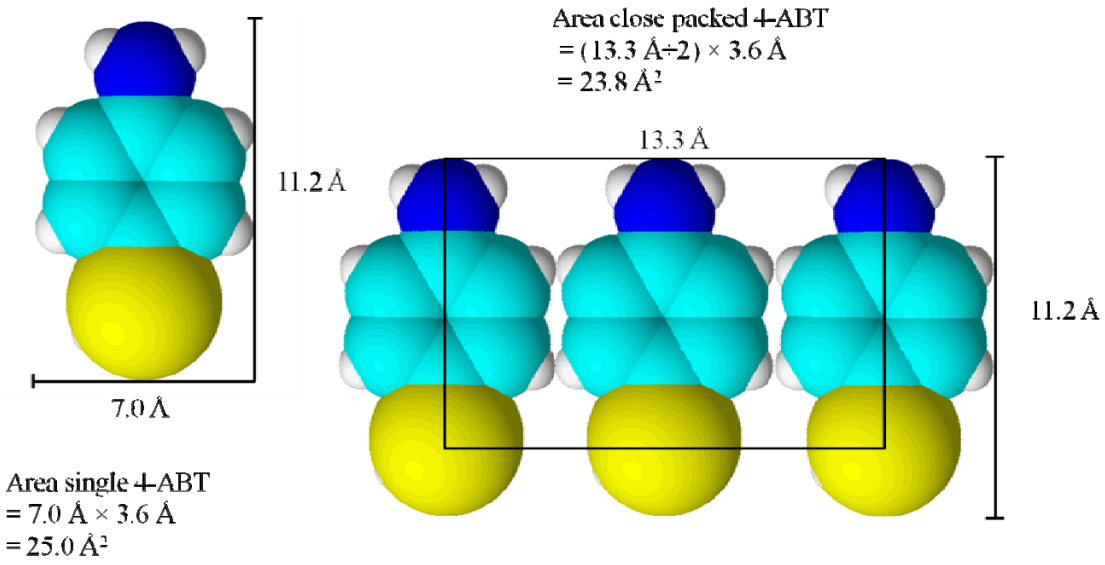

Figure 52: Sketch of estimated single and close packed area of 4-ABT using the non-bonded distances (Jmol), van der waals radius and ACD/ChemSketch.

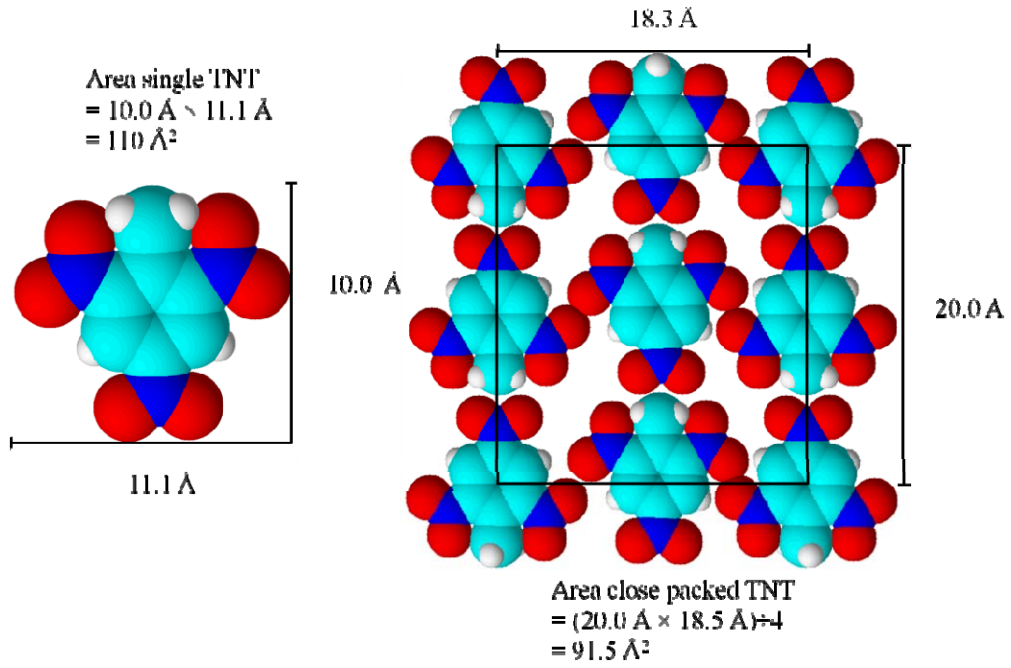

Figure 53: Sketch of estimated single and close packed area of TNT using the non-bonded distances (Jmol), van der waals radius and ACD/ChemSketch

Table 15 shows SEF values of 4-NBT with noble metal loaded n-TiO_2 nanoparticles, self assembled both onto microscopically smooth Au films on p-Si/SiO_2 wafers and onto stainless steel Type 316 (austenitic Cr-Ni-Mo). A matrix of Au/TiO_2 5% Au wt/wt nanoparticles laid over Au films gave us a Raman enhancement of 5 orders of magnitude, one order larger than the enhancement observed when laid over stainless steel. A Raman enhancement of 6 orders of magnitude was obtained for a matrix of Au/TiO_2 20% Au wt/wt nanoparticles laid over Au and stainless steel films. The difference in SEF values upon pH change was not appreciable when either underlying substrate was used.

On the other hand, significantly different SEF values were observed with Ag/TiO_2 showing changes both in pH and underlying substrate. A Raman enhancement of 6 orders of magnitude was observed when the particles were laid over the Au films as an underlying surface whereas with stainless steel an enhancement of only 5 orders of magnitude was observed. On both surfaces larger enhancements were observed at neutral pH. This difference was not observed when the matrix was prepared with Au/TiO_2 particles (see Table 15). The effect is due presumably to the poor homogeneity of Ag/TiO_2 particles. As stated earlier (Chapter 5) most Ag ions did not photo-reduce on the surface of the TiO_2 nanoparticles, owing to the fact that both Ag ions and TiO_2 have a positive charge, thus a mixture of colloidal Ag and TiO_2 particles was quite likely produced.

Colloid	*Substrate*	*pH*	*SEF*
5% wt Au/TiO_2	p-Si/SiO_2/Au	neutral	1.3×10^5
	Stainless steel	neutral	2.8×10^4
20% wt Au/TiO_2	p-Si/SiO_2/Au	acid	1.5×10^6
		neutral	1.4×10^6
	Stainless steel	acid	1.3×10^6
		neutral	1.0×10^6
54% wt Ag/TiO_2	p-Si/SiO_2/Au	acid	2.3×10^5
		neutral	1.1×10^6
	Stainless steel	acid	2.8×10^4
		neutral	3.1×10^5

Table 15: Surface enhancement factor (SEF) of 4-NBT with Au/TiO_2 5% Au wt/wt, Au/TiO_2 20% Au wt/wt and Ag/TiO_2 54% Ag wt/wt colloidal nanoparticles self assembled onto p-Si/SiO_2/Au and stainless steel substrate.

Raman enhancements of 4 orders of magnitude were observed for TNT when self assembled with Au/TiO_2 20% Au wt/wt colloidal particles over both smooth Au films and austenitic stainless steel. SEF values were of the same order when the pH was changed using either underlying substrate (see Table 16). The highest SEF obtained was at neutral pH with the smooth Au films on p-Si/SiO_2 wafers. Smaller Raman enhancements (about 100 times smaller) for TNT compared to 4-NBT were observed with Au/TiO_2 20% Au wt/wt nanoparticles laid over both smooth Au and austenitic stainless steel films. Since the TNT molecule does not possess groups with high affinity for Au like the 4-NBT molecule does, interaction of TNT with the Au/TiO_2 nanoparticles will be weak. Therefore, enhancement due to the chemical or charge transfer (CT) mechanism, which is usually in the order of 100 – 1000, is not going to arise. The CT mechanism, as stated earlier (Chapter 4), requires very specific molecular interactions with the metal surface. Consequently, the observed Raman enhancement of TNT was smaller due to the operation of only the SPR electromagnetic mechanism, the contribution of which is frequently of the 4 to 6 orders of magnitude.

Colloid	*Substrate*	*pH*	*SEF*
20% wt Au/TiO_2	p-Si/SiO_2/Au	acid	1.4×10^4
		neutral	2.9×10^4
	Stainless steel	acid	1.8×10^4
		neutral	1.2×10^4

Table 16: Surface enhancement factor (SEF) of TNT with Au/TiO_2 20% Au wt/wt colloidal nanoparticles self assembled onto p-Si/SiO_2/Au and stainless steel substrate.

Strong Raman enhancements, 7 orders of magnitude, for 4-ABT and 4-NBT were observed with etched Au films on p-Si/SiO_2 wafers. Enhancements of 4 orders of magnitude were observed for TNT, similar to those obtained with the self assembled Au/TiO_2 particles 20% Au wt/wt (Table 17). As mentioned above, the CT mechanism is not likely to operate with TNT. Thus, the only contribution to the observed Raman enhancement is the localized SPR mechanism due to the Au nanograins present in the galleries formed by chemical etching of the smooth Au films and the surface plasmon polariton associated with a thin metal surface.

Molecule	*SEF*
4-NBT	1.9×10^7
4-ABT	2.5×10^7
TNT	2.5×10^4

Table 17: Surface enhancement factor (SEF) of 4-NBT, 4-ABT with etched Au films on p-Si/SiO_2 wafers.

CHAPTER 8

8 CONCLUSIONS

The application of Au/TiO_2 composite NPs for the SERS detection of the trinitrotoluene (TNT) explosive, as well as other related nitroaromatic derivatives, has been described in the preceding pages. The main objectives of this research were 1) to achieve an efficient and stable SERS active substrate based on metal-semiconductor nanocomposites and 2) to define the mechanism that controls the enhancement of the Raman signals in these hybrid materials. To accomplish these objectives, the primary events in active particles that lead Raman enhancement have been taken into consideration. This is due to the fact that the formation of the excited state responsible for Raman scattering must compete with the other channels of non-radiative and radiative deactivation in the particle.

The base colloidal TiO_2 particles and the metal-TiO_2 composites have been fully characterized during the course of this research. Metal NPs were prepared by capping highly monodisperse colloidal n-TiO_2 particles with metal islands The introduction of noble metal (Au or Ag) has led to a considerable increase in enhanced Raman scattering as a result of the coupling between the localized surface plasmon (LSP) of metal nanoparticles (NP) and the surface plasmon polariton (SPP) associated with the thin metal surface of the underlying Raman substrate.

The preparation of a AuNPs – TiO_2 matrix over an Au coated p-Si/SiO_2 surface has been an essential step for the successful observation of enhanced Raman signals. One key aspect in the preparation of the Au/TiO_2 NPs active matrix has been the use of self-assembly sol-gel techniques. The microscopically smooth Au surface was an essential component to achieve coupling between the localized surface plasmon (LSP) induced by the laser on the active matrix

of metal nanoparticles (NP) and the surface plasmon polariton (SPP) induced in the continuous metal surface.

The promotion of electrons to the conduction band (charge transfer) using visible light (780 nm) is essential to generate the electron gas needed to induce LSP within hybrid metal-semiconductor NPs. This charge transfer process competes with other radiative and non-radiative processes of deactivation. Sorption of the analyte to the active surface is essential for successful surface Raman enhancement. Surface interaction can take place by a wide variety of sorption mechanisms ranging from simple physical absorption or strong adsorption to chemisorption by chemical bonding to the surface.

The consideration of the surface chemistry of the particles derivatized with noble metals has contributed to understand the operation of hybrid nanocomposite systems for surface Raman enhanced detection. The influences of some of the parameters that are important for the activity of enhanced Raman scattering were taken into account. Excellent results were obtained with semiconductor particles of colloidal dimensions prepared and maintained suspended in oxygen-free solutions at low pH values. The particles size has been identified to be critical for efficient induction of the electron plasma oscillations associated with LSPs. Increasing the rate of charge transfer to the conduction band while decreasing charge recombination is not an easy task. Electron mobility inside hybrid semiconductor particles following charge separation plays a crucial role. It can be calculated that the transit time is much faster than the recombination process (approximately 10,000 times) in 20 nm colloidal particles, while transit times are about equal for particles in powder form (1 – 2 μm). Particles of smaller size (60 nm or less) have many advantageous features that make it possible to utilize them for electromagnetic applications such as surface plasmon resonance (SPR) and surface enhanced Raman scattering (SERS).

Our studies are in good agreement with previous work by other research groups. The use of colloidal nanoparticles is advantageous over powders or even solid single crystals and polycrystalline materials, from the point of view of 1) high absorptivity for optical phenomena, 2) increased surface area, 3) very rapid charge carrier diffusion to the interface, 4) viability of spectroscopic techniques, and 5) possibility of surface modification by chemisorption, chemical derivatization or metal deposition.

The low Raman scattering efficiency observed for TNT can be explained in terms of the poor interaction between molecule and active surface. The TNT molecule does not possess groups with high affinity for either Au or TiO_2 particles like the 4-NBT molecule does; hence interaction of TNT with the Au/TiO_2 NPs was not strong enough and higher loadings were required to observe SERS. The fact that at higher Au NP loadings (20% wt Au or in the chemically etched Au galleries) enhancement of the Raman signals was observed is consistent with the operation of the SPR electromagnetic mechanism for TNT. Presumably, SPR is the more important or even dominant mechanism for SERS with TNT making our observations of particular value. On the one hand, considering the inherently lower Raman cross section for TNT, enhancement of the extremely weak Raman signals signifies that the SERS experimental system is working well. On the other hand, since the molecule-to-surface interaction is weak, TNT can be used as a probe to distinguish between the chemical or charge transfer SERS mechanism and the electromagnetic mechanism for a given experimental system.

In general terms, the results described in this document confirm that with ingenuity and molecular engineering skills it is possible to compete in good terms with scientists having at their disposal highly sophisticated techniques.

CHAPTER 9

9 EPILOGUE

The last few pages of this document are devoted to a summary discussion of the research work herein described in light of new developments in a retrospective view. During the course of this research considerable advances, both theoretical and experimental, have come to our attention. These advances are good reflections for the continuation of this line of work.

9.1 SERS with Bare Colloidal TiO_2 Nanoparticles

In spite of all our best efforts to observe enhancements of the Raman signals with bare colloidal TiO_2 particles, all attempts failed in our hands. Recently, well after this work was completed, reports by Tijana Rajh et al. (2011)[106] have appeared detailing the observation of SERS on hybrid TiO_2-molecular composites in liquid suspension, but with very modest enhancement factors (less than about 10^3). The success with bare colloidal TiO_2 particles in suspension, together with the theoretical single unified treatment of the SERS effect published earlier by Lombardi and Birk (2009),[113] explain why our initial experiments with 4-NBT and TNT were so unsuccessful. One reason is the absence in the bare semiconductor particle of surface-plasmon resonances in the visible. The second is the inability of our analytes to bind and form charge-transfer states on the semiconductor surface.

Lombardi and Birk, as well as most investigators in the field, now agree that there are three possible sources for the Raman enhancement. The one, most often cited, is the existence of surface plasmon resonances (SPR) due to the collective excitation of the electrons in the conduction band of the particle. This would require band-gap excitation of the semiconductor for positive SERS under our conditions. The second most important contribution is the chemical or

charge transfer (CT) mechanism between the molecule and the conduction band of the particle. When orbital mixing occurs between the molecular orbitals of the analyte and the orbitals which constitute the conduction band of the nanoparticles, the result is a charge transfer complex that leads to a shift in the effective band gap of the material to a lower energy. This charge transfer can occur in either direction depending on the relative energies of the semiconductor Fermi level and the HOMO and LUMO levels of the adsorbed molecule. The third possible contribution is due to resonances within the adsorbed molecule itself. We conclude that none of these mechanisms are likely to work with metal oxide semiconductors and the analytes of interest in liquid suspension.[16, 64, 105, 114]

It is clear that the positive SERS results reported by Tijana Rajh et al. with bare colloidal TiO_2 in liquid suspension are due to the specificity of the dopamine type analytes they used. The surface plasmon resonance of most semiconductors is located in the infrared region, which is far from the 514 or 785 nm excitation lines used in most experiments. Therefore, the semiconductor SPR cannot be a contribution for SERS with the bare semiconductor particles. This leaves the chemical mechanism (CT) and molecular resonances on the particle surface as the only two other possibilities to contribute to SERS under these conditions, but this requires, as stated earlier, very specific molecular interactions with the semiconductor surface as is in the reported case between TiO_2 and dopamine. Enhancement of the Raman signals was observed when dopamine was sorbed on the surface of the bare TiO_2 nanoparticles,[75, 106] and at the same time a red shift in the TiO_2 band gap occurred, the source of the reported Raman enhancement was clearly demonstrated since it can be attributed to charge transfer from dopamine to TiO_2. Moreover, when the excitation energy was below the energy of the charge transfer complex, Raman enhancement was not observed.

The theoretical explanation proposed by this group for the TiO_2 – dopamine system is summarized in Figure 9. It basically involves charge transfer from the molecule to the TiO_2 particle. Dopamine binding onto the TiO_2 surface results in charge transfer and the appearance of surface states within the TiO_2 band gap which reduces the TiO_2 excitation energy to 1.6 eV (776 nm). This allows excitation from the midgap state to the conduction band with radiation of a frequency lower than the band gap of bare TiO_2 (3.2 eV at 388 nm). Therefore, to be able to observe SERS with bare semiconductors, a charge transfer complex has to be formed between the molecule and the semiconductor surface. Formation of a CT complex under these conditions depends on the surface properties of the semiconductor, the frequency of the excitation, and the specific nature of both the molecule and the semiconductor. We, therefore, conclude that SERS studies based on the molecule-to-semiconductor charge transfer model is very limited and difficult to extend to the type of analyte of interest for further applications at this time. Nevertheless, it is intriguing to investigate the effect in the dopamine Raman spectrum when Au capped TiO_2 particles in colloidal suspension are exposed to dopamine.

9.2 The Unified View of Surface-Enhanced Raman Scattering

In very simple terms, enhancements in Raman intensity come about when a molecule is in the vicinity of a metal. Special sites referred as “hot spots” are responsible of the observed enhancement. The underlying source of the Raman signal enhancement is still a subject of considerable controversy and as such it is not yet completely understood. Lombardi and Birke[113] have provided a unified theory for the three possible resonances contributing to the enhancement factor in surface-enhanced Raman scattering: surface plasmon resonances (SPR) in the metal, charge transfer resonance (CT) between the HOMO of the molecule and the conduction band of the metal, and resonances within the adsorbed molecule itself.

The greatest triumph of this unified view of the SERS phenomenon is a single analytical expression for the Raman intensity in the proximity of one or more metal nanoparticles. To obtain this unified expression Lombardi and Birke followed the procedure of Albrecht, introducing Herzberg–Teller vibronic coupling into the expression for the polarizability. This is carried out to second order perturbation theory by allowing for the breakdown of the Born – Oppenheimer approximation.* They extended the calculation of Albrecht by considering the molecule – metal system to be coupled and including the filled and unfilled levels of the conduction band of the metal in the Herzberg-Teller expansion. The resulting expression for the polarizability (α) contains the sum of three terms:

$$\alpha = A + B + C$$

where A is a sum of terms considered to be responsible for resonance Raman spectra, while B and C are sums of Herzberg – Teller contributions which stem from molecule – to – metal or metal – to – molecule CT transitions, respectively. The sum A has terms with only Franck-Condon† integrals in the numerator. Far from resonance, A vanishes while near a resonance, one of the terms can make it very large and become dominant. This term allows only totally symmetric Raman lines and it is usually considered to be responsible for resonance Raman spectra. The sums B and C represent Herzberg – Teller contributions to transitions that are said to 'borrow" intensity from nearby allowed molecular transitions via the Herzberg – Teller coupling constant. These terms allow transitions both to totally symmetric and to non-totally symmetric vibrational modes and the resulting intensity can be enhanced by SPR or CT

* The Born-Oppenheimer Approximation (BOA) allows for the wavefunction of a molecule to be broken into its electronic and nuclear (vibrational, rotational) components.

† The Franck-Condon Approximation (FCA) allows calculating transition probabilities using fixed nuclear positions since electronic transitions occur on a time scale short compared to nuclear motion. Note that this is a more restrictive approximation than the BOA which states that nuclear and electronic motions can be separated, but does not demand that the nuclear coordinates be at a fixed value.

processes. If SERS spectra show intensity in non-totally symmetric normal modes, the *B* or *C* sums or both must be involved. They may also contribute to the totally symmetric bands, as do the *A* expressions. In a region of the SERS excitation spectrum far from either a CT or molecule resonance (blue shifted to the plasmon oscillations band), where only SPR resonances are important, the *A* term does not contribute. In this region the *B* and *C* sums are entirely responsible for the SERS intensity.

The unified view of the surface enhanced Raman phenomenon does a marvelous job to explain the underlying source of the huge increases in signal observed in SERS, but it does not help as much in sorting out the various contributions to SERS. A general discussion of these contributions is a nearly impossible task and thus requires the consideration of particular cases to define the boundaries of the problem. For instance, the analytical expressions for *B* and *C* involve infinite sums over all the states of the molecule – metal system, and as such are rather unmanageable. However, when the excitation wavelength is in the region of CT or MR (in addition to the SPR), only one or a few of these terms will dominate the sum, and things do get simplified [113] considerably. If we consider a single dominant term for either the *B* or *C*, the SERS intensity will be proportional to the square of the polarizability associated to this dominant term, i.e., to $|R_{IFK}(\omega)|^2$. Here, I, F, and K refer to the ground state, a CT state, and an excited molecular state of the molecule – metal system, respectively. As Lombardi and Birke detail in their seminal paper, the denominator in the expression for $R_{IFK}(\omega)$ involves the product of three terms, each of which represents a different resonance contribution to SERS. The first term is due to plasmon resonance of a single metal particle.[‡] The second term may be potential (Fermi energy) – dependent and represents a charge – transfer resonance, and the third term represents a molecular

[‡] Lombardi and Birke chose the expression for a single particle recognizing that non-spherical particles or particle aggregates with "hot spots" a more complex expression will be required.

resonance. In the third case, if the resonance condition is fulfilled, we have SERRS (surface enhanced resonance Raman scattering). This is the case for most of the single – molecule experiments for which the molecular transition is also in resonance with the laser.

It is possible to predict whether a CT resonance will occur if good estimates of the Fermi level of the solid substrate and of the energy levels of the molecule at the surface are available. Bonding of the molecule to the metal surface may result in charge transfer (CT) and the appearance of CT – surface states, which effectively reduce the excitation energy away from the metal plasmon band. This allows laser induced excitation from the surface states to the plasma or conduction band states with radiation of a frequency lower than the bare molecule HOMO-LUMO gap which usually resides in the UV or towards the blue VIS region. The charge transfer can occur in either direction depending on (horizontal Frank-Condon) the relative energies of the metal Fermi level and the HOMO and LUMO levels of the adsorbed molecule. Molecule–to–metal CT occurs for molecules with low-lying unfilled π orbitals whereas metal–to–molecule CT occurs for molecules without low-lying unfilled π orbitals. This can be illustrated for crystal violet cation, CV^+, where the electrochemical HOMO – LUMO gap of 1.9 eV is almost identical to the lowest electronic singlet $\pi - \pi^*$ transition. Thus, if the Fermi level of the metal (Ag) is around – 4.1 eV, light of 2 eV (633 nm) will excite besides the $\pi - \pi^*$ molecular resonance, a molecule – to – metal CT transition. Pyridine is also an excellent example to illustrate when a CT resonance will occur in a SERS study. The resonances in the pyridine – Ag nanoparticle system show three distinct regions. The pyridine absorption spectrum involves three transitions in the UV (two $\pi - \pi^*$ transitions and one $n - \pi^*$ transition) below 350 nm. In the near UV – VIS region there are a surface plasmon resonance and a molecule – to – metal charge transfer resonance, which overlap between 480 and 520 nm. It can be clearly seen that by

restricting the laser to wavelengths lower than around 480 nm, *only* the surface plasmon resonance will be excited, whereas as the wavelength is increased, a mixture of CT and SPR will contribute to the overall enhancement. It is now very interesting to realize that although there are no molecular resonances excited in this region, the approximate expression for $R_{IFK}(\omega)$ deduced by Lombardi and Birke [113] shows that intensity can be borrowed, if not stolen, from them via Herzberg – Teller coupling and the amount of borrowing is proportional to the square of the transition moments (i.e., the oscillator strengths) of the molecular transitions. Now, if we go back to the crystal violet cation – Ag system, the absorption spectrum clearly shows that in this case all three resonances are in the VIS region and overlap with the highest intensity around 575 nm, which is foretelling of single molecule SERS and makes CV^+ so popular. Here, the LUMO of the molecule is too low for metal – to – molecule CT if the Fermi level of Ag is close to – 4.1 eV but molecule – to – metal transitions can be in resonance when the exciting laser is around 600 nm.

To summarize the analysis of the denominator part of the single polarizability term $R_{IFK}(\omega)$ we conclude that it predicts the possibility of one, two, or three resonances simultaneously, depending on the metal and molecular parameters. The exact magnitude of the enhancement, the relative contribution of each of the three possible types of resonances involved, and the appearance of the Raman spectra (i.e., the relative intensities of the various bands) depend crucially on the particular choice of excitation wavelength, location of the nanoparticle Fermi energy, nanoparticle size and shape with respect to the wavelength, oscillator strength, and bandwidth of the resonance. We know turn to examine the numerator part in the single polarizability term $R_{IFK}(\omega)$, which provides the selection rules for SERS. The numerator consists of the product of four terms, i.e., all four terms must simultaneously be nonzero in order for a particular normal mode to be observed. It is important to realize, as Lombardi and Birke have

stressed, "*that all four terms in the numerator are linked to each other*." This fact is not always appreciated in discussions of SERS enhancements. First, we note that the Herzberg-Teller effect contributes a product of the coupling parameter $h_{IF} = \langle I|\partial V_{eN}/\partial Q_k|F\rangle$ with the vibrational integral $\langle i|Q_k|f\rangle$. The normal mode Q_k is the same in both expressions. The latter $\langle i|Q_k|f\rangle$ displays the normal harmonic oscillator selection rules (i.e., $f = i \pm 1$), and only those normal modes for which this term is nonzero will be observed. We also note that this term implies that overtones will not normally be observed and that non-totally symmetric vibrations may be allowed in SERS. However, an additional restriction for a normal mode to be observed is imposed by the Herzberg-Teller coupling term, h_{IF}, which must simultaneously be nonzero for the normal mode Q_k to be observed. This additional selection rule is crucial for understanding the details of SERS spectra. The other two terms in the numerator of $R_{IFK}(\omega)$ involve a product of the dipole transition moments μ_{KI}^{σ} and μ_{FK}^{ρ}, which are the allowed molecular transition I – K and the (metal – to – molecule) charge-transfer transition F – K. The charge-transfer or molecular transition moment will depend on the molecular orientation with respect to the metal and therefore depends on the geometry of the molecule – metal complex. Since the maximum electric field due to the plasmon resonance is normal to the metal surface, and the electric field interacts with the dipole moments through the inner product $\boldsymbol{\mu}\mathbf{E}$, it is expected that the components of μ_{FK}^{ρ} and μ_{KI}^{σ} normal to the surface (i.e., $\rho, \sigma = Z$) to provide the major contribution to SERS. We also note that the combination of molecular transition moments, Herzberg-Teller coupling, and direction of the plasmon-induced electric field places restrictions on the nature of the spectrum and the symmetry of the normal modes to be expected.

It is important now to understand how the product of terms in the numerator of the polarizability $R_{IFK}(\omega)$ links the three resonances in the denominator. The charge-transfer

transition moment (μ_{FK}^{ρ}) is coupled with the component of the electric field due to the surface plasmon resonance perpendicular to the surface ($\rho = Z$). This requires knowledge of the orientation of the molecule with respect to the surface. But most importantly, it also shows that the *surface plasmon and the charge transfer are intimately coupled to each other and are not separable*. Furthermore, the charge-transfer resonance is linked to the molecular resonance by the molecular transition moment (μ_{KI}^{σ}) since they both refer to the same excited-state K. Consequently, these two resonances cannot be considered to be separate. The Herzberg-Teller coupling constant ($h_{IF} = \langle I|\partial V_{eN}/\partial Q_k|F\rangle$) provides the link between the charge-transfer process (F) and the observed Raman spectral lines governed by $\langle i|Q_k|f\rangle$. Thus Lombardi and Birke arrived at the most fundamentally important conclusion that the three resonances which contribute to SERS intensities *cannot be considered separately*, and any description of SERS must include this linkage in order to provide a complete and accurate depiction of the effect.

9.2.1 The Difference between SERS and Normal Raman Spectroscopy

To conclude this section of the Prologue concerning the unified view of surface enhanced Raman scattering we consider what the difference between SERS and normal Raman spectroscopy is. If one examines the general expressions for SERS and the corresponding expression for normal Raman spectroscopy, they at first appear to be quite similar. They both involve large sums of terms similar to the expression for the simplified polarizability $R_{IFK}(\omega)$. However, more careful examination reveals that one important difference is the inclusion of charge-transfer (F) states between the molecule and metal. This comes about because we consider the molecule-metal system together. Lombardi and Birke note here that for metals, the Fermi level lies above the highest occupied molecular orbital (HOMO) of most molecules (for silver $E_F = -4.3$ eV and for pyridine the IP is – 9.26 eV), and often lower than many, if not all,

of the unoccupied orbitals (UMO). Thus for every molecular transition (HOMO → UMO), there is a corresponding charge-transfer transition between the molecule and the metal (E_F → UMO or HOMO → EF), which lies lower in energy than the purely molecular transition. One immediate consequence is that the charge-transfer terms in the SERS polarizability expansion lie lowest and, therefore (if the oscillator strengths are at all comparable), due to the smallness of the energy denominator, tend to contribute more to the SERS intensity than the corresponding molecular transition. These may provide the dominant contributions under some circumstances, even to the totally symmetric normal modes. In the region of the spectrum where only the surface plasmon resonance is active (i.e., at an excitation wavelength far from the charge – transfer or molecular resonances), the charge-transfer states cannot be ignored because they appear in the sum over states expression and usually represent the leading terms in that sum.

A second important difference between SERS and normal Raman spectroscopy lies in the molecular orientation with respect to the surface. Lombardi and Birke note that normally, except for Raman spectra in crystals, the orientation of the molecule with respect to the polarization of the electric vector of exciting light is random, and in order to account for this, the expression for normal Raman spectroscopy is averaged over all orientations. For SERS, the molecule is usually considered to be adsorbed to the surface in a definite orientation. The surface plasmon resonance results in a very strong component of the electric field normal to the metal surface, with a somewhat smaller tangential component, at least for most molecule-metal configurations. In either case, the result is that the SERS spectrum of the molecule often looks quite different than that of the molecule alone. We cannot average over all molecular orientations with respect to the polarization of the exciting light. Although the molecular frequencies are usually not changed very much, the relative intensities are drastically altered in comparison to the normal Raman

spectrum. Totally symmetric normal modes tend to dominate the spectrum far from charge-transfer or molecular transitions, while non-totally symmetric modes become considerably more prominent in the region of charge-transfer or molecular resonances. In this case the Herzberg-Teller-surface selection rules discussed in become important in interpreting the spectrum.

9.2.2 Sorting Out the Various Contributions to SERS

Lombardi and Birke have shown brilliantly that indeed there are three linked resonant contributions to the total SERS signal. At any chosen excitation wavelength, there might be quite different contributions from each resonance, but as the excitation wavelength is scanned, the relative degree of contribution from each resonance may vary considerably. This results in considerable variation in the appearance of the spectrum as a function of excitation wavelength. In order to state with confidence the amount of contribution from each source, it is necessary to have a complete description of the location (in wavelength), the width, and the oscillator strength of each transition involved. Thus there is the need for good optical spectra of the individual nanoparticles, the molecule, and if possible the molecule-metal system. This latter is often difficult to obtain, and an excitation profile of the SERS spectrum might suffice. In any case, as Lombardi and Birke clearly state, *it is impossible to determine the degree of contribution of each resonance by obtaining SERS spectra at only a single wavelength,* unless there are other measures, such as an electrochemical voltage profile or a nanoparticle size-dependent profile. Unfortunately, for the research herein described the limited availability of laser lines and the lack of any prior expertise in both photochemistry and electrochemistry by most team members and colleagues, has been an extremely impairing limitation to complete this dissertation in a proper and timely manner. This part of the Epilogue has been written in an attempt to alert future participating colleagues and students.

9.3 Metal – Molecule Schottky Junctions in SERS

In this section we address the nature of the metal – molecule interface and whether it can be theoretically treated as Schottky barrier in a metal – semiconductor junction.[§] Recently, Gang Logan Liu and co-workers[115] have proposed a complementary interpretation of the mechanism responsible for the strong enhancement of Raman signals observed at the metal – molecule interface. They have systematically investigated the effect of a strong static local electric field treating as a Schottky barrier the metal – molecule junction in SERS substrates. The study provides a viable explanation to the low repeatability of SERS experiments as well as the Raman peak shifts as observed in SERS and raw Raman spectra. It has been found that a strong electrostatic built-in field at the metal-molecule junction along specific orientations can result in 2 -- 4 more orders of enhancement in SERS. We include the highlights of this paper as part of the Epilogue for its theoretical and experimental relevance to the future of this field.

Of the three possible mechanisms for surface enhanced Raman scattering, the SPR mechanism in the metal particle, the CT mechanism), and the SERRS mechanism, these authors address many of the inconsistencies found in the literature when sorting out their relative contribution to the Raman spectrum with metal nanoparticles. For instance, the well-known electromagnetic (EM) mechanism (SPR) is usually described as a resonance between the incident laser radiation and the plasmon mode of the metal nanoparticle, conducing to a large amount of energy being "concentrated" on the nanoparticle. Subsequently, the nanoparticle re-emits a portion of the EM energy by Mie scattering,[**] thereby creating an intense surface field with very high energy density at or near the particle surface. In general, this EM enhancement by SPR

[§] A Schottky barrier, named after Walter H. Schottky, is a potential barrier formed at a metal–semiconductor junction which has rectifying characteristics, suitable for use as a diode.

[**] Mie theory is an analytical solution of Maxwell's equations for the scattering of electromagnetic radiation by spherical particles whose size is similar to the wavelength of the radiation.

should amplify the Raman scattering with no selectivity, irrespective of the type of molecules adsorbed on a particular surface. However, the CO and N_2 molecules differ by a factor of 200 in their Raman enhancement factors under the same experimental conditions. Another interesting example is that of water. While many SERS studies are conducted in aqueous systems, there is rarely an enhancement in the Raman spectrum of water. These results cannot be explained by invoking only a simple electromagnetic enhancement. Further, when the coupling of chemical enhancement and the electromagnetic enhancement is considered, the SERS enhancement factor can be up to the order of 10^{10}. This huge enhancement is difficult to explain when sorting out the relative contributions of each effect.

It is quite clear by now that the contributions from electromagnetic coupling and chemical binding are inseparable. Thus the kind of charge transfer (CT) contribution in those high enhancement experiments, including our own experiments, is still unknown. In the charge transfer model, an incident photon excites an electron from the metal surface into an adsorbed molecule, creating a negatively charged excited molecule. The molecular geometry of this excited molecule differs from that of the neutral species. This charge transfer induces a nuclear relaxation within the excited molecule, which results in the return of the electron to the metal surface, the creation of an excited neutral molecule, and the emission of a wavelength shifted (Raman) photon. In principle, in the CT model an adsorbed molecule can, under specific conditions, interact with a metal surface in such a way that there is a large increase in molecular polarizability, α.

It is also quite important to realize that even though the three SERS mechanisms are not independent of each other and may not be separable experimentally or theoretically, certain limits can be established where one mechanism is dominant over the others. In fact, to isolate the

chemical enhancement, SERS has been studied for adsorbates on smooth surfaces, which are known to be incapable of supporting large localized surface plasmons. These studies showed only small enhancements. However, recent theoretical as well as experimental studies have shown that under certain conditions the chemical enhancement can be much larger than predicted earlier. In addition, SERS enhancements have also been observed for molecules interacting with small nanoclusters or nanocrystalline semiconductor surfaces, both of which are not expected to support plasmon resonances at the laser excitation and thus should show only small EM enhancement. However, the CT mechanism as it has been studied to explain the Raman enhancement in molecular adsorbates, it fairly gives at most an intuitive picture of the chemical enhancement and mostly relies on phenomenological parameters. In this context, it is increasingly important to understand the microscopic nature of SERS using first principle modeling, and this is precisely what Gang Logan Liu and co-workers have done in this magnificent paper.

It is now widely believed that the chemical bonding effects in SERS can be simulated just considering the local environment of a molecule, which is also consistent with the adatom model, a model which assumes that the roughness features at the atomic scale determine the “hot spots” on a metal surface. The adatom model thus discounts the operation of electromagnetic enhancement due to the excitation of surface plasmons in the metal. In addition, it discounts the effect of interference between the chemical and the electromagnetic mechanism if any. Obviously, this is easier said theoretically than it can be done experimentally.

Many issues have been considered so far by the scientific community in the context of the SERS chemical enhancement. These include the binding geometry of the adsorbate, the effects of adsorption on various noble and transition metal surfaces, the influence of positively

charged atoms at the metal surface, the effect of adsorbed chloride anions, the effect of nonzero static electric fields, and the solvent effects. However, even though there is clear evidence of the existence of a solid-liquid electrochemical interface (electric double layer discovered recently by many) in all SERS experiments, *there are no systematic studies so far, with the exception of* Gang Logan Liu and co-workers *to elucidate the double layer effect in SERS.* The lack of systematic studies in this area is perplexing considering that it is well known that the strong electric field present at the electric double layer perturbs the vibrational frequencies of the adsorbed species (the vibrational Stark effect, VSE) and that the electric field changes the adsorbate vibrational line strength (the vibrational intensity effect (VIE). To fill in the vacuum, this study was done and that is why it is included here.

The Liu study takes into account the effects of a solid-liquid electrochemical interface on a model SERS molecule, benzenethiol, by assuming an interfacial static electric field at the interface between a metal surface and an adsorbed molecule. An additional external static electric field applied can be seen as a perturbation to the system Hamiltonian. Actually, this Liu work was motivated also by the need to interpret recently published potential-dependent SERS studies, where an enhancement of the order of $10^5 - 10^9$ were observed upon application of an external electric field to glutamic acid adsorbed on a Ag substrate. Their present study aimed to provide a microscopic insight to any such future studies that may lead to achieve controllable SERS intensities by an applied electric field module. To present a simplified picture of the metal-molecule interface, in the Liu study the molecule has been considered as a semiconductor and the magnitude of the static electric field so developed has been calculated on the basis of a metal – molecule Schottky barrier mechanism

9.3.1 A Molecular Monolayers as a Semiconductor

Most organic materials are electrical insulators with values of electrical conductivity at room temperature in the range 10^{-9} – 10^{-14} S cm^{-1} (10^{9} – 10^{14} Ω cm resistivity). To obtain a larger conductivity and hence semiconducting behavior, the HOMO-LUMO gap needs to be reduced and this can be achieved by extensive π-bonding. A reduced band gap allows electrons to jump more easily between the conduction and valence bands and gives rise to semiconductor properties. Aromatic rings for instance, contain alternating single and double bonds which lead to overlapping p-orbitals that form π-bonds. In conjugated π-bonds electrons are delocalized and shared between the atoms on the σ-framework. Similar to conduction due to the delocalized "sea of electrons" in metals, free movement of delocalized π-electrons in organic compounds allows organic molecules to conduct electricity and behave as semiconductors.

9.3.2 The Metal – Molecule Interface as a Schottky Barrier

It is well-known that a potential barrier known as a Schottky barrier forms at a metal-semiconductor junction and that the built-in electrostatic field strength can be as high as volts per angstrom. The formation of a Schottky barrier between a metal electrode and organic electronics materials has been extensively studied both theoretically and experimentally in recent years. In this discussion, it is assumed that the benzenethiol (BZT) molecule is equivalent to a highly doped p-type semiconductor and the Au – BZT junction is equivalent to a metal-semiconductor Schottky barrier junction. The relevant parameters used to define the Au – BZT Schottky barrier junction are: 1) the work function of Au, 5.3 eV, the ionization potential (IP) of benzenethiol, 8.32 eV, the band gap of benzenethiol, 4.1 eV, the difference between the Fermi energy of the metal and the HOMO (HIB, hole injection barrier), ~2.06 eV and the difference in the Fermi level and that of the LUMO (EIB, electron injection barrier), ~2.04 eV. The interface between a

metal and a organic semiconducting layer can be described as a Schottky barrier when molecules have large energy gaps between the HOMO and the LUMO, as in the study under discussion, since the Schottky limit holds well.

9.3.3 Calculations Show the Schottky Barrier Augments the Raman Cross Section

The effect of built-in electric field direction on the Raman scattering process has been theoretically explored applying a static electric field the benzenethiol molecule along various directions to simulate the built-in field of the Schottky barrier developed at the metal – molecule junction. The molecular conformation under different conditions was found through the energy minimization process n each case. The computational results have shown that the bond lengths of the benzenethiol molecule deform upon application of an electric fields. In general, it was found that the extent of the bond length change is proportional to the built-in electric field. The molecular conformation change will inherently induce dipole moment and polarizability changes since the inter-atomic distance and angle are altered. In addition to polarization effects, there is an intermediate state created by the adsorption of benzenethiol to Au atoms changing the excitation incident wave (532 nm or 2.33 eV) far below the purely intra-molecular electronic transitions level (4.1 eV).

The observed increase in polarizability derivative (and subsequent enhanced Raman intensity) has been explained by a large change in the dipole moment due to a change in molecular conformation (and an increase in the bond length). Since the polarizability of the molecule is related to the vibrational coordinates and the dipole moment, an increased in polarizability is expected. Also observed is an increase in the absolute polarizability derivative (modulus of the polarizability derivative) along with increase in dipole moment. Since the Raman scattering cross section is proportional to the square of polarizability derivative, an

increase in Raman scattering cross-section is found even in the absence of an electronic transition.

The metal-molecule Schottky barrier also induces the change of energy band gap of a benzenethiol molecule. The band gap of an isolated benzenethiol molecule is in the ultraviolet region, which makes the electronic level transition forbidden for visible excitations. The Fermi (HOMO) level of gold is somewhere in the middle of the molecule energy band gap. The energy difference between gold Fermi level and HOMO of an isolated molecule shows now the viability of a charge transfer scheme where charges can transfer from a metal atom cluster to the molecule or from the molecule to the metal cluster. Upon attaching Au atoms, the density and number of accessible states in the hybrid system increase. In addition, the band gap shrinks and this can make it possible to induce resonance Raman with visible excitation light. This last statement is not unreasonable since the calculated band gap of benzenethiol alone is 4.092 eV while the band gap calculated for benzenethiol with three Au atoms is 0.75 eV. The built-in electric field further shrinks the band gap, increasing the probability of transition to higher excited states and further enlarging the Raman scattering cross section.

The decrease in the band gap of the molecule upon to adsorption to metal atoms can be explained by the neutralization of the dipole layer on the metal when the molecules come in close contact with the metal surface. This is due to a mismatch between the benzenethiol ionization potential (IP ~ 8.32 eV) and the work function of the metal (~5.3 eV). Actually, this is what leads to the formation of the Schottky barrier in the first place which will give rise to a built-in electric field directed from metal surface to the organic molecule. The developed electric field will oppose further leakage of electrons from the metal. So even for a weakly interacting (physisorbed or van der Waal interacting) species or for a strongly interacting (covalent bonded)

species, the electron cloud leaking out of the metal surface is pushed back into the metal. This pushback (or pillow) effect always contributes to reduce the surface dipole and lower U_{vac} relative to E_F and, consequently, leads to a reduced work function of the sample. The interface dipole is expected to lower the LUMO level of the organic molecule. In the study being discussed a reduction of ~2.54 eV has been observed for the benzenethiol LUMO level. In addition, the metal work function is increased (i.e., decreases the Fermi energy) and the HOMO energy of the organic layer is increased. As a result, the hole injection barrier (HIB) is reduced. In fact, an increase of 1.37 eV for the HOMO level of benzenethiol has been observed upon conjugation to gold, which reduces the HIB from 2.06 eV before conjugation to 0.69 eV after conjugation.

Finally, to elucidate the effect of the magnitude of the built-in electric field on Raman intensity, the Raman scattering spectra were simulated calculating the Raman intensity as a function of applied electric field. These authors have shown that with application of a local built-in electric field of 1.028 V/Å, one extra order of Raman enhancement was achieved in addition to the enhancement from the gold atom attachment. This shows that a built-in electric field can actually bridge the gap between high enhancement experimental observations and previous theoretical simulations. In fact, with an application of a high built-in field of 2.570 V/Å we achieved a 2-4 more orders of enhancement which points to the importance of a metal-molecular junction for the potential 10^{14} Raman enhancement.

10 REFERENCES

1. *Nanoparticles and nanotechnology research.* **Rocco, A.** 1999, Journal of Nanoparticle Research, pp. 1-6.

2. http://nanotech.mediadir.in. [Online]

3. **Feldheim, D. L. and Foss, C. A. Jr.** *Metal Nanoparticles Synthesis, Characterization and Applications.* New York : Marcel Dekker, 2002.

4. **Kik, P. G. and** Brongersma **M. L.** *Surface Plasmon Nanophotonics.* New York : Springer, 2007.

5. **Grey, S. K.** *Surface Plasmon Enhanced Spectroscopy, Plasmonics.* 2007.

6. **Smith E., and Dent, G.** *Modern Raman Spectroscopy: A Practical Approach.* England : John Wiley & Sons, 2005, 1.

7. *Observation of* **molecules** *adsorbed on III-V semiconductor quantum dots by Surface-enhanced Raman scattering.* **Quagliano, L.G.** 2004, J. Am. Chem. Soc., Vol. 126, pp. 7393-7398.

8. *Enhanced Raman scattering as a probe for 4-Mercaptopyridine surface-modified copper oxide nanocrystals.* **Wang, Y. F., Hu, H. L., Jing, S. Y., Wang, Y. X., Sun, Z. H., Zhao, B., Zhao, C. and Lombardi, J. R.** 2007, Anal. Sci., Vol. 23, pp. 787-791.

9. *Surface-enhanced Raman scattering on mercaptopyridine-capped CdS microclusters.* **Wang, Y., Sun, Z., Wang, Y., Hu, H., Zhao, B., Xu, W. and Lombardi, J. R.** 2007, Spectrochimica Acta Part A, Vol. 66, pp. 1199–1203.

10. *Ag Nanocrystal Junctions as the Site for Surface-Enhanced Raman Scattering of Single Rhodamine 6G Molecules.* **Michaels, A. M. and Jiang, J. and Brus, L.** 2000, J. Phys. Chem. B, Vol. 104, p. 11965.

11. *Chemically Patterned Microspheres for Controlled Nanoparticle Assembly in the Construction of SERS Hot Spots.* **Braun, G., et al.** 2007, J. Am. Chem. Soc., Vol. 129, p. 7760.

12. *Surface-Enhanced Raman Spectroscopy and Nanogeometry: The Plasmonic Origin of SERS.* **Lee S. J., Guan Z., Xu H., and Moskovits M.** 2008, J. Phys. Chem. C, Vol. 111, pp. 17985-*17988*.

13. *Creating Well-Defined Hot Spots for Surface-Enhanced Raman Scattering by Single-Crystalline Noble Metal Nanowi.* **Taejoon K., Ilsun Y., Ki-Seok J., Wonjun C., Yonghoon L., Kwanyong S., Youngdong Y., Q-Han P., Hyotcherl I., Yung D. S., and Bongsoo K.** 2009, J. Phys. Chem. C, Vol. 113, pp. 7492-7496.

14. *Sub-wavelength localization of hot-spots in SERS.* **Le Ru, E.C. and Etchegoin, P.G.** 2004, Chem. Phys. Lett, Vol. 396, pp. 393–397.

15. *Surface-enhanced Raman scattering and biophysics.* **Kneipp, K., Kneipp, H., Itzkan, I., Dasari, R.R., and Feld, M.S.** 2002, J. Phys. Condens. Matter., Vol. 14, pp. R597-R624.

16. *Surface-enhanced spectroscopy.* **Moskovits, M.** 1985, Rev. Mod. Phys., Vol. 57, pp. 783-826.

17. *Surface-Enhanced Raman Scattering from 4-Ethylpyridine and Poly(4 vinylpyridine) on Gold and Silver Electrodes.* **Garrell, R. L. and Beer, K. D.** 1989 : s.n., Langmuir, Vol. 5, pp. 452-458.

18. *Surface-Enhanced Raman Spectroscopy at a Silver Electrode as a Detection System in Flowing Streams.* **Pothier, N. J. and Forcé, R. K.** 1990, Anal. Chem., Vol. 62, pp. 678-680.

19. *Surface-Enhanced Raman Scattering of p -Aminobenzoic Acid at Ag Electrode.* **Park, H., Lee,S. B., Kim, K., and Kim, M. S.** 1990, J. Phys. Chem. , Vol. 94, pp. 7516-1580.

20. *Effect of preparation conditions for roughening gold substrate by oxidation–reduction cycle on the surface-enhanced Raman spectroscopy of polypyrrole. Materials Chemistry and Physics.* **Yu-Chuan, L., Bing-Joe, H. and Wen-Jie J.** 2002, Vol. 73, pp. 129-134.

21. *Strategy and Characteristics of Polypyrrole Deposited on Silver Substrates with Silver-Containing Nanocomplexes.* **Yu-Chuan, L., Yen-Chun, L. and Ya-Ting, L.** 2003, J. Phys. Chem. B. , Vol. 107, pp. 11370-11375.

22. *Charge Transfer from Tetrathiafulvalene to Silver and Gold Surfaces Studied by Surface-Enhanced Raman Scattering.* **Sandroff, C. J., Weltz, D. A., Chung, J. C., and Herschbach, D. R.** 1983, J. Phys. Chem., Vol. 87, pp. 2127-2133.

23. *Surface-Enhanced Raman Scattering from Copper and Zinc Phthalocyanine Complexes by Silver and Indium Island Films.* **Jennings, C. and Aroca, R.** 1984, Anal. Chem., Vol. 56, pp. 2033-2035.

24. *Surface resonance Raman spectra of dyes absorbed on metals.* **Yamada, H., Nagata, H., and Kishibe, K.** 1986, J. Phys. Chem., Vol. 90, pp. 818–823.

25. *Silver-island films as substrates for enhanced Raman scattering: Effect of deposition rate on intensity.* **Vicki, L., and Cotton, T. M.** 1991, Anal. Chem, Vol. 63, pp. 241-247.

26. *Near-infrared surfaced enhanced Raman scattering from metal island films.* **Jeannings, C. A. and Kovacs, G. J.** 1992, J. Phys. Chem., Vol. 96, pp. 1340-1343.

27. *Reversible Temperature Dependence in Surface-enhanced Raman Scattering of 1-Propanethiol Adsorbed on a Silver Island Film.* **Pang, Y. S., Hwang, H. J., and Kim, M. S.** 1998, J. Phys. Chem. B., Vol. 102, pp. 7203–7209.

28. *Temperature Dependence and Annealing Effects in Surface-Enhanced Raman Scattering on Chemically Prepared Silver Island Films.* **Kwon, C. H., Boo, D. W., Hwang, H. J., and Kim, M. S.** 1999, J. Phys. Chem. B., Vol. 103, pp. 9610-9615.

29. *Ultrahigh-Vacuum Studies of Enhanced Raman Scattering from Pyridine on Ag Surfaces.* **Rowe, J. E. , Shank, C. V. , Zwemer, D. A. , and Murray, C. A.** 1980, Phys. Rev. Lett., Vol. 44, pp. 1770–1773.

30. *Surface-Enhanced Raman Scattering from Sputter-Deposited Silver Surfaces.* **Davies, J. P., Pachuta, J., Cooks, R. G., and Weaver, M. J.** 1986, Anal. Chem, Vol. 58, pp. 1290-1294.

31. *Sputtered silver oxide layers for surface-enhanced Raman spectroscopy.* **Büchel, D., Mihalcea, Fukaya, C., Atoda, T., N., and Tominaga, J.** 2001, App. Phys. Lett., Vol. 79, pp. 620-623.

32. *Adsoption and surface enhanced Raman of dyes on silver and gold colloids.* **Lee, P. C. and Meisel, D.** 1982, J. Phys. Chem., Vol. 86, pp. 3391-3395.

33. *Surface-Enhanced Raman Spectroscopy of Colloidal Metal Systems: A Two-Dimensional Phase Equllibrlum in p -Aminobenzoic Acid Adsorbed on Silver.* **Suh, J. S., DILella, D. P., and Moskovits, M.** 1983., J. Phys. Chem. , Vol. 87, pp. 1540-1544.

34. *Surface-Enhanced Raman Scattering by Molecules Adsorbed on Aqueous Copper Colloids.* **Creighton, J. A., Alvarez, M. S., Weltz, D. A., Garoff, S., and Kim, M. W.** 1983, J. Phys. Chem., Vol. 87, pp. 4793-4799.

35. *Surface enhanced Raman spectroscopy of amino acids and nucleotide bases adsorbed on silver.* **Suh, J. S. and Moscovits, M.** 1986, J. Am. Chem. Soc., Vol. 108, pp. 4711-4718.

36. *In Situ Photoreduced Silver Nitrate as a Substrate for Surface-Enhanced Raman Spectroscopy.* **Ahern, M. and Garrell, R. L.** 1987, Anal. Chem., Vol. 59, pp. 2813-2816.

37. *Enzyme immunoassay utilizing surface enhanced Raman scattering of the enzyme reaction product.* **Dou, X., Takama, T., Yamaguchi, Y. and Yamamoto, H.** 1997, Anal. Chem., Vol. 69, pp. 1492-1495.

38. *Surfaced enhanced Raman scattering of biological molecules on metal colloids II: Effects on aggregation of gold colloid and comparison of effects of pH of glycine solutions between gold.* **Xiaoming, D., Young, M. J., Zhuang-Qi, C, and Yukihiro, O.** 1999, Appl. Spectrosc., Vol. 53, pp. 1440-1447.

39. *A Silver Colloid Produced by Reduction with Hydrazine as Support for Highly Sensitive Surface-Enhanced Raman Spectroscopy.* **Nickel, U., Castell, A., Pöppl, K., and Schneider, S.** 2000, Langmuir, Vol. 16, pp. 9087-9091.

40. *A New Method for Fast Preparation of Highly Surface-Enhanced Raman Scattering (SERS) Active Silver Colloids at Room Temperature by Reduction of Silver Nitrate with*

Hydroxylamine Hydrochloride. **Leopold, N. and Lendl, B.** 2003, J. Phys. Chem. B., Vol. 107, p. 572.

41. *Periodically structured metallic substrates for SERS.* **Kahl, M., Voges, E., Kostrewa, S., Viets, C., and Hill, W.** 1998, Sensors and Actuators B, Vol. 51, pp. 285–291.

42. *Interparticle coupling effects in nanofabricated substrates for surface-enhanced Raman scattering.* **Gunnarsson, L., Bjerneld, E. J., Xu, H, Petronis, S., Kasemo, B., and Källa, M.** 2001, App. Phys. Lett., Vol. 78, pp. 802-804.

43. *Controlling the optical response of regular arrays of gold particles for surface-enhanced Raman scattering.* **Félidj, N., Aubard, J., and Lévi, G.** 2002, Phys. Rev. B. , Vol. 65, pp. 075419-1-8.

44. *Optimized surface-enhanced Raman scattering on gold nanoparticle arrays.* **Félidj, N., Aubard, J., Lévia, G., Krenn, J. R., Hohenau, A., Schider, Leitner A., and Aussenegg, F. R.** 2003, App. Phys. Lett., Vol. 82, pp. 3095-3097.

45. *Optimization of SERS-active substrates for near-field Raman spectroscopy.* **Grand, J., Kostcheev, S., Bijeon, J. L., Lamy de la Chapelle, M., Adam, P.M., Rumyantseva, A., Lérondel, G., Royer P.** 2003, Synth. Met., Vol. 139, pp. 621–624.

46. **Geddes, C. D. and Lakowicz, J. R.** *Radiative Decay Engineering.* New York : Springer, 2005.

47. *On a remarkable case of uneven distribution of light in a diffraction grating spectrum.* **Wood, R.W.** 1902, Philos. Mag. , Vol. 4, pp. 396-402.

48. *Diffraction gratings with controlled groove form and abnormal distribution of intensity.* **Wood, R.W.** 1912, Philos. Mag., Vol. 23, pp. 310–317.

49. *On the dynamical theory of gratings.* **Rayleigh, L.** 1907, Proc. R. Soc. London. Ser, Vol. A79, p. 399.

50. *The theory of anomalous diffraction gratings and of quasi-stationary waves on metallic surfaces (Sommerfeld's waves).* **Fano, U.** 1941, J. Opt. Soc. Am., Vol. 31, pp. 213–222.

51. *Excitation of nonradiative surface plasma waves in silver by the method of frustrated total reflection.* **Otto, A.** 1968, Z. Phys., Vol. 216, pp. 398–410.

52. *Radiative decay of non radiative surface plasmons excited by light.* **Kretschmann, E. and Reather, H., and Naturforsch, Z.** 1968, Teil A, Vol. 23, pp. 2135–2136.

53. *Surface plasmon resonance for gas detection and biosensing, Sens. Actuators.* **Liedberg, B., Nylander, C., and Lundstrom, I.** 1983, Vol. 4, pp. 299–304.

54. **Tudos, A. J. and Schasfoort, R. B.M.** Introduction to Surface Plasmon Resonance. London : Royal Society of Chemistry, 2008, pp. 1-2.

55. *Raman Spectra of Pyridine Adsorbed at a Silver Electrode.* **Fleishmann, M., Hendra, P. J. and McQuiuan, A.** 1974, J. Chem. Phys. Lett. , Vol. 26, pp. 163-166.

56. *Surface Raman spectroelectrochemistry—part I: heterocyclic, aromatic, and aliphatic amines adsorbed on the anodized silver electrode.* **Jeanmaire, D. L. and Van Duyne, R. P.** 1977, J. Electroanal. Chem., Vol. 84, pp. 1-20.

57. *Anomalously intense Raman spectra of pyridine at a silver electrode.* **Albrecht, M. G. and Creighton, J. A.** 1977, J. Am. Chem. Soc., Vol. 99, pp. 5215-5217.

58. *Surface Enhanced Raman Scattering.* **Campion, A. and Kambhampati, P.** 1998, Chem. Soc. Rev., Vol. 27, pp. 241-250.

59. *Surface enhanced Raman scattering (SERS) of citrate ion adsorbed on colloidal silver.* **Kerker, M., Siiman, O., Bumm, L. A., and Wang, D. S.** 1980, Appl. Opt., Vol. 19, pp. 3253-3255.

60. *Enhanced Raman scattering by molecules adsorbed at the surface of colloidal spheroids.* **Wang, D. S. and Kerker, M.** 1981, Phys. Rev. B., Vol. 24, pp. 1777-1790.

61. *Theory of Raman scattering by molecules adsorbed at electrode surfaces.* **King, F. W., Van Duyne, R.P., and Schatz, G. C.** 1978, J. Chem. Phys., Vol. 69, pp. 4472-4481.

62. *The role of charge-transfer states of the metal-adsorbate complex in surface-enhanced raman scattering.* **Arenas, J. F., Soto, J., Lopez, I., Fernandez, D. J., Otero, J. C., Marcos, J. I.** 2002, J. Chem. Phys., Vol. 116, pp. 7202-7216.

63. *Theory of Enhance Light Scattering from Molecules Adsorbed at the Metal-Solution Interface.* **Gersten, J. I., Birke, R. L., and Lombardi, J. R.** 1979, Phys. Rev. Lett., Vol. 43, pp. 147–150.

64. *Surface-enhanced Raman scattering.* **Otto, A., Mrozek, I., Grabhom, H., and Akemann, W.** 1992, J. Phys. Condens. Matter., Vol. 4, pp. 1143–1212.

65. *Role of Nanoparticle Surface Charge in Surface-Enhanced Raman Scattering.* **Alvarez-Puebla, R. A., Arceo, E., Goulet, P. J. G., Garrido, J. J. and Aroca, R. F.** 2005, J. Phys. Chem. B., Vol. 109, pp. 3787-3792.

66. *Surface-enhanced Raman scattering on colloidal nanostructures.* **Aroca, R.F. Alvarez-Puebla, R.A., Pieczonka, N., Sanchez-Cortez S., Garcia-Ramos, J.V.** 2005, Adv. Colloid Interfac., Vol. 116, pp. 45-61.

67. *Self-Assembled Metal Colloid Films: Two Approaches for Preparing New SERS Active Substrates.* **Li, X., Xu, W., Zhang, J., Jia, H., Yang, B., Zhao, Bofu Li, B., and Ozaki, Y.** 2004, Langmuir, Vol. 20, pp. 1298-1304.

68. *The structural basis for giant enhancement enabling single-molecule Raman scattering.* **Wang, Z., Pan, S., Krauss, T. D., Du, H. and Rothberg, L.** 2003, J. Proc. Natl. Acad. Sci. USA, Vol. 100, pp. 8638-8643.

69. *Self-Assembled Metal Colloid Monolayers: An Approach to SERS Substrates.* **Freeman, R. G., Grabar, K. C., Allison, K. J., Bright, R. M., Davis, J. A., Guthrie, A. P., Hommer, M. B., Jackson, M. A., Smith, P. C., Walter, D. G. and Natan, M. J.** An Approach to SERS Substrates. Science. : . : s.n., 1995, Science, Vol. 267, pp. 1629-1632.

70. *Surface micropatterning technique for surface-enhanced Raman scattering analysis.* **Ruan, W., Lu Z., Zhou, T., Zhao, B. and Niu, L.** 2010, Anal. Methods, Vol. 2, pp. 684–687.

71. *Synthesis and Characterization of Monodisperse Nanocrystals and Close-packed Nanocrystal Assemblies.* **Murray, C. B. and Kagan, C. R.** 2000, Ann. Rev. Mat., Vol. 30, pp. 545-610.

72. **Balandin, A. A. and Wang, K. L.** Handbook of semiconductor nanostructures and nanodevices. California : American Scientific Publishers, 2006, Vol. 5, 6.

73. *ZnO nanoparticle size-dependent excitation of surface Raman signal from adsorbed molecules: Observation of a charge-transfer resonance.* **Sun, Z. H., Zhao, B. and Lombardi, J. R.** 2007, Appl. Phys. Lett., Vol. 91, pp. 221106–1-3.

74. *Nanoparticle metal-semiconductor charge transfer in ZnO/PATP/Ag assemblies by surface-enhanced Raman spectroscopy.* **Yang, L., Jiang, Ruan, X., W., Zhao, B., Xu, W., and Lombardi, J. R.** 2008, J. Phys. Chem. C, Vol. 112, pp. 20095–20098.

75. *SERS of Semiconducting Nanoparticles (TiO2 Hybrid Composites).* **Musumeci, A., Gosztola, D., Schiller, T., Dimitrijevic, N. M., Mujica, V., Martin, D., and Rajh, T.** 2009, J. Am. Chem. Soc. , Vol. 131, pp. 6040–6041.

76. *Adsorption study of 4-MBA on TiO2 nanoparticles by surface-enhanced Raman spectroscopy.* **Yang, L., Jiang, X., Ruan, W., Zhao, B., Xua, W. and Lombardi, J. R.** 2009, J. Raman Spectrosc., Vol. 40, pp. 2004–2008.

77. *Raman spectroscopy of adsorbates on semiconductors by means of SERS effect.* **Quagliano, L. G., Jusserand, B., and Ladan, F. R.** 1995, Phys. Stat. Sol. (a)., Vol. 152, pp. 219-225.

78. *Surface-enhanced raman scattering from molecules adsorbed on GaAs surfaces.* **Quagliano, L. G. and Orani, D.** 1996, Surf. Sci., Vol. 368, pp. 108-112.

79. *SERS spectroscopy to study adsorbates on semiconductor surfaces.* **Quagliano, L. G., Jusserand, B. and Orani, D.** 1998, J. Raman Spectrosc., Vol. 29, pp. 721-724.

80. *Surface enhanced Raman scattering from molecules adsorbed on semiconductor surfaces.* **Quagliano, L. G., Jusserand, B., Ladan, E R. and Izrael, A.** 1993, J. Electron Spectrosc., Vol. 64, pp. 177-182.

81. *Preparation and studies of Ag–TiO2 hybrid nanoparticles of core-shell structure.* **Zhou, Y., Wang, C.Y., Liu, H.J., Zhu, Y.R. and Chen, Z.Y.** 1999, Materials Science and Engineering B, Vol. 67, pp. 95-98.

82. *The surface enhanced Raman scattering effects of composite nanocrystals of Ag–TiO2.* **Liu, Y., Liu, C., Zhang, Z., and Wang, C.** 2001, Spectrochimica Acta Part A, Vol. 57, pp. 35-39.

83. *Characterization of Novel Ag on TiO2 Films for Surface-Enhanced Raman Scattering.* **Mills, A., Hill, G., Steward, M., Graham, D., Smith, W. E., Hodgen, S., Halfpenny, P. J., Faulds, K., and Roberson, P.** 2004, Appl. Spectrosc., Vol. 58, pp. 922-928.

84. *Simple synthesis and size dependent surface-enhanced Raman scattering of Ag nanostructures on TiO2 by thermal decomposition of silver nitrate at low temperature.* **Wang, R. C., Gao, Y.S., and Chen, S. J.** 2009, Nanotechnology, Vol. 20, pp. 375605-375611.

85. *New application of photocatalytic TiO2 nanoparticles on the improved surface-enhanced Raman scattering.* **Liu, Y., Yu, C., Wang, C. and Juang, L.** 2006, Chem. Phys. Lett., Vol. 420, pp. 245-249.

86. *Surface enhanced Raman spectroscopy for adsorption studies on semiconductor nanostructured films.* **Lana-Villarreal, T., Perez, J. M., and Gomez, R.** 2004, Surf. Sci., Vol. 572, pp. 329-336.

87. *Surface-enhanced Raman spectrometry for trace organic analysis.* **Vo-Dinh, T., Hiromoto, M. Y. K., Begun, G. M. and Moody, R. L.** 1984, Anal. Chem., Vol. 56, pp. 1667-1670.

88. *Chemical procedure for preparing surface-enhanced Raman scattering active silver films.* **Ni, F. and Cotton, T. M.** 1986, Anal. Chem., Vol. 58, pp. 3159-3163.

89. *Direct analysis of high-performance thin-layer chromatography spots of nucleic purine derivatives by surface-enhanced Raman scattering spectrometry.* **Sequaris, J. M. and Koglin, E.** 1987, Anal. Chem., Vol. 59, pp. 525-527.

90. *Feasibility studies for the detection of organic surface and subsurface water contaminants by surface-enhanced Raman spectroscopy on silver electrodes.* **Carrabba, M. M., Edmonds, R. B. and Rauh, R. D.** 1987, Anal. Chem., Vol. 59, pp. 2559-2563.

91. *Surface-enhanced resonance Raman spectroscopy as an ancillary high-performance liquid chromatography dectector for nitrophenol compounds.* **Ni, F., Thomas, L., and Cotton, T. M.** 1989, Anal. Chem., Vol. 61, pp. 888-894.

92. *Determination of purine bases by reversed-phase high-performance liquid chromatography using real-time surface-enhanced Raman spectroscopy.* **Sheng, R., Ni, F., and Cotton, T. M.** 1991, Anal. Chem., Vol. 63, pp. 437-442.

93. *In situ surface enhanced resonance Raman scattering analysis of a reactive dye covalently bound to cotton.* **White, P. C., Munro, C. H., and Smith, W. E.** 1996, Analyst., Vol. 121, pp. 835-838.

94. *Surface-Enhanced Raman Spectroscopy as anin SituReal-Time Probe of Catalytic Mechanisms at High Gas Pressures: The CO–NO Reaction on Platinum and Palladium.* **Williams, C. T., Tolia, A. A., Chan, H. Y. H., Takoudis, C. G., and Weaver, M. J.** 1996, J. Catal., Vol. 163, pp. 63-76.

95. *Near-infrared surface-enhanced Raman scattering of trinitrotoluene on colloidal gold and silver.* **Kneipp, K., Wang, Y., Dasari, R. R., Feld, M. S., Gilbert, B. D., Janni, J., and Steinfield, J. I.** 1995, Spectrochim. Acta A, Vol. 51A, pp. 2171-2175.

96. *Simultaneous multianalyte identification of molecular species involved in terrorism using Raman spectroscopy.* **Docherty, F. T., Monaghan, P. B., McHugh, Graham, C. J., D., Smith, W. E., and Cooper, J. M.** IEEE Sensors Journal, Vol. 5, pp. 632-640.

97. **Urbanski, T.** *Chemistry and Technology of Explosives (I).* New York : Pergamon, 1964.

98. *Analysis of high-explosive samples by Fourier transform Raman spectroscopy.* **Akhavan, J.** 1991, Spectrochim. Acta A, Vol. 47A, pp. 1247-1250.

99. *In-situ detection and identification of trace explosives by Raman microscopy.* **Cheng, C., Kirkbridge, T. E., Batchelder, D. N., Lacey, R. J., and Sheldon, T. G.** 1995, J. Forensic Sci., Vol. 40, pp. 31-37.

100. *Use of a fiber optic probe for the detection and identification of explosive materials by Raman-spectroscopy.* **Hayward, I. P., Kirkbride, T. E., Batchelder, D. N., and Lacey, R. J.** 1995, J. Forensic Sci., Vol. 40, pp. 883-884.

101. *Surface-Enhanced Raman Detection of 2,4-Dinitrotoluene Impurity Vapor as a Marker To Locate Landmines.* **Sylvia, J. M., Janni, J. A., Klein, J. D., and Spencer, K. M.** 2000, Anal. Chem., Vol. 72, pp. 5834-5840.

102. *Detection and analysis of cyclotrimethylenetrinitramine (RDX) in environmental samples by surface-enhanced Raman spectroscopy.* **Hatab, N. A., Eres, G., Hatzingerc, P. B., and Gua, B.** 2009, J. Raman Spectrosc., Vol. 41, pp. 1131-1136.

103. *Semiconductor-Metal Nanocomposites. Photoinduced Fusion and Photocatalysis of Gold-Capped TiO2 (TiO2/Gold) Nanoparticles.* **Dawson, A. and Kamat, P. V.** 2001, J. Phys. Chem. B., Vol. 105, pp. 960-966.

104. *Electrostatically Controlled Organization of Carboxylic Acid Derivatized Colloidal Silver Particles on Amine-Terminated Self Assembled Monolayers.* **Gole, A., Sainkar, S. R., and Sastry, M.** 2000, Chem. Mater., Vol. 12, pp. 1234-1239.

105. *Charge Transfer Resonance Raman Process in Surface-Enhanced Raman Scattering from p-Aminothiophenol Adsorbed on Silver: Herzberg-Teller Contribution.* **Masatoshi, O., Matsuda, N., Yoshii, K., and Uchida, I.** 1994, J. Phys. Chem., Vol. 98, pp. 12702-12707.

106. *Utilizing Chemical Raman Enhancement: A Route for Metal Oxide Support-Based Biodetection.* **Hurst, S. J., Fry, H. C., Gosztola, D. J., and Rajh, T.** 2011, J. Phys. Chem. C., Vol. 115, pp. 620–630.

107. *Observation of Enhanced Raman Scattering for Molecules Adsorbed on TiO2 Nanoparticles: Charge-Transfer Contribution.* **Yang, L., Jiang, X., Ruan, W., Zhao, B., Xu, W., and Lombardi, J. R.** 2008, J. Phys. Chem., Vol. 112, pp. 20095–20098.

108. *A study of the nucleation and growth processes in the synthesis of colloidal gold.* **Turkevich, J., Stevenson, P.C. and Hillier, J.** 1951, Discuss. Faraday Soc., Vol. 11, pp. 55-75.

109. **Pleskov, Y. V. and Gurevich, Y. Y.** Semiconductor Photoelectrochemistry. New York : Consultants Bureau, 1986, pp. 63-75.

110. *A colorimetric method for determining low concentrations of mercaptans.* **Ellman, G.L.** 1958, Arch. Biochem. Biophys., Vol. 74, pp. 443-450.

111. *The relative acidities of 4-nitro-, 2,4-dinitro-, and 2,4,6-trinitro-toluene.* **Lelievre, J., Farrell, P. G., and Terrier, F.** 2, 1986, J. Chem. Soc., Perkin Trans. 2, pp. 333-336.

112. *Surface Enhanced Raman Scattering Enhancement Factors: A Comprehensive Study.* **Le Ru, E. C., Blackie E., Meyer, M., and Etchegoin, P. G.** 2007, J. Phys. Chem. C., Vol. 111, pp. 13794-13803.

113. *A Unified View of Surface-Enhanced Raman Scattering.* **Lombardi, J. R., and Brike, R. L.** 2009, Acc. Chem. Res., Vol. 42, pp. 734-742.

114. *Theory of Enhanced Light Scattering from Molecules Adsorbed at the Metal-Solution Interface.* **Gersten, J. I., Birke, R. L., and Lombardi, J. R.** 1979, Phys. Rev. Lett., Vol. 43, pp. 147–150.

115. *Metal-Molecule Schottky Junction Effects in Surface Enhanced Raman Scattering.* **Gartia, M. R., Bond, T. C., and Liu, G. L.** 2011, J. Phys. Chem. A, Vol. 115, pp. 318-328.